JOINT SCALE-LAG DIVERSITY IN MOBILE WIDEBAND COMMUNICATIONS

DISSERTATION

Presented in Partial Fulfillment of the Requirements for

the Degree Doctor of Philosophy in the

Graduate School of The Ohio State University

By

Adam R. Margetts, B.S., M.S.

* * * * *

The Ohio State University

2005

Dissertation Committee:

Philip Schniter, Adviser

Hesham El Gamal

Andrea Serrani

Ananthram Swami

Approved by

Adviser

Graduate Program in
Electrical and Computer
Engineering

ABSTRACT

We consider the effect of mobility on a wideband direct sequence spread spectrum (DSSS) communication system, and study a *scale-lag* Rake receiver capable of leveraging the diversity that results from mobility. A wideband signal has a large bandwidth-to-center frequency ratio, such that the typical narrowband Doppler spread assumptions do not apply to mobile channels. Instead, we assume a more general *temporal scaling* phenomenon, i.e., a dilation of the transmitted signal's time support. Based on a uniform ring of scatterers model, we determine that the wideband scattering function, which quantifies the average scale spreading, has a "bathtub-shaped" *scale profile*. We investigate, through frame-theoretic tools, the translation- and dilation-spacing parameters of a scale-lag Rake basis, and compare the performances of a *scale-lag* Rake and a *Doppler-lag* Rake, each capable of leveraging the diversity that results from mobility. When the translation spacing of the Rake functions is equal to the minimum resolvable lag, there is no significant performance difference between the receivers. For wider spacings, the receiver is more reliant on dilation diversity; hence, the scale-lag Rake receiver performs relatively better. Such analysis applies, for example, to ultra-wideband (UWB) radio frequency channels and underwater wideband acoustic channels.

We study the correlation structure of the scale-lag Rake fingers and show that the *normalized scale spread* parameter relates directly to the time-variability of the

channel. We discover that much of the channel energy is concentrated in few eigenmodes and hence propose principal components combining for a reduced-complexity solution. Finally, we perform physical experiments in the air-acoustic channel to demonstrate the applicability of the wideband channel model.

Dedicated to Ruth Ann

ACKNOWLEDGMENTS

There are many people who have helped in all aspects of my life, and particular throughout this course of study. To begin, I wish to thank Mrs. Taylor, my first grade teacher, who helped me develop a love for reading. In fourth grade, I transferred to the "smart school" at the other end of the county. That experience helped me develop independence as I found new friends and rode the city bus to school every day (which also helped me develop a severe case of mono). Unfortunately, I cannot think of any notable achievements during my junior high years—unless you count survival. In high school, Mr. Jackson instilled the desire to understand the physical world around me through such projects as the constant velocity machine. I'll never forget the day we blew the windows out of the physics room by exploding hydrogen-oxygen balloons. Mr. Orem, my humanities teacher, showed me that there is more to life than numbers and formulas.

At the ripe old age of 19, I spent two years on a church proselyting mission in the beautiful country of Austria. I want to thank my mission trainer, Elder Russell, for teaching me to work. President Swensen and my companions also helped me strengthen my faith. Faith has always played an integral part in my pursuit of knowledge and wisdom.

Through my college years, there are several experiences that stand out. Uncle Chuck, Dr. Furse, and Dr. Moon each contributed to my education at Utah State in

a unique way. Uncle Chuck persuaded me to switch majors from Physics to Electrical Engineering (we spent hours discussing my life over pizza at Chuck & Melanie's house). Dr. Furse made electromagnetics fun and accessible. Dr. Moon, thanks to his example, challenged me to branch out into communications. He taught me that if something seems hard, then you are probably doing it wrong. My favorite math professor, Ian Anderson, used to say "a word to the wise—is sufficient."

I would like to thank my colleagues in the IPS Lab at Ohio State and my dissertation committee. Their support and insights have been invaluable. My advisor, phil schniter, was unbelievably active and superb in guiding me through research and writing. He consistently amazed me with his quick and insightful responses. I also enjoyed a few seasons of ultimate frisbee with phil. My ankle gave out long before my will to play. I would also like to thank Hesham El Gamal. He taught me to seek difficult problems and find opportunities where others see challenges. Ananthram Swami, my external committee member from Army Research Labs, graciously hosted me for a very productive short internship in Maryland. Many of the key ideas for my dissertation initiated from that experience. I would also like to thank the Ohio Space Grant Consortium for supporting me during my Ph.D. and helping me feel like a real space cadet.

My friends and members of my church congregation have made our stay in Ohio the best ever! Special thanks to Coach Sundberg and the gang: Bill, Heidi, and Thomas. We will miss them. We couldn't have survived our last year without Jeremy and April Johnson—our line-of-sight neighbors.

I reserve an unmeasurable amount of gratitude to my parents and siblings. My mother was a tremendous inspiration as we raced to see who would obtain the first

Margetts Ph.D. She beat me by a few months. My Big Bad Dad is the wisest, friendliest, most considerate, and spiritually connected man I know. I aspire to have his wit and wisdom. My Momma-in-law, Mary Eggli, provided moral support and plenty of care packages to ease the tension.

Finally, I would like to thank my beautiful wife Ruth Ann. I am tremendously indebted to her for following me to Ohio. For the past few years, I'm not sure who helped whom more—me with her law-school homework or her with her persistent encouragement to make my deadlines. This experience has taught us that out of difficulties come great rewards.

I thank everyone who has helped.

VITA

April, 1975	Born - Bountiful, Utah
May, 2000	B.S. Electrical Engineering and Mathematics, Utah State University
Dec., 2002	M.S. Electrical Engineering, The Ohio State University
2003-present	Doctoral Student, The Ohio State University.

PUBLICATIONS

Research Publications

Adam R. Margetts and Phil Schniter. Adaptive chip-rate equalization of downlink multirate wideband CDMA. *IEEE Trans. on Signal Processing*, 53(6):2205–2215, Jun. 2005.

Adam R. Margetts and Philip Schniter. On the correlation structure of wideband scale-lag rake fingers. *Proc. IEEE Workshop on Signal Processing Advances in Wireless Communication*, Jun. 2005.

Adam R. Margetts, Philip Schniter, and Ananthram Swami. Scale-lag diversity reception in mobile wideband channels. *Proc. IEEE Internat. Conf. on Acoustics, Speech, and Signal Processing*, Mar. 2005.

Adam R. Margetts and Philip Schniter. Joint scale-lag diversity in mobile wideband communication systems. *Proc. Asilomar Conf. on Signals, Systems and Computers*, Nov. 2004.

Adam R. Margetts and Phil Schniter. Chip-rate adaptive two-stage receiver for scrambled multirate CDMA downlink. *Proc. Asilomar Conf. on Signals, Systems and Computers*, Nov. 2003.

Adam R. Margetts and Phil Schniter. Adaptive inter-chip interference cancellation of multirate scrambled CDMA downlink. *Proc. Allerton Conf. on Communication, Control, and Computing*, Oct. 2003.

Phil Schniter and Adam R. Margetts. Adaptive chip-rate equalization of downlink multirate wideband CDMA. *Proc. Asilomar Conf. on Signals, Systems and Computers*, Nov. 2002.

FIELDS OF STUDY

Major Field: Electrical and Computer Engineering

Studies in:

Wireless Communications	Prof. Philip Schniter
Wireless Communications	Prof. Hesham El Gamal
Control Theory	Prof. Andrea Serrani

TABLE OF CONTENTS

Page

Abstract ii

Dedication iv

Acknowledgments v

Vita viii

List of Tables xiii

List of Figures xiv

Chapters:

1. Introduction 1

    1.1 Outline and Contributions 3

2. Background 6

    2.1 Direct Sequence Spread Spectrum (DSSS) Signal 6
    2.2 Wireless Time-Varying Channel Model 10
        2.2.1 Narrowband Baseband Channel Model 11
        2.2.2 Wideband Channel Model 17
    2.3 Rake Receiver 19
        2.3.1 Fading and Diversity 22
    2.4 Previous Work 29
        2.4.1 Wideband Systems 29
        2.4.2 Narrowband and Wideband Canonical Models 33

3. Scale-Lag Rake Receiver 42

3.1 Scale-Lag Resolution 42
3.1.1 Discussion 51
3.2 Choice of Basis Functions 52
3.2.1 Low-Complexity Scale-Lag Rake Implementation 54
3.3 Connection to Radar, Sonar, and Wavelets 58
3.4 Appendix: Proof of Propositions 1 and 2 59
3.5 Appendix: Wideband Ambiguity Function for Second-Derivative Chip Pulse 63
3.6 Appendix: Admissibility of DSSS Waveform 64

4. Frame Theory and the Scale-Lag Rake Receiver 65

4.1 Introduction to Frame Theory 65
4.1.1 Tight Frames 67
4.1.2 Snug Frames 67
4.2 Average Frame Bounds for DSSS Signal 67
4.3 Average Frame Bounds for DSSS Signals Using Second-Derivative Gaussian Wavelets as Chip Pulses 70

5. Scale-Lag Diversity 75

5.1 Wideband Scattering Function 75
5.2 Wideband Channel Coefficient Correlation 80
5.3 Numerical Results 81

6. Rake Receiver Finger Correlation Structure 94

6.1 Narrowband Baseband-Equivalent Model 95
6.1.1 Doppler-Lag Rake Receiver 96
6.1.2 Narrowband Channel Coefficients 96
6.1.3 Narrowband Channel Correlation 97
6.2 Wideband Model 99
6.2.1 Wideband Channel Autocorrelation 99
6.2.2 Autoregressive Model for Scale-Lag Channel Coefficients . . 102
6.2.3 Principal Components Combining 103
6.2.4 Acoustic Experiments 106

7. Conclusions and Future Research 116

Appendices:

A. Real-Valued Doppler-lag Basis 120

A.1 Doppler-Lag Basis Function Inner Product 120
A.2 Second-Derivative Gaussian Chip Pulse 123

B. Narrowband Scattering Function 125

B.1 Derivation 125
B.1.1 Assumptions 126
B.1.2 Ring of Scatterers 127

Bibliography 130

LIST OF TABLES

Table		Page
1.1	Acronyms used in the Dissertation.	5
2.1	Outline of various quantities.	9
2.2	Time-frequency and time-scale characterization functions for the one path Doppler-lag and one path scale-lag channels. [81, p. 51]	20
3.1	Outline of scale-lag resolution quantities.	51
4.1	Frame bounds for $a_o = 2$.	73
4.2	Frame bounds for $a_o = 1 + 1/64$.	73
4.3	Frame bounds for $a_o = 1 + 1/128$.	74

LIST OF FIGURES

Figure **Page**

2.1 Spectrum of (a) narrowband baseband-equivalent signal modulated to a carrier frequency of f_c, and (b) wideband signal. 10

2.2 (a) Narrowband system with complex baseband-equivalent signal $\tilde{s}(t)$, carrier frequency f_c, and low-pass filter $G(f)$. (b) Wideband system. The passband time-varying system kernel is $h(t, \tau)$. 11

2.3 Single-path time-varying channel. 15

2.4 Eigenvalue profile for $N = 1, 2, 4, 8$ channels. The eigenvalues are normalized to unity for each profile. 27

2.5 Average BER versus SNR for coherent binary phase-shift keying (BPSK) in Gaussian noise. Dashed lines indicate BER performance of uniformly-valued eigenvalues and solid lines indicate BER performance of exponentially-decaying eigenvalues. 28

2.6 FCC spectral mask for handheld UWB devices. 30

2.7 Sampling the scale-lag plane. 40

3.1 (a) Waveform $x(t)$. (b) Waveform $x(t)$ dilated by a. 44

3.2 Plot of (a) $p(t)$ (time domain) and (b) $P(f)$ (frequency domain) for the second-derivative Gaussian chip pulse, a.k.a. Mexican hat wavelet, defined in (3.3). 46

3.3 Approximate wideband ambiguity function $\bar{\chi}(a, \tau)$ with a second-derivative Gaussian chip pulse (3.3). 48

3.4 Deterministic wideband ambiguity function $\chi(a,\tau)$ of a DSSS waveform $x(t)$ composed of a length-128 i.i.d. random binary sequence modulating second-derivative Gaussian chip pulses. The chip-pulse spacing is chosen to be $T_o = \frac{2}{f_o}$. 49

3.5 Plot of (a) $\bar{\chi}(a,0)$ and (b) $\bar{\chi}(1,\tau)$ for DSSS waveform employing second-derivative Gaussian chip-pulses. 50

3.6 Sampling the scale-lag plane. 54

3.7 Block-diagram for the scale-lag Rake projection given by equation (3.13). The receiver can easily be made causal by introducing an appropriate bulk delay in the matched filter. 56

4.1 Ratio of average frame bounds B/A for a DSSS signal employing second-derivative Gaussian wavelet chip pulses. 74

5.1 Plot of "bathtub-shaped" scale profile $p_A(a)$. The angle of arrival ξ is uniformly distributed. 79

5.2 For the scale-spread of $\gamma_{max} T_s f_o = 0.05$, we compare the eigenvalues and BER of the scale-lag Rake receiver for translation-spacing relation k_τ settings of (a) $k_\tau = 0.236$ (minimum resolvable lag), (b) $k_\tau = 0.744$, (c) $k_\tau = 2$. The Eigenvalue curves are indexed from right to left over scale-spacings of $k_\gamma = 0.55$ (minimum scale resolution), $k_\gamma = 1$, and $k_\gamma = 2$. The BER curves are indexed in the opposite ordering. The normalized delay spread is $\tau_{max} f_o = 0.5$. A "bathtub-shaped" scale profile (5.10) is used. 86

5.3 For the scale-spread of $\gamma_{max} T_s f_o = 0.0005$, we compare the eigenvalues and BER of the scale-lag Rake receiver for translation-spacing relation k_τ settings of (a) $k_\tau = 0.236$ (minimum resolvable lag), (b) $k_\tau = 0.744$, (c) $k_\tau = 2$. The Eigenvalue curves are indexed from right to left over scale-spacings of $k_\gamma = 0.55$ (minimum scale resolution), $k_\gamma = 1$, and $k_\gamma = 2$. The BER curves are indexed in the opposite ordering. The normalized delay spread is $\tau_{max} f_o = 0.5$. A "bathtub-shaped" scale profile (5.10) is used. . . 87

5.4 For the scale-spread of $\gamma_{max}T_sf_o = 0.05$, we compare the eigenvalues and BER of the scale-lag Rake receiver for scale-spacing relation k_γ settings of (a) $k_\gamma = 0.55$ (minimum scale resolution), (b) $k_\gamma = 1$, (c) $k_\gamma = 2$. The Eigenvalue curves are indexed from right to left over translation-spacings of $k_\tau = 0.236$ (minimum resolvable lag), $k_\tau = 0.744$, $k_\tau = 1$ and $k_\tau = 2$. The BER curves are indexed in the opposite ordering. The normalized delay spread is $\tau_{max}f_o = 0.5$. A "bathtub-shaped" scale profile (5.10) is used. . . 88

5.5 For the scale-spread of $\gamma_{max}T_sf_o = 0.0005$, we compare the eigenvalues and BER of the scale-lag Rake receiver for scale-spacing relation k_γ settings of (a) $k_\gamma = 0.55$ (minimum scale resolution), (b) $k_\gamma = 1$, (c) $k_\gamma = 2$. The Eigenvalue curves are indexed from right to left over translation-spacings of $k_\tau = 0.236$ (minimum resolvable lag), $k_\tau = 0.744$, $k_\tau = 1$ and $k_\tau = 2$. The BER curves are indexed in the opposite ordering. The normalized delay spread is $\tau_{max}f_o = 0.5$. A "bathtub-shaped" scale profile (5.10) is used. . . 89

5.6 For the scale-spacing relation $k_\gamma = 0.55$ (set to minimum scale resolution) and translation-spacing relation $k_\tau = 0.236$ (set to minimum resolvable lag), we compare the eigenvalues and BER performances of the three receivers for scale-spreads of (a) $\gamma_{max}T_sf_o = 0.05$, (b) $\gamma_{max}T_sf_o = 0.005$, (c) $\gamma_{max}T_sf_o = 0.0005$. The Eigenvalue curves are indexed from right to left as the scale-lag Rake, Doppler-lag Rake, and lag-only Rake. The BER curves are indexed in the opposite ordering. The normalized delay spread is $\tau_{max}f_o = 0.5$. A "bathtub-shaped" scale profile (5.10) is used. 90

5.7 For the scale-spacing relation $k_\gamma = 0.55$ (set to minimum scale resolution) and translation-spacing relation $k_\tau = 2$, we compare the eigenvalues and BER performances of the three receivers for scale-spreads of (a) $\gamma_{max}T_sf_o = 0.05$, (b) $\gamma_{max}T_sf_o = 0.005$, (c) $\gamma_{max}T_sf_o = 0.0005$. The Eigenvalue curves are indexed from right to left as the scale-lag Rake, Doppler-lag Rake, and lag-only Rake. The BER curves are indexed in the opposite ordering. The normalized delay spread is $\tau_{max}f_o = 0.5$. A "bathtub-shaped" scale profile (5.10) is used. 91

5.8 For the scale-spacing relation $k_\gamma = 0.55$ (set to minimum scale resolution) and translation-spacing relation $k_\tau = 0.236$ (set to minimum resolvable lag), we show the eigenvalues and BER for (a) scale-lag Rake, (b) Doppler-lag Rake, and (c) lag-only Rake. The Eigenvalue curves are indexed from right to left via the normalized scale spread $\gamma_{max} T_s f_o = 0.05, 0.005, 0.0005$, respectively. The BER curves are indexed in the opposite ordering. The normalized delay spread is $\tau_{max} f_o = 0.5$. A "bathtub-shaped" scale profile (5.10) is used. 92

5.9 For the scale-spacing relation $k_\gamma = 0.55$ (set to minimum scale resolution) and translation-spacing relation $k_\tau = 2.0$, we show the eigenvalues and BER for (a) scale-lag Rake, (b) Doppler-lag Rake, and (c) lag-only Rake. The Eigenvalue curves are indexed from right to left via the normalized scale spread $\gamma_{max} T_s f_o = 0.05, 0.005, 0.0005$, respectively. The BER curves are indexed in the opposite ordering. The normalized delay spread is $\tau_{max} f_o = 0.5$. A "bathtub-shaped" scale profile (5.10) is used. 93

6.1 (Solid lines) Channel coefficient autocorrelation sequence $\mathrm{E}[h^{(0)}_{m,n} h^{(k')}_{m',n'}]$ for $m = m' = 0$, and $n = n' = 0$. (Dashed lines) Damped Bessel function approximation: $J_0\left(2\pi\gamma_{\max} f_o T_s k'\right) e^{-\gamma_{\max} f_o T_s |k'|}$. The normalized delay spread is $\tau_{\max} f_o = 0.5$. 101

6.2 BER performance of scale-lag Rake receiver using PCC with various values of K_{pcc}. Same setup as in Fig. 5.6(b). 105

6.3 Zoomed view of a typical wideband DSSS transmit waveform. 107

6.4 (a) Deterministic lag autocorrelation of a typical wideband DSSS transmit waveform realization: $\chi(1, \tau) = \langle x(t), x(t-\tau) \rangle$. (b) Zoomed view. 108

6.5 (a) Deterministic dilation autocorrelation of a typical wideband DSSS transmit waveform realization: $\chi(a, 0) = \langle x(t), \frac{1}{\sqrt{a}} x(\frac{t}{a}) \rangle$. (b) Zoomed view. . . . 109

6.6 Time-invariant transfer function of an acoustic channel. The x-axis is lag (in seconds) and the y-axis is time (in seconds). 112

6.7 (a) Delay spread at time zero. (b) Channel coefficients $r^{(k)}_{0,0}$ and $r^{(k)}_{1,0}$ for a fixed receiver. 113

6.8 Time-varying transfer function of acoustic channel. The x-axis is lag (in seconds) and the y-axis is time (in seconds). 114

6.9 (a) Delay spread at time zero. (b) Channel coefficients $r_{0,0}^{(k)}$ and $r_{1,0}^{(k)}$ for a mobile receiver. The dashed line is $\mathrm{E}[h_{0,0}^{(0)} h_{0,0}^{(k)}]$ for a normalized scale spread of $\gamma_{\max} f_o T_s = 0.0381$, corresponding to a mobile speed of 1 in./second. . . 115

B.1 Plot of "bathtub-shaped" Doppler-frequency profile $p_\Theta(\theta)$. The angle of arrival ξ is uniformly distributed. 129

CHAPTER 1

INTRODUCTION

Wideband communication systems are defined by a ratio of single-sided bandwidth to center frequency in excess of 0.20 [92] [20]. We are interested in studying the effect of mobility (i.e., temporal variation in the physical geometries between transmitter, receiver, and scatterers) on wideband communications systems and in designing transceivers capable of leveraging the potential diversity gains that result from multipath propagation in mobile environments.

First, it is important to note that the combined effects of multipath and mobility on wideband systems are quite different than those on their narrowband counterparts. For example, in narrowband systems with a dense ring of scatterers surrounding the receiver, mobility imparts a spreading of the signal in the frequency-domain that is commonly referred to as Doppler spreading [75, p. 809]. Considering a wideband system employing orthogonal frequency division multiplexing (OFDM)[1] with narrow subcarrier bandwidths in the same physical environment, mobility implies that each subcarrier signal will experience Doppler spreading, but the amount of spreading will vary from one subcarrier to the next [83]. In wideband communication systems

[1]For a listing of all acronyms used in the text, see Table 1.1.

employing direct sequence spread spectrum (DSSS)—the focus of this manuscript—the effects of mobility in the multipath mobile environment are not well described by frequency-domain spreading, but rather by *scale spreading*. Note that scale-spreading is actually a general concept that applies to both narrowband and wideband systems. For example, changing the time scale of a single sinusoid is equivalent to shifting the signal in frequency. By scale spreading, we mean that several copies of the transmitted signal combine at the receiver, each with a different dilation of the time support of the original signal. In addition, each copy may be temporally delayed by a different amount.

When the different propagation paths are characterized by independent dilations and delays, the fading inherent to multipath propagation can be mitigated by using diversity reception. For wideband DSSS signaling, we propose a *scale-lag Rake receiver* that extracts this diversity.[2] The scale-lag Rake employs a basis composed of shift-dilates of the transmitted waveform in order to match the scale-lag spreading induced by the wideband channel. In general, the transmit waveform could be designed to optimally extract the scale-lag diversity; however, for practical considerations, we constrain the transmit waveform to be a DSSS signal.

We investigate, through frame-theoretic tools, the translation- and dilation-spacing parameters of a scale-lag Rake basis, and compare the performances of a *scale-lag* Rake and a *Doppler-lag* Rake [85], each capable of leveraging the diversity that results from mobility. When the translation spacing of the Rake functions is equal to the minimum resolvable lag, there is no significant performance difference between

[2]The possibility of a scale-lag receiver was mentioned in [5], but no details were developed.

the receivers. For wider spacings, the receiver is more reliant on dilation diversity; hence, the scale-lag Rake receiver performs relatively better.

The analysis can be applied to radio frequency ultra-wideband (UWB) systems [101] as well as to underwater acoustic systems [26].

1.1 Outline and Contributions

The background chapter and main contributions are outlined as follows. (The main results of this dissertation are documented in [63], [64], [65], and [66].)

Background (Chapter 2)

After introducing the direct-sequence spread-spectrum (DSSS) waveforms used in this dissertation, we review the time-varying channel and discuss the narrowband baseband model and the wideband model. We analyze the Rake receiver and define fading and diversity reception. Previous work in electromagnetic and underwater acoustic is reviewed with a specific discussion of the narrowband canonical model [85] and wideband canonical model [5].

Scale-Lag Rake Receiver (Chapter 3)

We define the scale resolution for a DSSS signal and specify scale-lag basis functions to be used in the scale-lag Rake receiver. We derive close approximations for the wideband ambiguity function, and we propose a reduced-complexity scale-lag Rake receiver. Finally, we show connections to Radar, Sonar, and wavelets.

Frame Theory and the Scale-Lag Rake Receiver (Chapter 4)

After a brief introduction to frame theory, we define and analyze average frame-bounds for a DSSS waveform. We use the average frame bounds as a guideline for determining the translation and scale spacing of the scale-lag basis used in Chapter 5. We provide numerical average frame bound results for a DSSS waveform using a second-derivative Gaussian chip pulse.

Scale-Lag Diversity (Chapter 5)

We derive the wideband scattering function, which quantifies the statistics of the energy spread across dilation and delay, and make a numerical performance comparison of the scale-lag Rake receiver with the Doppler-lag Rake and conventional lag-only Rake receiver. The numerical results use a second-derivative Gaussian chip-pulse.

Rake Receiver Finger Correlation Structure (Chapter 6)

We study the time-variation of the scale-lag Rake receiver channel coefficients. This is done by computing the autocorrelation between time-samples of scale-lag Rake fingers. We find that the Rake fingers are approximately stationary for short periods of time and that the amount of variation is inversely proportional to the wideband channel scale spread. Chapter 6 also investigates the principal components combiner, which learns and tracks the low dimensional signal eigenspace. Finally, we provide acoustic experiments to study the wideband channel.

Conclusions (Chapter 7)

In Chapter 7 we provide a short conclusion and suggest future research directions.

ADC	Analog to Digital Converter
AR	Auto Regressive
AWGN	Additive White Gaussian Noise
BEM	Basis Expansion Model
BER	Bit Error Rate
BPSK	Binary Phase Shift Keying
CSI	Channel State Information
CWT	Continuous Wavelet Transform
DAC	Digital to Analog Converter
DC	Direct Current
DSSS	Direct-Sequence Spread-Spectrum
FCC	Federal Communications Commission
FDTD	Finite Difference Time Domain
GHz	Gigahertz
IEEE	Institute of Electrical and Electronics Engineers
ISI	Inter-Symbol Interference
LPF	Low-Pass Filter
LMS	Least Mean Squares Algorithm
MAP	Maximum A Posteriori
MHz	Megahertz
MMSE	Minimum Mean Squared Error
MRC	Maximal Ratio Combining
MSE	Mean Squared Error
OFDM	Orthogonal Frequency Division Multiplexing
PCC	Principal Components Combining
PN	Pseudo Noise
RF	Radio Frequency
RLS	Recursive Least Squares Algorithm
RX	Receiver
SNR	Signal to Noise Ratio
TX	Transmitter
UWAC	Underwater Wideband Acoustic Communications
UWB	Ultra-Wideband

Table 1.1: Acronyms used in the Dissertation.

CHAPTER 2

BACKGROUND

In this chapter, we introduce the direct-sequence spread-spectrum (DSSS) waveforms used in this dissertation and review the time-varying channel. We discuss the narrowband baseband-equivalent model and the wideband model. We analyze the conventional Rake receiver and define fading and diversity reception. Previous work in electromagnetic and underwater acoustic is reviewed with a specific discussion of the narrowband canonical model [85] and wideband canonical model [5].

2.1 Direct Sequence Spread Spectrum (DSSS) Signal

The text has referred several times to Direct Sequence Spread Spectrum (DSSS) signaling without a proper definition. In this section, we define the narrowband and wideband DSSS waveforms and the information bearing transmit waveforms.

There are two main differences between narrowband and wideband signals. First, the obvious difference is that the narrowband signal occupies much less bandwidth than the wideband signal. We say that the narrowband signal operates in bandwidth-limited regime, while the wideband signal operates in a power-limited regime (see [95] for a discussion on the information-theoretic impacts of operating in either regime).

Second, the wideband signal is directly transmitted at baseband, i.e., it is not modulated to a carrier frequency, while the narrowband signal has a complex-valued baseband-equivalent representation that is modulated to a passband by a carrier sinusoid before transmission. Both of these differences are illustrated by Fig. 2.1, which shows the spectra of typical narrowband and wideband transmit signals. Our contributions concern mainly wideband signals, but we introduce narrowband signals to provide background for the discussion of previous work and to motivate our research.

In the following, the *narrowband baseband-equivalent* quantities are denoted with a tilde in order to reduce confusion with *wideband* quantities. For ease of reference, the variables used throughout this chapter are outlined in Table 2.1.

- Narrowband baseband-equivalent DSSS waveform:

$$\tilde{x}(t) := \frac{1}{\sqrt{\tilde{N}_p}} \sum_{i=0}^{\tilde{N}_p-1} \tilde{c}_i \tilde{p}(t - i\tilde{T}_o) \tag{2.1}$$

- Wideband DSSS waveform:

$$x(t) := \frac{1}{\sqrt{N_p}} \sum_{i=0}^{N_p-1} c_i p(t - iT_o) \tag{2.2}$$

In the narrowband case, $\tilde{p}(t)$ is the narrowband baseband-equivalent *chip* waveform; $\{\tilde{c}_i\}_{i=0}^{\tilde{N}_p-1}$ is the narrowband pseudorandom (PN) *chip sequence* with $c_i \in \{-1, 1\}$; $\tilde{N}_p$ is the number of narrowband chips; $\tilde{T}_o$ is the narrowband chip spacing. In the wideband case, $p(t)$ is the wideband *chip pulse*; $\{c_i\}_{i=0}^{N_p-1}$ is the wideband PN *chip-pulse sequence*, where $c_i \in \{-\frac{1}{\sqrt{q}}, 0, \frac{1}{\sqrt{q}}\}$, and q is the probability of a non-zero chip so that $\mathrm{E}[c_i^2] = 1$; N_p is the number of wideband chip pulses; and T_o is the wideband chip-pulse spacing. We refer to $\tilde{p}(t)$ as a *chip* and to $p(t)$ as a *chip pulse*.

We assume the chip $\tilde{p}(t)$ is approximately band-limited to $\tilde{W}$ Hertz (double-sided) and is approximately time-limited to $\tilde{T}_p$ seconds. Likewise, we assume the chip pulse $p(t)$ is approximately band-limited to W Hertz (single-sided) and is approximately time-limited to T_p seconds. We define f_o to be the frequency of the spectral peak of the wideband chip pulse.

For the wideband case, a discussion on the construction of ternary sequences see [4, 17, 16, 102]. In [68], the authors study spreading sequences specifically for UWB systems; the spreading sequences in this thesis are randomly chosen to facilitate the analysis.

The DSSS waveforms are linearly modulated by information bits to create the following transmit signals:

- Narrowband baseband-equivalent transmit signal:

$$\tilde{s}(t) := \sum_{k=0}^{N_b-1} b_k \tilde{x}(t - iT_s) \tag{2.3}$$

- Wideband transmit signal:

$$s(t) := \sum_{k=0}^{N_b-1} b_k x(t - iT_s) \tag{2.4}$$

where T_s is the DSSS waveform duration; $\{b_k\}$ are the bits with $b_k \in \{-\sqrt{E_b}, \sqrt{E_b}\}$, E_b is the energy per bit; and N_b is the number of transmitted bits.

In general, we define $s(t)$ as the signal output of the transmit antenna; hence, for the narrowband case $s(t) = \mathrm{Re}\{\tilde{s}(t)e^{j2\pi f_c t}\}$ where f_c is the carrier frequency. The transmit spectrum of example narrowband and wideband waveforms are shown in Fig. 2.1.

Quantity	Description
$\tilde{x}(t)$	Narrowband baseband-equivalent DSSS waveform.
$\tilde{p}(t)$	Narrowband baseband-equivalent chip waveform.
$\{\tilde{c}_i\}$	Narrowband PN chip sequence, $\tilde{c}_i \in \{-1, 1\}$.
$\tilde{N}_p$	Number of chips in narrowband PN sequence. $\tilde{N}_p := \frac{\tilde{T}_s}{\tilde{T}_o}$
$\tilde{T}_o$	Chip spacing for narrowband baseband-equivalent DSSS waveform.
$\tilde{T}_p$	Approximate duration of narrowband baseband-equivalent chip.
$\tilde{W}$	Approximate double-sided chip bandwidth.
N_b	Number of transmitted bits.
$\{b_k\}$	Transmitted bits, $b_k \in \{\sqrt{E_b}, -\sqrt{E_b}\}$, where E_b is the energy per bit.
T_s	DSSS waveform duration, same for wideband and narrowband signals.
$x(t)$	Wideband DSSS waveform.
$p(t)$	Wideband chip pulse.
$\{c_i\}$	Wideband PN chip-pulse sequence, $c_i \in \{-\frac{1}{\sqrt{p}}, 0, \frac{1}{\sqrt{p}}\}$, $\mathrm{E}[c_i^2] = 1$.
N_p	Number of chip pulses in wideband PN sequence. $N_p := \frac{T_s}{T_o}$
T_o	Wideband chip-pulse spacing.
T_p	Approximate wideband chip-pulse duration.
W	Approximate single-sided bandwidth for wideband chip pulse.
f_c	Carrier frequency of narrowband passband transmit signal.
f_o	Frequency of spectral peak for wideband chip pulse.
$v_{\max}$	Velocity of mobile receiver.
c	Wave propagation speed.
$f_{\max}$	Doppler spread (single-sided) of narrowband baseband-equivalent channel.
$\tau_{\max}$	Delay spread.
$a_{\min}$	Minimum dilation of the wideband channel.
$a_{\max}$	Maximum dilation of the wideband channel.
$\gamma_{\max}$	Scale spread (single-sided) of wideband channel. $\gamma_{\max} := \frac{a_{\max} - a_{\min}}{2}$
$h(t, \tau)$	Time-varying channel.
$H(\theta, \tau)$	Passband spreading function.
$\tilde{H}(\theta, \tau)$	Baseband spreading function.
$\mathcal{L}(a, \tau)$	Wideband channel kernel.

Table 2.1: Outline of various quantities.

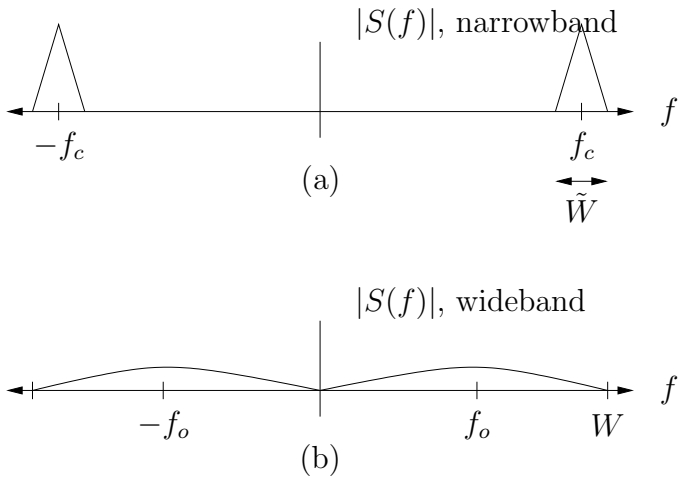

Figure 2.1: Spectrum of (a) narrowband baseband-equivalent signal modulated to a carrier frequency of f_c, and (b) wideband signal.

2.2 Wireless Time-Varying Channel Model

The input-output relationship of the time-varying wireless channel can be modeled as

$$r(t) = \int h(t,\tau)s(t-\tau)d\tau \tag{2.5}$$

where the kernel $h(t,\tau)$ is the response of the system to a impulse at time $t-\tau$ and $s(t)$ is the input signal. For now, we assume the additive noise is negligible. The time-varying impulse response $h(t,\tau)$ is the *passband* response; thus, all quantities in (2.5) are real valued. By passband, we mean that all frequencies are passed except direct current (DC), which cannot be coupled through free-space. The model (2.5) is general in that $h(t,\tau)$ depends only on the time-varying physical channel geometry and not on the input signal $s(t)$; hence, it can be used to model the input-output relationship

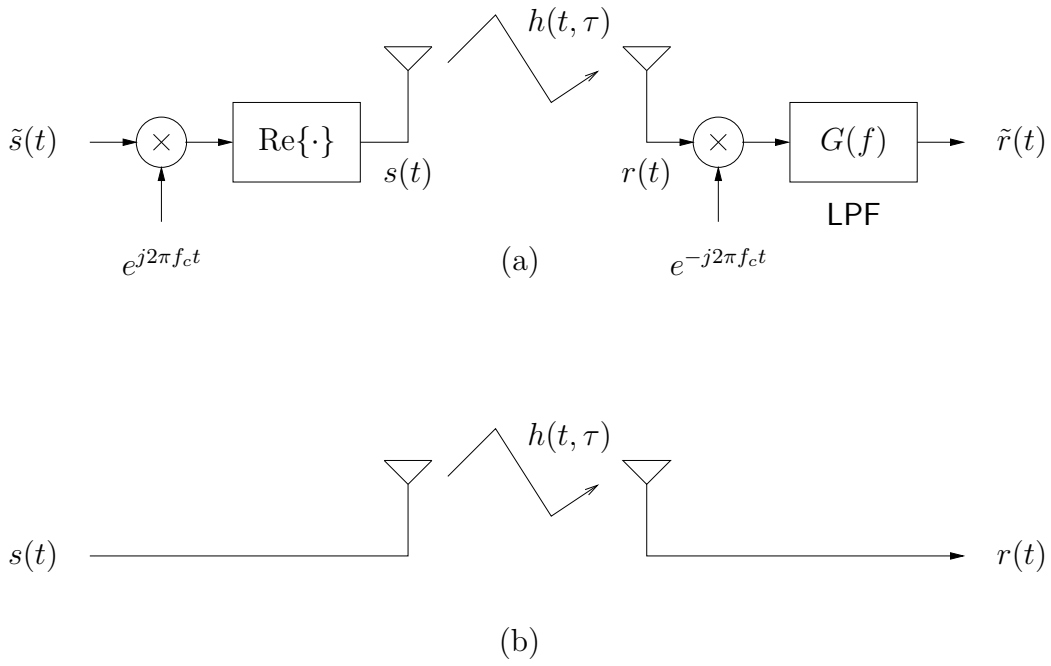

Figure 2.2: (a) Narrowband system with complex baseband-equivalent signal $\tilde{s}(t)$, carrier frequency f_c, and low-pass filter $G(f)$. (b) Wideband system. The passband time-varying system kernel is $h(t,\tau)$.

of modulated narrowband baseband-equivalent signals (see Fig. 2.2(a)) or carrier-less wideband signals (see Fig. 2.2(b)). We proceed now to derive the narrowband baseband-equivalent model. Later, we review the wideband channel model.

2.2.1 Narrowband Baseband Channel Model

We now derive the time-varying *narrowband baseband-equivalent* model and point out the implicit assumptions that are often made when deriving this model from the general passband model (2.5). The channel is narrowband in the sense that the bandwidth-to-center-frequency ratio is very small. A narrowband channel in this sense can be frequency selective. Our goal is to obtain a simple expression for the

complex-valued baseband signal, $\tilde{r}(t)$ in terms of the complex-valued baseband input $\tilde{s}(t)$, which has double-sided bandwidth of $\tilde{W} \ll f_c$. Along the way, we point out assumptions that are often implicit in the literature.

From Fig. 2.2(a), the spectrum of the demodulated-filtered received signal $\tilde{r}(t)$ is easily seen to be

$$\tilde{R}(f) = G(f)R(f + f_c), \tag{2.6}$$

where $R(f)$ is the spectrum of the received passband signal, whose time function $r(t)$ is written

$$\begin{aligned}
r(t) &= \int h(t,\tau)s(t-\tau)d\tau, && (2.7)\\
&= \int h(t,\tau)\,\mathrm{Re}\{\tilde{s}(t-\tau)e^{j2\pi f_c(t-\tau)}\}d\tau, && (2.8)\\
&= \int\int H(\theta,\tau)e^{j2\pi\theta t}\,\mathrm{Re}\{\tilde{s}(t-\tau)e^{j2\pi f_c(t-\tau)}\}d\theta d\tau, && (2.9)\\
&= \int\int \frac{1}{2}H(\theta,\tau)e^{-j2\pi f_c\tau}\tilde{s}(t-\tau)e^{j2\pi(f_c+\theta)t}d\theta d\tau\\
&\quad + \int\int \frac{1}{2}H(\theta,\tau)e^{j2\pi f_c\tau}\tilde{s}^*(t-\tau)e^{-j2\pi(f_c-\theta)t}d\theta d\tau, && (2.10)
\end{aligned}$$

where $H(\theta,\tau)$ is the *passband spreading function* obtained by taking the Fourier transform of $h(t,\tau)$ with respect to the time variable t. We proceed by taking the Fourier transform of the received signal (2.10)

$$\begin{aligned}
R(f) &= \int\int \frac{1}{2}H(\theta,\tau)\tilde{S}(f-f_c-\theta)e^{-j2\pi(f-\theta)\tau}d\theta d\tau\\
&\quad + \int\int \frac{1}{2}H(\theta,\tau)\tilde{S}^*(-f-f_c+\theta)e^{-j2\pi(f-\theta)\tau}d\theta d\tau, && (2.11)
\end{aligned}$$

and substitute (2.11) into (2.6) to obtain the spectrum of the demodulated-filtered received signal

$$\begin{aligned}\tilde{R}(f) &= \int\int \frac{1}{2}H(\theta,\tau)e^{-j2\pi f_c\tau}G(f)\tilde{S}(f-\theta)e^{-j2\pi(f-\theta)\tau}d\theta d\tau \\ &\quad + \int\int \frac{1}{2}H(\theta,\tau)e^{-j2\pi f_c\tau}G(f)\tilde{S}^*(-f-2f_c+\theta)e^{-j2\pi(f-\theta)\tau}d\theta d\tau \quad (2.12) \\ &= \int\int \tilde{H}(\theta,\tau)G(f)\tilde{S}(f-\theta)e^{-j2\pi(f-\theta)\tau}d\theta d\tau \\ &\quad + \int\int \tilde{H}(\theta,\tau)G(f)\tilde{S}^*(f-2f_c+\theta)e^{-j2\pi(f-\theta)\tau}d\theta d\tau, \quad (2.13)\end{aligned}$$

where $\tilde{H}(\theta,\tau) = \frac{1}{2}H(\theta,\tau)e^{-j2\pi f_c\tau}$ is the *baseband spreading function*. In order to simplify (2.13), we make the following narrowband baseband-equivalent channel assumption.

(A0) Assume that $\tilde{H}(\theta,\tau)$ has compact support in the θ variable, that is, $H(\theta,\tau) = 0$, $\forall\tau$, $|\theta| > f_{\max}$ for some $f_{\max} \ll \frac{\tilde{W}}{2}$, which we call the single-sided *maximum Doppler spread*. Note that $\tilde{H}(\theta,\tau)$ has the same θ-support as $H(\theta,\tau)$.

Assumption (A0) allows us to eliminate the double frequency term in (2.13) since the lowpass filter $G(f)$ and $\tilde{S}(f-2f_c+\theta)$ have non-overlapping frequency support. We now have

$$\tilde{R}(f) \approx \int\int \tilde{H}(\theta,\tau)G(f)\tilde{S}(f-\theta)e^{-j2\pi(f-\theta)\tau}d\theta d\tau. \quad (2.14)$$

Our next assumption is that the lowpass filter $G(f)$ is unity across the band $[-\tilde{W}/2 - f_{\max},\ \tilde{W}/2 + f_{\max}]$, and zero elsewhere; hence, (2.14) can be written

$$\tilde{R}(f) \approx \int\int \tilde{H}(\theta,\tau)\tilde{S}(f-\theta)e^{-j2\pi(f-\theta)\tau}d\theta d\tau, \quad (2.15)$$

and

$$\tilde{r}(t) \approx \int\int \tilde{H}(\theta,\tau)\tilde{s}(t-\tau)e^{j2\pi\theta t}d\theta d\tau, \tag{2.16}$$

$$\approx \int \tilde{h}(t,\tau)\tilde{s}(t-\tau)d\tau. \tag{2.17}$$

where $\tilde{h}(t,\tau) = \frac{1}{2}h(t,\tau)e^{-j2\pi f_c\tau}$. We have achieved our goal: (2.17) is the narrowband baseband-equivalent model.

To gain insight into the compact-support narrowband assumption, we give the following example.

Single-Path Example

Assume there is only one signal path between a fixed transmitter and a mobile receiver, e.g., see Fig. 2.3. Hence, the received passband signal can be written

$$r(t) = \int h(t,\tau)s(t-\tau)d\tau + w(t), \tag{2.18}$$

$$= h'(t)s(t-\tau'(t)) + w(t). \tag{2.19}$$

where $h'(t)$ is the real-valued time-varying attenuation, $\tau'(t)$ is the time-varying delay, and $w(t)$ is additive white Gaussian noise with double-sided power density of σ_w^2, i.e., $\mathrm{E}[w(t)w(t-\tau)] = \sigma_w^2\delta(t-\tau)$. We now make the following assumptions:

(A1) Over the time epochs considered in wireless communications, the real-valued attenuation $h'(t)$ is assumed to be constant: $h'(t) \approx h'$, for some h'.

(A2) At time zero, define the component of mobile velocity in the direction of the incoming signal path to be $v_{\max}\cos(\xi')$, where $v_{\max}$ is the mobile velocity and ξ' is the angle between the direction of mobile velocity and the incoming signal

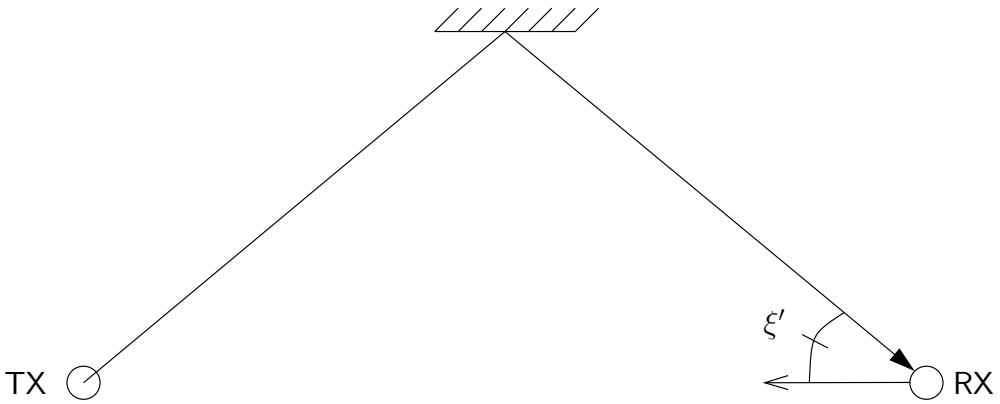

Figure 2.3: Single-path time-varying channel.

path (see Fig. 2.3). We make the simplifying assumption that the time-varying delay $\tau'(t)$ can be modeled as $\tau'(t) \approx \tau'(0) - \frac{v_{\max}\cos(\xi')}{c}t$, where c is the speed of wave propagation in the medium. This assumption is as if the mobile is traveling with velocity $v_{\max}\cos(\xi')$ in the direction of the incoming path.

Together, assumptions (A1) and (A2)[3] allow us to write the single-path time-varying channel output as

$$r(t) \approx h' s\left(\left(1 + \frac{v_{\max}\cos(\xi')}{c}\right)t - \tau'(0)\right) + w(t). \tag{2.20}$$

Note that assumptions (A1) and (A2) are general, in that they can be made regardless of the nature of the input signal $s(t)$. We implicitly make a strong assumption that the transfer function of the antenna is constant across all frequencies; future work would explicitly include antenna effects in the analysis.

[3]These are textbook assumptions often made for the wireless mobile channel, e.g., [90].

Focusing on the narrowband case, $s(t) = \mathrm{Re}\{\tilde{s}(t)e^{j2\pi f_c t}\}$, we have

$$r(t) \approx h' \,\mathrm{Re}\left\{\tilde{s}\left(\left(1 + \frac{v_{\max}\cos(\xi')}{c}\right)t - \tau'(0)\right)e^{j2\pi(f_c+\theta')t}e^{j2\pi\phi'}\right\} + w(t), \quad (2.21)$$

where $\theta' := \frac{v_{\max}\cos(\xi')}{c} f_c$ is the *Doppler frequency shift*, and $\phi' := -f_c\tau'(0)$ is the phase. If we assume the dilation effect on $\tilde{s}(t)$ is minimal, i.e., $\tilde{s}((1 + \frac{v_{\max}\cos(\xi')}{c})t) \approx \tilde{s}(t)$, then the received signal is approximated as

$$r(t) \approx \mathrm{Re}\left\{2H'\tilde{s}\left(t - \tau'(0)\right)e^{j2\pi(f_c+\theta')t}\right\} + w(t) \quad (2.22)$$

where $H' := \frac{1}{2}h'e^{j2\pi\phi'}$. Finally, the baseband channel output is

$$\tilde{r}(t) \;\approx\; H'\tilde{s}\left(t - \tau'(0)\right)e^{j2\pi\theta' t} + \tilde{w}(t). \quad (2.23)$$

where $\tilde{w}(t)$ is the demodulated low-pass filtered noise:

$$\tilde{w}(t) = \int w(\tau)e^{-j2\pi\tau}g(t-\tau)d\tau. \quad (2.24)$$

To show the connection with the time-varying baseband model (2.17), we write the baseband-equivalent spreading function for (2.23) as $\tilde{H}(\theta,\tau) := H'\delta(\theta-\theta')\delta(\tau-\tau'(0))$; thus, (2.23) can be re-written

$$\begin{aligned}
\tilde{r}(t) &= \int\int \tilde{H}(\theta,\tau)\tilde{s}(t-\tau)e^{j2\pi\theta t}d\theta d\tau + \tilde{w}(t), & (2.25)\\
&= \int\int H'\delta(\theta-\theta')\delta(\tau-\tau'(0))\tilde{s}(t-\tau)e^{j2\pi\theta t}d\theta d\tau + \tilde{w}(t), & (2.26)\\
&= H'\tilde{s}\left(t-\tau'(0)\right)e^{j2\pi\theta' t} + \tilde{w}(t). & (2.27)
\end{aligned}$$

The key point here is that the baseband-equivalent spreading function $\tilde{H}(\theta,\tau)$ for the single-path case has finite support in the θ-variable, that is, $|\theta'| < \frac{v_{\max}}{c}f_c := f_{\max}$. Indeed, under the above assumptions, a superposition of paths $\tilde{H}(\theta,\tau)$ will have finite

θ-support. We also make the common assumption that the delay difference between the first and last arriving paths does not exceed $\tau_{\max}$ seconds, i.e., $0 < \tau < \tau_{\max}$, for some $\tau_{\max}$ called the *delay spread*. Furthermore, we assume that the symbol duration T_s is much greater than the delay spread $\tau_{\max}$.

2.2.2 Wideband Channel Model

To motivate the wideband channel model, we extend the above single-path example to the wideband case where $s(t)$ is a carrier-less transmitted signal as in Fig. 2.2(b). In the narrowband case, the effect of dilation on the baseband message signal $\tilde{s}(t)$ was deemed insignificant; however, in the wideband case, the effect of dilation on the message signal may no longer be neglected.

We proceed by repeating (2.20) with the following notation

$$r(t) \approx l' \frac{1}{\sqrt{a'}} s\left(\frac{t-\tau'}{a'}\right), \tag{2.28}$$

where the dilation is $a' := \frac{1}{1+\frac{v_{\max}\cos(\xi')}{c}} \approx 1 - \frac{v_{\max}\cos(\xi')}{c}$, the path delay is τ', and the path attenuation is l'. We pre-multiply by $\frac{1}{\sqrt{a'}}$ to explicitly account for energy conservation.

If several paths are received, then the output of the wideband channel is a superposition modeled as:

$$r(t) = \underbrace{\int\int \mathcal{L}(a,\tau) \frac{1}{\sqrt{a}} s\left(\frac{t-\tau}{a}\right) da\, d\tau}_{\mathcal{L}\{s(t)\}} + w(t), \tag{2.29}$$

where $s(t)$ is the channel input, $\mathcal{L}(a,\tau)$ is the *wideband channel kernel* [5], and $w(t)$ is additive white Gaussian noise with two-sided power spectral density of σ_w^2. Note

that the wideband channel transformation $\mathcal{L}\{\cdot\}$ is *not* shift-invariant; hence, sinusoids are *not* eigenfunctions. This is also the case for the time-varying narrowband baseband-equivalent model. The wideband channel kernel $\mathcal{L}(a,\tau)$ quantifies the scale-lag spreading produced by the channel—the variable a corresponds to the dilation introduced by the channel, and the variable τ corresponds to the propagation delay. The wideband kernel for the single-path channel (2.28) would be written $\mathcal{L}(a,\tau) = l'\delta(a-a')\delta(\tau-\tau')$, where $\delta(\cdot)$ is the Dirac delta function. Note that, under the above assumptions, the wideband channel kernel has finite support in the dilation-variable a, i.e., $|a-1| < \frac{v_{\max}}{c}$.

Definitions

To simplify the following exposition, we assume a mobile receiver, fixed reflectors, and a fixed transmitter. Note, however, that the wideband kernel can be used to model any dynamic geometry between the transmitter, scatters, and receiver, e.g., a turbulent underwater environment with rings of scatters in motion.

In a rich scattering environment, the wideband channel kernel $\mathcal{L}(a,\tau)$ is non-zero on a continuum of points (a,τ). However, finite mobile velocity implies that the temporal dilation is bounded: $\{(a,\tau) : a_{min} < a < a_{max},\ 0 < \tau < \tau_{max}\}$, where a_{min} and a_{max} are the *minimum dilation* and *maximum dilation*, respectively, and τ_{max} is the delay spread. By convention, the time delay of the shortest path is zero lag. We reiterate the assumption that the symbol duration T_s is much larger than the delay spread, i.e., $T_s \gg \tau_{\max}$.

Relativistic effects for electromagnetic wave propagation are negligible due to low mobile velocities; hence, the minimum dilation and maximum dilation can be simplified to $a_{min} = 1 - \frac{v_{max}}{c}$ and $a_{max} = 1 + \frac{v_{max}}{c}$, respectively, where v_{max} is the maximum mobile velocity [81]. An important system parameter is the wideband *scale spread*:

$$\gamma_{max} := \frac{a_{max} - a_{min}}{2} = \frac{v_{max}}{c} = a_{max} - 1. \tag{2.30}$$

This defines the maximum deviation from unit temporal dilation. Though typical values of γ_{max} may be extremely small for mobile RF channels, we establish, in the sequel, that wideband DSSS signals can be very sensitive to this parameter.

Connection between Narrowband and Wideband Models

In [81], Rickard showed that in general the following models are equivalent

$$\begin{aligned} r(t) &= \int h(t,\tau)s(t-\tau)d\tau, & (2.31)\\ &= \int\int \mathcal{L}(a,\tau)\frac{1}{\sqrt{a}}s\left(\frac{t-\tau}{a}\right)dad\tau, & (2.32)\\ &= \int\int H(\theta,\tau)s(t-\tau)e^{j2\pi\theta t}d\theta d\tau. & (2.33) \end{aligned}$$

However, Rickard also showed that if $H(\theta,\tau)$ has finite support then $\mathcal{L}(a,\tau)$ has infinite support, and vice versa, if $\mathcal{L}(a,\tau)$ has finite support then $H(\theta,\tau)$ has infinite support. This can be seen from the equivalent single-path channels shown in Table 2.2, which is taken directly from [81, p. 51]. Hence, results for the narrowband baseband-equivalent case cannot be directly applied to the wideband case.

2.3 Rake Receiver

In this section, we define the conventional Rake receiver [75, p. 842] and examine its error performance. We concentrate on the wideband case; thus, all quantities

	one path Doppler lag, $\theta' \neq 0$	one path scale lag $a' \neq 1$
$H(\theta, \tau)$	$\boldsymbol{\delta(\theta - \theta')\delta(\tau - \tau')}$	$\frac{\sqrt{a'}}{\lvert 1-a' \rvert} e^{-j2\pi\theta \frac{\tau' - a'\tau}{1-a'}}$
$\mathcal{L}(a, \tau)$	$\begin{cases} \frac{\lvert\theta'\rvert}{\sqrt{a}(1-a)^2} e^{j2\pi\theta' \frac{\tau - a\tau'}{1-a}}, & a \neq 1 \\ 0, & a = 1 \end{cases}$	$\boldsymbol{\delta(a - a')\delta(\tau - \tau')}$
$h(t, \tau)$	$\delta(\tau - \tau')e^{j2\pi t\theta'}$	$\sqrt{a'}\delta((1-a')t + a'\tau - \tau')$

Table 2.2: Time-frequency and time-scale characterization functions for the one path Doppler-lag and one path scale-lag channels. [81, p. 51]

are real valued. To recover the k^{th} bit, the Rake receiver generates a set of sufficient statistics $\{r_n^{(k)}\}$ by projecting the received signal $r(t)$ onto a set of functions $\{x_n^{(k)}(t)\}_{n=0}^{N}$, which are time-shifted versions of the DSSS waveform:

$$x_n^{(k)}(t) := x(t - nt_o - kT_s). \tag{2.34}$$

The *translation-spacing parameter* t_o is specified to be $t_o := \frac{k_t}{f_o}$, where the relation parameter k_t is a design choice based on the rule-of-thumb [75] that a DSSS waveform can resolve multipath at delays spaced on the order of $\frac{1}{2W}$ seconds apart. Recall that f_o is the peak frequency of the chip-pulse waveform. We provide more detail on the choice of k_t in Section 3.1. The number of waveforms $N + 1 \geq \lceil \tau_{\max} W \rceil$ is chosen so the Rake receiver extracts a significant portion of the received signal energy. The

Rake projection coefficients are

$$
\begin{aligned}
r_n^{(k)} &= \langle x_n^{(k)}(t), r(t)\rangle, && (2.35)\\
&= \sum_{l=0}^{N_b-1} b_l \underbrace{\left\langle x_n^{(k)}(t), \int_0^{\tau_{\max}} h(t,\tau)x(t-lT_s-\tau)d\tau \right\rangle}_{\approx 0,\text{ for } l\neq k \text{ since } \tau_{\max}\ll T_s} + \underbrace{\langle x_n^{(k)}(t), w(t)\rangle}_{w_n^{(k)}}, && (2.36)\\
&\approx b_k \underbrace{\left\langle x_n^{(k)}(t), \int_0^{\tau_{\max}} h(t,\tau)x(t-kT_s-\tau)d\tau \right\rangle}_{h_n^{(k)}} + w_n^{(k)}, && (2.37)\\
&= b_k h_n^{(k)} + w_n^{(k)}. && (2.38)
\end{aligned}
$$

We call $\{h_n^{(k)}\}$ the *channel coefficients* and $\{w_n^{(k)}\}$ the *noise coefficients*. To simplify the notation, we vectorize the $N+1$ Rake projection coefficients to obtain

$$\boldsymbol{r}_k = b_k \boldsymbol{h}_k + \boldsymbol{w}_k \tag{2.39}$$

where $\boldsymbol{r}_k := [r_0^{(k)}, r_1^{(k)}, \ldots, r_N^{(k)}]^T$; $\boldsymbol{h}_k$ and $\boldsymbol{w}_k$ are defined likewise.

The noise vector is Gaussian distributed with zero mean; hence, the optimal bit error rate (BER) minimizing coherent receiver is the whitened matched filter [75, p. 603], which assumes knowledge of the channel coefficients $\boldsymbol{h}_k$ and noise correlation matrix $\boldsymbol{R_w} := \mathrm{E}[\boldsymbol{w}_k \boldsymbol{w}_k^H] = \sigma_w^2 \boldsymbol{R_x}$, where

$$\boldsymbol{R_x} = \begin{bmatrix} \mathrm{E}[\langle x_0^{(k)}(t), x_0^{(k)}(t)\rangle] & \cdots & \mathrm{E}[\langle x_0^{(k)}(t), x_N^{(k)}(t)\rangle] \\ \vdots & \ddots & \vdots \\ \mathrm{E}[\langle x_N^{(k)}(t), x_0^{(k)}(t)\rangle] & \cdots & \mathrm{E}[\langle x_N^{(k)}(t), x_N^{(k)}(t)\rangle] \end{bmatrix} \tag{2.40}$$

is the autocorrelation between the Rake basis functions. The expectation is taken over the random spreading code. For practical systems, the receiver must estimate the channel coefficients $\boldsymbol{h}_k$.

The decision statistic $\hat{b}_k$ is

$$\hat{b}_k = \boldsymbol{f}_k^H (\boldsymbol{R}_{\boldsymbol{x}}^{-1/2})^H \boldsymbol{r}_k, \tag{2.41}$$

$$= b_k \|\boldsymbol{f}_k\|^2 + \boldsymbol{f}_k^T (\boldsymbol{R}_{\boldsymbol{x}}^{-1/2})^H \boldsymbol{w}_k. \tag{2.42}$$

where $(\boldsymbol{R}_{\boldsymbol{x}}^{-1/2})^H$ is the whitening matrix and $\boldsymbol{f}_k = (\boldsymbol{R}_{\boldsymbol{x}}^{-1/2})^H \boldsymbol{h}_k$ is the combining coefficient vector. The matrix $\boldsymbol{R}_{\boldsymbol{x}}^{1/2}$ is, e.g., the Cholesky decomposition of the matrix $\boldsymbol{R}_{\boldsymbol{x}}$.

Conditional Bit Error Rate

The final bit decision is made by observing the sign of the sufficient statistic $\text{sign}\{\hat{b}_k\}$. The BER, given the combining coefficients $\boldsymbol{f}_k$, is easily shown to be

$$P_{e|\boldsymbol{f}_k} = Q\left(\sqrt{\frac{\|\boldsymbol{f}_k\|^2 E_b}{\sigma_w^2}}\right). \tag{2.43}$$

where

$$Q(x) = \int_x^\infty \frac{1}{\sqrt{2\pi}} e^{-\frac{z^2}{2}} dz \tag{2.44}$$

is the tail probability of the unit normal random variable. Note that the error probability is conditioned on the norm of the combining vector $\boldsymbol{f}_k$, which depends on the time-varying channel.

2.3.1 Fading and Diversity

In general, diversity reception techniques refer to the receiver "observing" the information symbol through more than one fading "channel" [74] [95] in order to enhance the link reliability. Depending on transmitter-receiver configuration, copies of the information symbol may arrive at the receiver through a combination of different

delays, frequencies, times, dilations, polarizations, and antennas. Relative motion between the transmitter and receiver causes the amplitudes of the various channels to fluctuate. The basic idea is that when one "channel" is faded, another may provide enough information for correct bit decision.

Fading is often regarded as a "bad" phenomenon; however, under certain contexts, fading can actually enhance performance, e.g., when multiuser systems can schedule transmission times to opportunistically leverage good channel states [95]. In order to isolate the effect of exploiting scale-lag diversity, we assume a simple point-to-point single-user system with a single transmit and a single receive antenna, future work would employ multiple transmit antennas [1] [97].

The conventional Rake receiver (2.42) exploits lag diversity, where fingers of the Rake provide different observations of the transmitted bit. The n^{th} "bit observation" (corresponding to the n^{th} Rake finger) is multiplied by the n^{th} channel coefficient $h_n^{(k)}$. The time-varying channel causes the channel coefficients $\{h_n^{(k)}\}$ to change from bit to bit. As described above, it is hoped that if some of the channel coefficients are faded, then others will provide enough energy for a correct decision. In the following, we compute the expectation of the BER and quantitatively define the "effective diversity" exploited by the Rake receiver.

In the following, we assume that the receiver is demodulating the 0^{th} bit and hence drop the bit index k; the following results would hold for any other bit in a bit-by-bit detector. To begin, we define the correlation matrix of the whitened matched-filter combining coefficients $\boldsymbol{f}$ to be $\boldsymbol{\Sigma} := \mathrm{E}[\boldsymbol{f}\boldsymbol{f}^T] = \boldsymbol{R}_{\boldsymbol{x}}^{-H/2}\boldsymbol{R}_{\boldsymbol{h}}\boldsymbol{R}_{\boldsymbol{x}}^{-1/2}$ where $\boldsymbol{R}_{\boldsymbol{h}} := \mathrm{E}[\boldsymbol{h}\boldsymbol{h}^H]$. Suppose that the channel coefficients $\boldsymbol{h}$ are distributed as a zero-mean

real-valued jointly-Gaussian random vector. This model is a obtained from a central limit theorem argument where multiple non line-of-sight reflections are superimposed at the receive antenna. It follows that $\boldsymbol{f} \sim \mathcal{N}(\mathbf{0}, \boldsymbol{\Sigma})$. Note that diversity results for any other distribution on $\boldsymbol{f}$ could likewise be obtained by plugging the distribution into the following analysis.

To find the unconditional probability of error, we take the expectation of (2.43) with respect to the coefficients $\boldsymbol{f}$. To this end, we use the preferred form of the Q-function $Q(x) = \frac{1}{\pi}\int_0^{\pi/2} \exp\left(-\frac{x^2}{2\sin^2\theta}\right) d\theta$ [89] and write

$$
\begin{aligned}
P_e &= \mathrm{E}_{\boldsymbol{f}}\left[Q\left(\sqrt{\frac{\|\boldsymbol{f}\|^2 E_b}{\sigma_w^2}}\right)\right] && (2.45)\\
&= \frac{1}{\pi}\,\mathrm{E}_{\boldsymbol{f}} \int_0^{\pi/2} \exp\left(-\frac{\|\boldsymbol{f}\|^2 E_b}{2\sigma_w^2 \sin^2\theta}\right) d\theta && (2.46)\\
&= \frac{1}{\pi}\int_0^{\pi/2}\int_{\mathbb{R}^N} \exp\left(-\frac{\|\boldsymbol{f}\|^2 E_b}{2\sigma_w^2 \sin^2\theta}\right) \frac{1}{(2\pi)^{N/2}(\det\boldsymbol{\Sigma})^{1/2}} \\
&\quad \exp\left(-\frac{1}{2}\boldsymbol{f}^T\boldsymbol{\Sigma}^{-1}\boldsymbol{f}\right) d\boldsymbol{f} d\theta && (2.47)\\
&= \frac{1}{\pi}\int_0^{\pi/2}\int_{\mathbb{R}^N} \frac{1}{(2\pi)^{N/2}(\det\boldsymbol{\Sigma})^{1/2}} \exp\left(-\frac{1}{2}\boldsymbol{f}^T\boldsymbol{\Omega}^{-1}\boldsymbol{f}\right) d\boldsymbol{f}_k d\theta && (2.48)
\end{aligned}
$$

where $\boldsymbol{\Omega}^{-1} := \boldsymbol{\Sigma}^{-1} + \frac{E_b}{\sigma_w^2 \sin^2\theta}\boldsymbol{I}$. If we multiply the numerator and denominator of the integrand in (2.48) by $(2\pi)^{N/2}(\det\boldsymbol{\Omega})^{1/2}$, then the integration over the combining coefficients reduces to

$$
\begin{aligned}
P_e &= \frac{1}{\pi}\int_0^{\pi/2} \frac{1}{(\det(\boldsymbol{\Omega}^{-1}\boldsymbol{\Sigma}))^{1/2}} d\theta && (2.49)\\
&= \frac{1}{\pi}\int_0^{\pi/2} \prod_{l=0}^{N-1}\left(1 + \frac{E_b\lambda_l}{\sigma_w^2\sin^2\theta}\right)^{-1/2} d\theta && (2.50)
\end{aligned}
$$

where $\{\lambda_l\}_{l=0}^{N-1}$ are the eigenvalues of the combining coefficient autocorrelation matrix $\boldsymbol{\Sigma}$. Finally, we note that the integrand attains a maximum when $\theta = \pi/2$; hence,

(2.50) can be upper-bounded by

$$P_e \leq \frac{1}{2} \prod_{l=0}^{N-1} \left(1 + \frac{E_b \lambda_l}{\sigma_w^2}\right)^{-1/2}, \tag{2.51}$$

which is the Chernoff bound on the average error probability.

Throughout this dissertation, the signal to noise ratio (SNR) is defined as $\mathsf{SNR} = \frac{E_b}{\sigma_w^2}$, which is the *transmitted* SNR. We use the transmitted SNR in order to appropriately compare the performances of different Rake receiver structures.

Effective Diversity

The upper bound (2.51) can be mildly loosened to provide insight into the shape of the BER curve. For a nominal value of SNR $\frac{E_b}{\sigma_w^2}$, we order and partition the eigenvalues:

$$\{\lambda_i\}_{i=0}^{N-1} = \{\lambda_j^{\mathsf{big}}\}_{j=0}^{B-1} \bigcup \{\lambda_j^{\mathsf{small}}\}_{j=0}^{N-B-1} \tag{2.52}$$

where $\lambda_j^{\mathsf{big}} > \frac{\sigma_w^2}{E_b}$ and $\lambda_j^{\mathsf{small}} \leq \frac{\sigma_w^2}{E_b}$. The small eigenvalues $\{\lambda_j^{\mathsf{small}}\}$ can be ignored such that the upper bound becomes

$$\log(P_e) \leq -\frac{B}{2} \log\left(\frac{E_b}{\sigma_w^2}\right) - C \tag{2.53}$$

where $C := -\log\frac{1}{2} + \frac{1}{2}\log\left(\prod_{j=0}^{B-1} 2\lambda_j^{\mathsf{big}}\right)$.

We denote the negative BER-slope $\frac{B}{2}$ as the *effective diversity level* extracted by the receiver at the nominal value of SNR $\frac{E_b}{\sigma_w^2}$. Note that, as the nominal SNR increases, the effective diversity level approaches the traditionally defined asymptotic

diversity level, which for our Gaussian-distributed system equals the number of non-zero eigenvalues divided by two. The division by two is an artifact of assuming the channel coefficients are real-Gaussian distributed.[4]

Numerical Example

To gain insight into how the bit error rate (BER) depends on eigenvalue profile, we plot BER performance versus SNR $\frac{E_b}{\sigma_w^2}$ for systems with uniformly-valued eigenvalues and with exponentially decaying eigenvalues, e.g., $\{0, -3, -6, \ldots, -3(N-1)\}$ dB. For both systems, the eigenvalues are such that they sum to unity. The derivation of BER for Gaussian-distributed channel coefficients is described in the previous section.

Figure 2.4 shows the sets of eigenvalues, which are normalized to sum to unity for each set. The corresponding average bit error rate (BER) versus signal to noise ratio (SNR) is shown in Fig. 2.5. Also shown in Fig. 2.5 is the BER performance (Fixed) of a 1-channel system where the gain is fixed (i.e. not randomly fading). In both plots, the solid lines indicate systems with uniformly-valued eigenvalues and the dashed lines indicate performance of systems with exponentially decaying eigenvalues. Note that increasing the number of observations of the transmitted bit reduces the bit error rate, even though extra observations come with additive noise terms. The two eigenvalue distributions eventually have the same asymptotic BER slope, but the uniformly-valued eigenvalue system achieves better performance for the same number of observations. We implicitly assume that the channel gains are known by the receiver; in practical systems, however, the channel gains must be estimated.

[4]Complex circular-Gaussian distributed channel coefficients do not lead to a division by two.

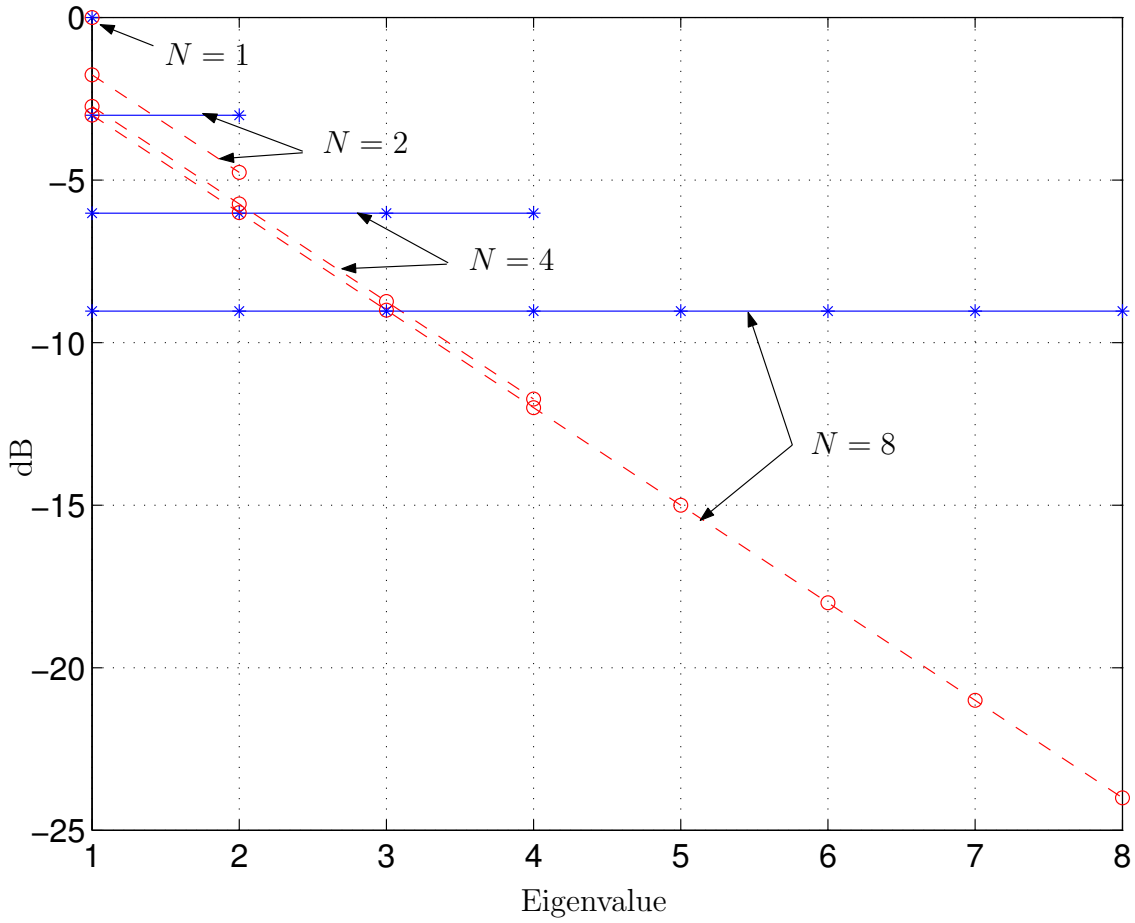

Figure 2.4: Eigenvalue profile for $N = 1, 2, 4, 8$ channels. The eigenvalues are normalized to unity for each profile.

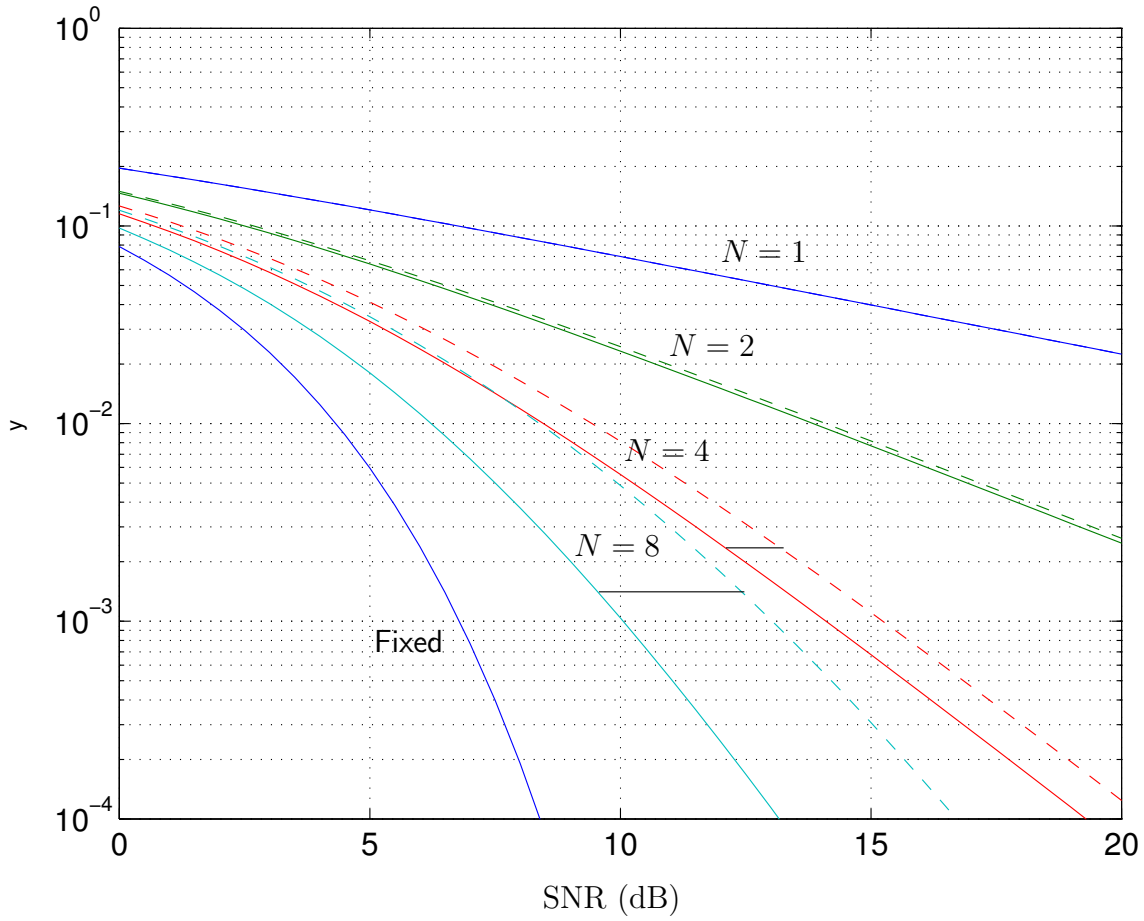

Figure 2.5: Average BER versus SNR for coherent binary phase-shift keying (BPSK) in Gaussian noise. Dashed lines indicate BER performance of uniformly-valued eigenvalues and solid lines indicate BER performance of exponentially-decaying eigenvalues.

2.4 Previous Work

In this section, we first discuss two types of wideband communication systems for which our work is apropos: electromagnetic ultra-wideband (UWB) communications and underwater wideband acoustic communications (UWAC). Each system has unique challenges and opportunities as outlined below. We then review two papers: [85] and [5], which provided the main impetus for the current work.

2.4.1 Wideband Systems

Electromagnetic Ultra-Wideband

Beginning with preliminary work by Scholtz [87] and Win and Scholtz [101], electromagnetic radio frequency UWB radio has become a major research area today. UWB radio communications spans applications from military covert communications to commercial indoor wireless links. A large push for commercial applications came after the Federal Communications Commission (FCC) amended its Part 15 rules in February 2002 to allow unlicensed UWB spectral emissions for wireless digital communications [34] [19] [20]. The FCC mandated that spectral energy radiated by handheld UWB devices must be lower than the specified spectral mask shown in Fig. 2.6. The large notch below five Gigahertz prevents UWB devices from interfering with vital services such as the global positioning system (GPS).

There are currently two design philosophies proposed for UWB standardization (see [96] [105] for a discussion). The first proposal is impulse radio, which is a form of extreme spread spectrum where chip pulses are nanosecond in duration and are transmitted directly at baseband, i.e., are not modulated to a carrier frequency. Impulse

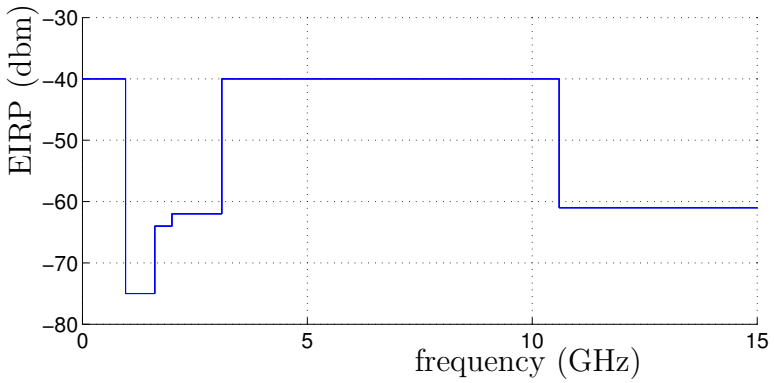

Figure 2.6: FCC spectral mask for handheld UWB devices.

radio is intended for longer-range lower-rate communication systems. For reference, a typical impulse-radio UWB system we consider has mobile velocity of 10 km/hr, data rate of 1 Mbps, and bandwidth of 10 GHz. The second proposal is to transmit via an OFDM-like multiband waveform where each carrier occupies greater than 500 MHz. The OFDM proposal is intended for shorter-range higher-rate communication systems. As mentioned above, mobility implies that each carrier of a UWB system employing OFDM will experience a carrier-frequency-dependent amount of Doppler spreading [83] [12]. Carriers at lower frequencies will experience less spreading than carriers at higher frequencies. A good overview of the state of the art in UWB communications can be found in [105]. The focus of this dissertation is on the impulse-radio method, since we consider higher-mobility systems; future work would apply the wideband channel model to modulated UWB systems.

An interesting dynamic UWB channel model is found in [47, 48] where the authors propose a spatially-varying baseband impulse response. The mobile unit is placed in a

grid of virtual sources and the time delay from each source to the mobile is calculated as the mobile moves in space. The source locations are chosen to match an intended environment. For each virtual source, a cluster of reflections is randomly generated to model a typical channel response. While this model yields time-varying delay spreads that visually match measurements, it is a cumbersome model for analytical purposes. In addition, there is no discussion of time dilations caused by motion in the channel, though dilations are implicitly modeled. The model is extended in [97] to investigate the performance of a multiple antenna system.

In the radio frequency (RF) ultra-wideband (UWB) literature, many papers characterize the statistics of the delay spread of UWB systems [3, 14, 31, 50, 88, 93, 100, 108], but do not consider time-varying channel geometries. The IEEE 802.15.3a standardization group has developed a channel model [31] based on the Valenzuela-Saleh model [84]. Basically, reflections are modelled as arriving in clusters. The clusters arrive according to a Poisson process, and the paths within each cluster arrive with a Poisson process. Each cluster has exponential power profile and the fading is log-normal (rather than Rayleigh). An outdoor forest finite-difference time-domain (FDTD) ray tracing simulation study and field measurement trial is undertaken in [86].

Using the static channel model, dozens of papers study the performance of UWB impulse radio receivers, e.g., [8, 15, 18, 22, 29, 30, 32, 38, 39, 49, 51, 54, 56, 69, 70, 71, 73, 76, 79, 77, 78, 82, 99, 100, 101, 107, 110]. One reason for the adoption of the static channel model is that the focus of current UWB research is on indoor environments [100] where mobility is less of an issue. However, advances in signal

processing hardware and algorithms are allowing the design of radio frequency (RF) communications systems with ever increasing bandwidths and mobility [36] [109]. If UWB devices follow the trend of other wireless systems, we can expect mobility to become more of an issue in the future.

Timing jitter and acquisition are also a major research thrust in the UWB community, e.g., [10, 13, 33, 37, 57, 61, 67, 94, 104, 109]. We recognize the unique challenges of timing acquisition in UWB systems; however, to simplify the current exposition we assume the receiver has perfect knowledge of chip and symbol time.

Throughout this thesis, we will consider inter-symbol interference (ISI) to be negligible, since we assume the symbol duration to be much greater than the delay spread. An important question for future research is the design of optimal diversity-exploiting receivers capable of mitigating ISI for high-rate systems such that ISI is non-negligible. The paper by Klein et al. [46] assumes non-negligible ISI and the Rake receiver is modified to one that considers both ISI and narrowband interference via a minimum mean squared error (MMSE) criterion. The finite set of Rake fingers are allowed to float, reminiscent of selection combining, and finger weights are calculated according to a mean squared error (MSE) criterion. Thus, the optimization problem becomes one of minimizing the MSE by jointly placing the rake fingers at optimal delays and calculating optimal finger weights. Given a finger placement, the cost is quadratic in the finger weights; however, the cost has many local minima and maxima over finger placement. The analysis assumes complete knowledge of channel state information (CSI) and only applies to short-coded pulse-repetition systems, since the MSE is calculated at the symbol level.

While an enormous amount of research is being performed on radio frequency UWB radio, an equally challenging communications environment is the underwater acoustic wideband communications channel.

Underwater Wideband Acoustic

Underwater wideband acoustic communication (UWAC) systems benefit from scale-lag diversity research since signal dilations in the acoustic domain are much greater due to the low speed of wave propagation. A good overview of the underwater acoustic communications channel is found in [45]. In [25, 26, 28], the authors take into account signal dilation due to platform motion and design receivers capable of mitigating this effect, but do not consider the implication of leveraging scale diversity to enhance receiver performance. Our research will aid in the design of robust acoustic systems for difficult time-varying multipath environments. For reference, a typical UWAC system considered in this dissertation has mobile velocity of 5 km/hr, data rate of 1 kbps, and bandwidth of 36 kHz.

2.4.2 Narrowband and Wideband Canonical Models

In this section, we discuss two papers: [85] and [5], which are the main impetus for the present work. Sayeed and Aazhang [85] make two fundamental contributions:

1. The derivation of a narrowband baseband-equivalent canonical model for parsimonious representation of the received signal.

2. The development and performance analysis of a Doppler-lag Rake receiver, which exploits Doppler-lag channel diversity.

The first contribution is extended to the wideband case by Balan et al. [5]. Although Balan et al. suggest using a scale-lag Rake receiver for the wideband case, it is not developed.

The main thrust of Sayeed and Aazhang [85] is to improve the BER performance of a Rake receiver for a direct sequence spread spectrum (DSSS) signal in a single-bit, single-antenna, single-user, doubly-selective fading channel. Simply put, they propose an enhanced receiver, called the Doppler-lag Rake, to collect energy from Doppler-frequency-shifted signals as well as from non-shifted signals. Before [85], it was generally assumed that Doppler effects were insignificant over the duration of a symbol. However, [85] shows that considering even small Doppler effects can lead to big performance gains. In fact, [85] suggests lengthening the symbol duration to collect ever more Doppler energy thereby improving performance. However, it is clear that there is a trade-off between performance and transmission rate. This is addressed in [9] by allowing successive symbols to overlap in time. Works that consider transmission schemes to exploit Doppler diversity are [11, 53, 58, 59, 60, 80, 106]. In this dissertation, we focus on receive diversity as a first step in exploiting the dynamics of the wideband channel.

Part of the research in this dissertation involves taking some ideas developed by Sayeed and Aazhang for the narrowband channel and, motivated by the wideband canonical model of Balan et al., applying them to the wideband channel to show that exploiting the small temporal dilations induced by mobility leads to large performance gains.

Narrowband Canonical Model

The analysis in [85] centers on the discovery of a parsimonious time-frequency representation of the narrowband baseband-equivalent time-varying channel, called the narrowband canonical model.[5] Basically, for a channel input with double-sided bandwidth approximately limited to $\tilde{W}$ Hertz, and symbol duration approximately limited to T_s seconds, a Fourier-series analysis can be used to show that the output can be represented by a weighted sum over uniform frequency- and lag-shifted copies of the input. The inter-frequency spacing is $1/T_s$ and the inter-lag spacing is $1/\tilde{W}$.

In particular, consider a single-bit transmission with the narrowband baseband-equivalent DSSS signal (2.1) through a time-varying channel. The canonical model is derived by looking at only the $[0, T_s]$ portion of the narrowband baseband-equivalent channel output, i.e., $\tilde{r}(t)1_{[0,T_s]}$. For $t \in [0, T_s]$, the narrowband canonical model for $\tilde{r}(t)$ (neglecting additive noise) is

$$\tilde{r}(t) = \sum_m \sum_n \tilde{l}_{m,n} \tilde{x}\left(t - \frac{n}{W}\right) e^{j2\pi mt/T_s}, \tag{2.54}$$

where the narrowband canonical model coefficients $\{\tilde{l}_{m,n}\}$ are

$$\tilde{l}_{m,n} = \int_0^{\tau_{\max}} \int_{-f_{\max}}^{f_{\max}} \tilde{H}(\theta, \tau) \operatorname{sinc}(n - W\tau) \operatorname{sinc}(m - T_s\theta) e^{-j\pi(m - T_s\theta)} d\theta d\tau. \tag{2.55}$$

A simple change of variables $\theta' = T_s\theta$, $\tau' = \tilde{W}\tau$ in (2.55) gives the following:

$$\tilde{l}_{m,n} = \frac{1}{\tilde{W}T_s} \int_0^{\tau_{\max}\tilde{W}} \int_{-f_{\max}T_s}^{f_{\max}T_s} \tilde{H}\left(\frac{\theta'}{T_s}, \frac{\tau'}{\tilde{W}}\right) \operatorname{sinc}(n - \tau') \operatorname{sinc}(m - \theta') e^{-j\pi(m-\theta')} d\theta' d\tau'. \tag{2.56}$$

[5] Others have independently suggested and used similar so-called basis expansion models (BEMs) [35].

Sayeed and Aazhang [85] simplify the sum (2.54) by considering only the model coefficients where the main-lobes of the sinc functions in (2.56) overlap with the kernel $\tilde{H}(\theta, \tau)$; thus, [85] includes only the following terms: $m = -M, \ldots, M$ where $M = \lceil f_{\max} T_s \rceil$; and $n = 0, 1, \ldots, N$ where $N = \lceil \tilde{W} \tau_{\max} \rceil$,

$$\tilde{r}(t) \approx \sum_{m=-M}^{M} \sum_{n=0}^{N} \tilde{l}_{m,n} x \left(t - \frac{n}{\tilde{W}} \right) e^{j2\pi m t / T_s}. \tag{2.57}$$

We make a few observations about the canonical model:

- It is a parsimonious representation of the channel output, i.e., the number of model coefficients is reduced from a sampling of approximately $\tilde{W} T_s$ coefficients to approximately $(2M + 1)(N + 1)$ coefficients. The values of M and N are chosen as the largest values of m and n, respectively, such that the main lobe of the sinc function overlaps with the support of the narrowband baseband-equivalent spreading function $\tilde{H} \left(\frac{\theta'}{T_s}, \frac{\tau'}{\tilde{W}} \right)$ in (2.56).

- If the DSSS waveforms $\{ \tilde{x} \left(t - \frac{n}{\tilde{W}} \right) e^{j2\pi t / T_s} \}$ are orthogonal, then the representation suggests using a Rake receiver matched to these waveforms to recover the energy in the model coefficients. In this case, the model coefficients $\{ \tilde{l}_{m,n} \}$ can be used independently from the specifics of the waveform $\tilde{x}(t)$ to predict performance. If the transmit waveforms are not orthogonal, then effects of the waveform cross-correlations must be included in the analysis. The extension to the wideband case, including the effects of non-orthogonal transmit waveforms, is discussed in Section 3.2.

- The number $(2M + 1)(N + 1)$ can be thought of as the degrees of freedom characterizing the channel.

Sayeed and Aazhang [85] showed that the frequency- and lag-shifted copies of the DSSS signal $\{\tilde{x}\left(t-\frac{n}{\tilde{W}}\right)e^{j2\pi t/T_s}\}$ are approximately orthogonal. The receiver then projects the received signal onto this basis to generate a set of statistics; however, the statistics are not necessarily sufficient. The sufficiency of the statistics was not fully investigated by [85]. Figure 7 in [85] shows performance curves for the coherent Doppler-lag Rake compared to the conventional lag-only Rake (discussed in Section 2.3). One notes the large performance gain for small values of Doppler spread, i.e., for small values of $f_{max}T_s$.

In [85] it is assumed, from central-limit theorem arguments, that the underlying channel kernel $\tilde{H}(\theta,\tau)$ is a zero-mean two-dimensional uncorrelated Gaussian process, which implies that the model coefficients $\{\tilde{l}_{m,n}\}$ are zero-mean Gaussian random variables. This leads to the second key contribution of [85]: the assumption that the model coefficients $\{\tilde{l}_{m,n}\}$ are uncorrelated and thus the canonical model (2.57) is a *Karhunen-Loeve-like* expansion of the narrowband baseband-equivalent channel. However, for practical values of Doppler spread $f_{\max}$ and symbol duration T_s, the channel coefficients will be correlated. Sayeed, in a recent email correspondence, agreed that it would be interesting to investigate system performance with correlated channel coefficients.

Wideband Canonical Model

Balan et al. [5], inspired by the narrowband frequency-lag canonical model of [85], derived a powerful time-scale canonical model for the wideband transformation in (2.29). A very similar canonical model for the wideband channel was developed

independently in [41, 42]. The wideband channel output is written as a weighted sum of delayed and dilated versions of the input:

$$r(t) = \sum_m \sum_n l_{m,n} \frac{1}{a_o^{m/2}} s\left(\frac{t - n t_o a_o^m}{a_o^m}\right), \tag{2.58}$$

where the wideband canonical coefficients $l_{m,n}$ are given by,

$$l_{m,n} \;=\; \int_0^{\tau_{max}} \int_{a_{min}}^{a_{max}} \mathcal{L}(a,\tau) \mathrm{sinc}\left(n - \frac{\tau}{a t_o}\right) \mathrm{sinc}\left(\frac{\ln(a)}{\ln(a_o)} - m\right) da\, d\tau. \tag{2.59}$$

The canonical representation (2.58) shows that the output of the wideband transformation can be expanded by shift-dilates of the transmitted waveform; hence, in the presence of additive white Gaussian noise (AWGN) at the receiver, a bank of correlators matched to shift-dilates of the transmitted waveform produces a set of (possibly correlated) sufficient statistics for the optimal receiver [75, Ch 5].

The impetus for Balan et al. [5] is Rickard's dissertation [81], which extensively studied the connections between the narrowband and wideband kernels and proposed the wideband canonical model. The wideband canonical model (2.58) looks very similar to the narrowband canonical model (2.54), in that a double-integral transformation is decomposed into a weighted double-sum. The following observations concerning the treatment of the wideband canonical model in [5] can be made:

- The *dilation spacing* parameter a_o and *translation spacing* parameter t_o were not specified.

- A set of orthonormal dilated and shifted waveforms inspires the use of a scale-lag Rake receiver, similar to the principle of a Doppler Rake in the narrowband case. The scale-lag Rake projects the received signal onto the dilated-delayed basis waveforms.

- The possibility of a scale-lag Rake receiver was mentioned by [5], but no details were developed.

- For an orthonormal basis, the coefficients $\{l_{m,n}\}$ are effectively a sampling of the scale-lag plane, as shown in Fig. 2.7. Define the *scale spacing* parameter to be $\gamma_o := a_o - 1$. A Taylors series approximation around $a_o = 1$ gives $a_0^m \approx 1 + m(a_0 - 1) = 1 + m\gamma_o$; hence, a uniform spacing in the scale domain suffices for typical values of dilation (i.e., $a \approx 1$).

- Assuming a statistical model for $\mathcal{L}(a, \tau)$, one could characterize the performance of the scale-lag Rake receiver, and compare it to the Doppler-lag Rake receiver and to the conventional lag-only Rake receiver. This analysis was not performed by [5].

These observations lead to questions regarding the design and performance of a so called scale-lag Rake receiver, which we study in the following chapters.

Approximation

In this section, we make a few reasonable approximations to show the similarity between the narrowband and wideband canonical models.

Note that in practical systems, the scale spread $\gamma_{\max}$ and the scale spacing parameter γ_o are very small; hence, the variable a and the dilation spacing parameter a_o are very near unity. A Taylor series approximation can be used to write

$$\ln(a) \;\approx\; \frac{a-1}{a} \;\approx\; a - 1, \tag{2.60}$$

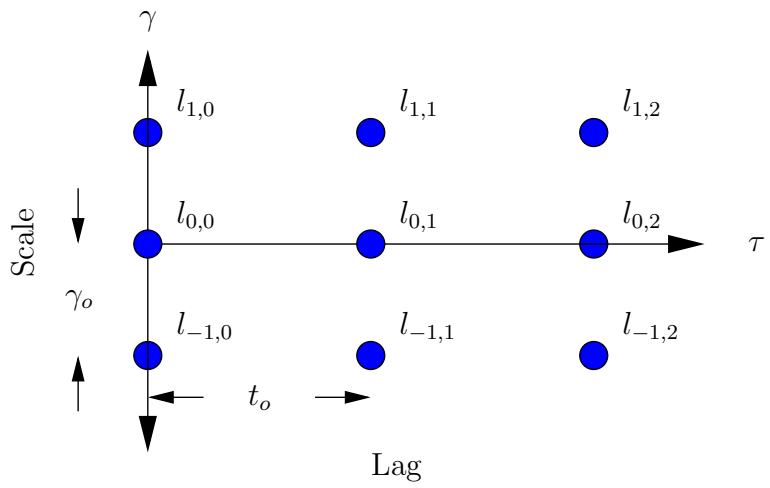

Figure 2.7: Sampling the scale-lag plane.

likewise,

$$\ln(a_o) \;\approx\; \frac{a_o - 1}{a_o} \;\approx\; a_o - 1. \tag{2.61}$$

In (2.59), we make the change of variables: $\gamma = \frac{a-1}{\gamma_o}$, and $\tau' = W\tau$, to write the wideband channel coefficients

$$l_{m,n} \approx \frac{\gamma_o}{W} \int_0^{\tau_{\max} W} \int_{-\frac{\gamma_{\max}}{\gamma_o}}^{\frac{\gamma_{\max}}{\gamma_o}} \mathcal{L}\left(1 + \gamma\gamma_o, \frac{\tau'}{W}\right) \operatorname{sinc}(n - \tau') \operatorname{sinc}(m - \gamma)\, d\gamma d\tau'. \tag{2.62}$$

For ease of reference, we repeat the expression of the narrowband canonical model coefficients:

$$\tilde{l}_{m,n} = \frac{1}{\tilde{W} T_s} \int_0^{\tau_{\max} W} \int_{-f_{\max} T_s}^{f_{\max} T_s} \tilde{H}\left(\frac{\theta'}{T_s}, \frac{\tau'}{\tilde{W}}\right) e^{-j\pi(m - T_s\theta)} \operatorname{sinc}(n - \tau') \operatorname{sinc}(m - \theta') d\theta' d\tau'. \tag{2.63}$$

Using the same arguments as in the narrowband case, we reduce the number of wideband channel coefficients by considering only the channel coefficients where the

main-lobes of the sinc functions in (2.62) overlap with the kernel $\mathcal{L}\left(1+\gamma\gamma_o, \frac{\tau'}{W}\right)$; thus, only the following terms are included: $m = -M, \ldots, M$ where $M = \lceil \frac{\gamma_{\max}}{\gamma_o} \rceil + 1$ and $n = 0, 1, \ldots, N$ where $N = \lceil \tau_{\max} W \rceil + 1$

$$r(t) \approx \sum_{m=-M}^{M} \sum_{n=0}^{N} \frac{l_{m,n}}{a_o^{m/2}} x\left(\frac{t - nT_o a_o^m}{a_o^m}\right). \tag{2.64}$$

Hence, as in the narrowband case, the following observations about the wideband canonical model hold:

- It is a parsimonious representation of the channel output, i.e., the number of channel coefficients is reduced from a sampling of approximately WT_s coefficients to approximately $(2M+1)(N+1)$ coefficients.
- The number $(2M+1)(N+1)$ can be thought of as the degrees of freedom characterizing the wideband channel.

Discussion

Sayeed and Aazhang [85] derived a narrowband canonical model for parsimonious representation of the received signal and, after making statistical assumptions on the narrowband baseband-equivalent kernel, analyzed the performance of a Doppler-lag Rake receiver, which exploits Doppler-lag channel diversity. Motivated by the narrowband canonical model, Balan et al. [5] derive a canonical model for the wideband transformation. Although Balan suggested using a scale-lag Rake receiver for the wideband case, it was not developed. Our main contribution is to develop and study the scale-lag Rake receiver for the wideband channel.

CHAPTER 3

SCALE-LAG RAKE RECEIVER

To begin this chapter, we examine the scale- and lag-resolution properties of the wideband direct-sequence spread-spectrum (DSSS) waveform (c.f. (2.2)). These properties lead to good choices of dilation spacing and translation spacing parameters for a set of dilated-delayed functions used in the scale-lag Rake receiver. We propose a low-complexity scale-lag Rake implementation and conclude with a discussion of the connection of the scale-lag analysis to areas outside the scope of wireless communications.

3.1 Scale-Lag Resolution

The scale-lag resolution properties of a wideband DSSS signal $x(t)$ can be determined by studying the *wideband ambiguity function* $\chi(a,\tau)$ [43], defined as

$$\chi(a,\tau) := \left\langle x(t), \frac{1}{\sqrt{a}} x\left(\frac{t-\tau}{a}\right) \right\rangle \tag{3.1}$$

where $\langle f(t), g(t)\rangle := \int_{-\infty}^{\infty} f(t)g(t)dt$ is the inner product.

We define the *minimum resolvable lag* τ_o to be the smallest $\tau > 0$ such that $\chi(1,\tau) = 0$, and the *minimum resolvable dilation* α_o to be the smallest $a > 1$ such

that $\chi(a,0) = 0$; the *minimum scale resolution* is defined as $\beta_o := \alpha_o - 1$. (A table of variables used in this chapter is shown in Table 3.1.) Below, we show that these resolution quantities are related to the chip-pulse duration T_p—or equivalently the peak frequency f_o—and to the symbol duration T_s. The minimum resolvable lag and the minimum scale resolution will be used as guidelines in the sequel to construct the basis functions for the scale-lag Rake receiver.

An often used rule-of-thumb is that a linear Rake receiver can resolve multipath with inter-arrival lag differences on the order of T_p seconds [75, p. 841]. This is verified by the following proposition.

Proposition 1 *The mean and variance of the inner product* $\langle x(t), x(t-\tau)\rangle = \chi(1,\tau)$ *vanishes if* $\tau \geq T_p$.

Proof: The proof is found in Appendix 3.4. □

It immediately follows from Proposition 1 that the minimum resolvable lag τ_o has an upper bound given by $\tau_o \leq T_p$.

The scale resolution property of a DSSS signal is linked to the time-bandwidth product, as we see next. Let a result in a dilation greater than or equal to one chip-pulse duration T_p, (a dilation by one chip-pulse duration is illustrated by Fig. 3.1) or in other words, let a satisfy the relation

$$aT_s - T_s \;\; \geq \;\; T_p \;\; \Leftrightarrow \;\; a \geq 1 + \frac{T_p}{T_s}. \tag{3.2}$$

Now consider the following proposition, which gives a rule-of-thumb for the minimum resolvable dilation α_o.

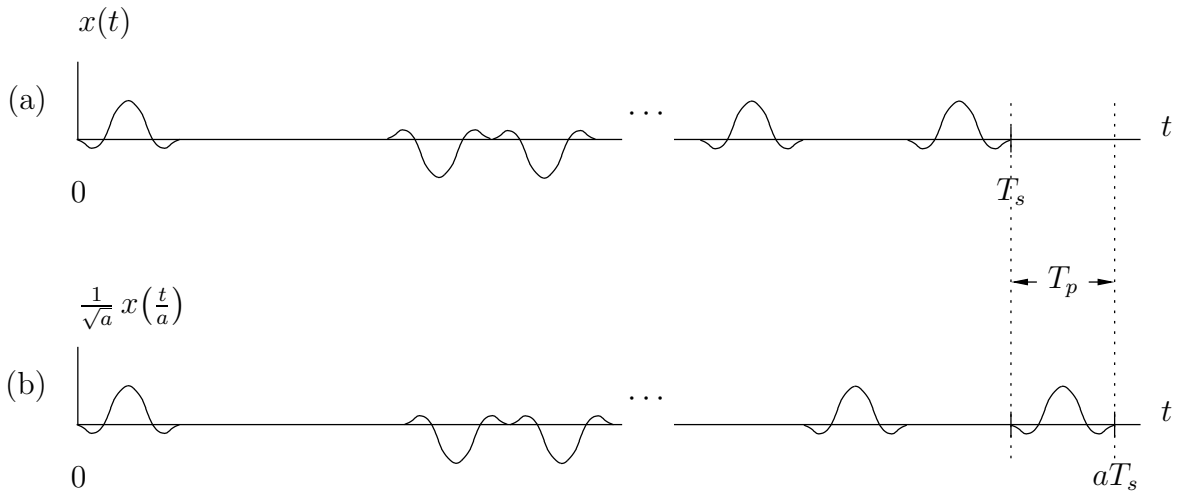

Figure 3.1: (a) Waveform $x(t)$. (b) Waveform $x(t)$ dilated by a.

Proposition 2 *The mean and variance of the inner product* $\left\langle x(t), \frac{1}{\sqrt{a}} x\left(\frac{t}{a}\right) \right\rangle = \chi(a, 0)$ *evaluated at* $a \geq 1 + \frac{T_p}{T_s}$ *vanishes if and only if the chip pulse* $p(t)$ *has zero DC component.*

Proof: The proof is found in Appendix 3.4. □

From Proposition 2, it follows that the minimum resolvable dilation α_o has an upper bound given by $\alpha_o \leq 1 + \frac{T_p}{T_s}$. Equivalently, the *minimum scale resolution* $\beta_o := \alpha_o - 1$ is upper bounded by $\beta_o \leq \frac{T_p}{T_s}$. Since the chip-pulse duration T_p and the peak frequency f_o are inversely proportional, we can say that the scale resolution β_o is on the order of $(T_s f_o)^{-1}$—the inverse of the time-bandwidth product.

The following example with the chip pulse $p(t)$ assigned to be a second-derivative Gaussian waveform illustrates the scale and lag resolution properties of a DSSS signal. The second-derivative Gaussian chip pulse is often used in the UWB literature [21,

91, 101, 111] as a test pulse and is defined as

$$p(t) = \frac{\sqrt{f_o}\sqrt[4]{32\pi}}{\sqrt{3}}\left[1-2(\pi f_o t)^2\right]e^{-(\pi f_o t)^2}, \tag{3.3}$$

with Fourier transform

$$P(f) = \frac{\sqrt{f_o}\sqrt[4]{32\pi}}{\sqrt{3}}\frac{2}{\sqrt{\pi f_o^2}}\left(\frac{f}{f_o}\right)^2 e^{-\frac{f^2}{f_o^2}}. \tag{3.4}$$

Time and frequency plots of the second-derivative Gaussian are shown in Fig. 3.2. From Fig. 3.2(a), we argue that the duration of the chip pulse is roughly $T_p = \frac{2}{f_o}$ seconds.[6] From Fig. 3.2(b), we see that the chip pulse (3.3) has zero DC component[7] and that the peak frequency is indeed at f_o Hertz.

It is shown in Appendix 3.4 that the wideband ambiguity function can be approximated in the mean-square sense as

$$\begin{aligned}\chi(a,\tau) &\approx \bar{\chi}(a,\tau),\\ &:= \int_0^1 \chi_p(1,\tau+(a-1)zT_s)dz\end{aligned} \tag{3.5}$$

where

$$\chi_p(a,\tau) := \left\langle p(t), \frac{1}{\sqrt{a}}p\left(\frac{t-\tau}{a}\right)\right\rangle \tag{3.6}$$

is the wideband ambiguity function of the chip pulse $p(t)$. The approximation is tight when the number of chip pulses N_p is large and the dilation a is near unity, which is the regime we are interested in studying. The chip-pulse ambiguity function for (3.3)

[6]Some authors [21, 111] set the chip-pulse duration to be $T_p := \frac{7}{\pi f_o\sqrt{2}} = \frac{1.58}{f_o}$. We round up to $T_p = \frac{2}{f_o}$.

[7]We wish to point out that other zero-DC component signals may be used, such as the modified duobinary pulse [75, p. 563].

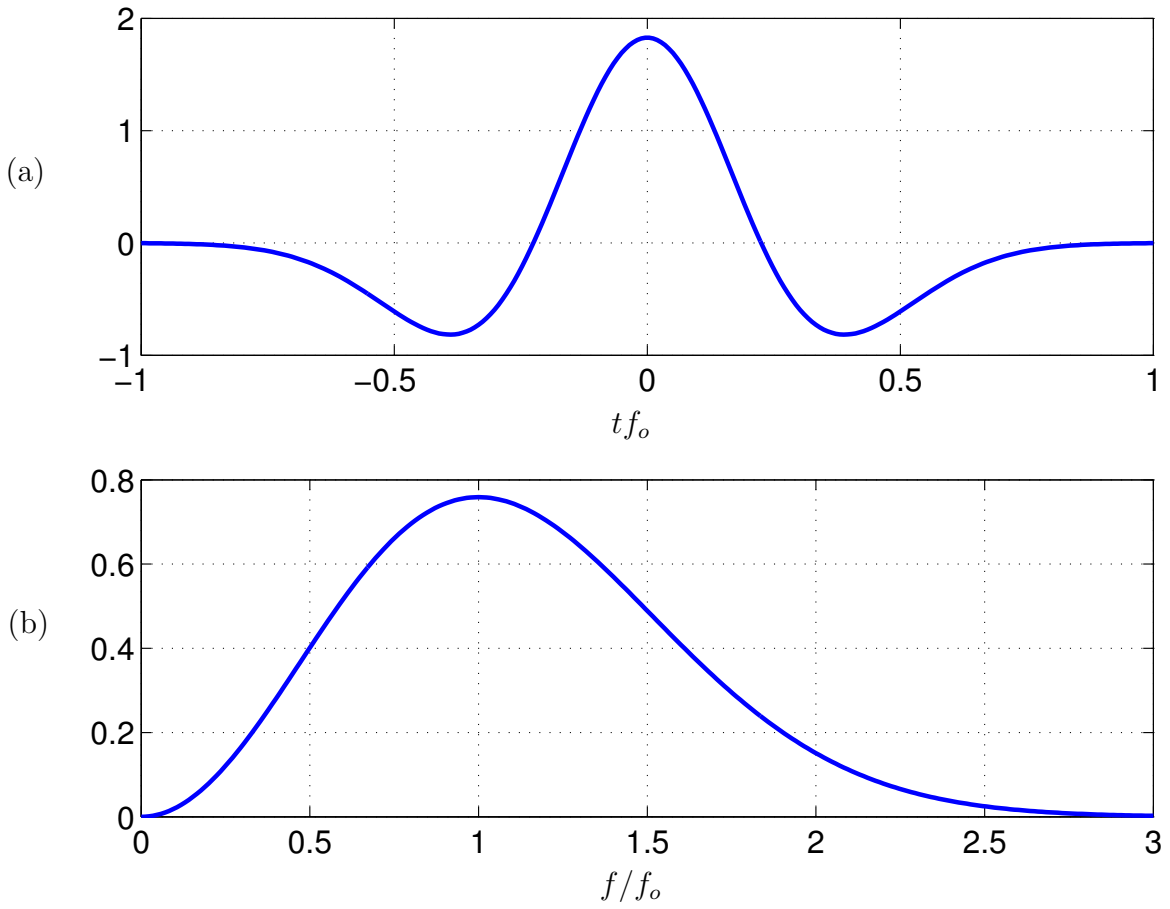

Figure 3.2: Plot of (a) $p(t)$ (time domain) and (b) $P(f)$ (frequency domain) for the second-derivative Gaussian chip pulse, a.k.a. Mexican hat wavelet, defined in (3.3).

is shown in Appendix 3.5 to be

$$\begin{aligned}\chi_p(a,\tau) &= f(a)\left(4\pi^4 f_o^4\tau^4 - 12\pi^2 f_o^2\tau^2(1+a^2) + 3(1+a^2)^2\right) \\ &\quad \exp\left(-\frac{\pi^2 f_o^2\tau^2}{1+a^2}\right), \end{aligned} \tag{3.7}$$

where $f(a) = \frac{4}{3}\sqrt{\frac{2a^5}{(1+a^2)^9}}$. Plugging (3.34) into (3.5), we have an approximation for the wideband ambiguity function (3.1), which we plot in Fig. 3.3. (Note that the approximation $\bar{\chi}(a,\tau)$ is not directly a function of the chip-pulse spacing T_o.) To see the tightness of the approximation, Fig. 3.4 shows for comparison the deterministic wideband ambiguity function $\chi(a,\tau)$ of a typical length-128 i.i.d. random binary chip sequence $x(t)$ composed of second-derivative Gaussian chip pulses. The chip-pulse spacing parameter T_o is chosen to be $T_o = T_p$ such that the chip-pulses are essentially non-overlapping.

Let us now find the minimum resolvable dilation α_o and minimum resolvable lag τ_o by specifically examining the $a = 1$ and $\tau = 0$ cross-sections of $\bar{\chi}(a,\tau)$. These are plotted in Fig. 3.5(a) and (b), respectively.

From Fig. 3.5(a), it is clear that the minimum resolvable dilation is $\alpha_o = 1 + \frac{0.55}{T_s f_o}$. Equivalently, the minimum scale resolution is $\beta_o = \frac{0.55}{T_s f_o}$. Note also that $\bar{\chi}(a,0)$ approaches zero at $a = 1 + \frac{1}{T_s f_o}$ and vanishes at $a = 1 + \frac{2}{T_s f_o} = 1 + \frac{T_p}{T_s}$ as predicted by Proposition 2.

From Fig. 3.5(b), we see that the minimum resolvable lag is $\tau_o = \frac{0.236}{f_o}$. Also note that another zero crossing occurs at $\tau = \frac{0.744}{f_o}$, and that $\bar{\chi}(1,\tau)$ approaches zero at $\tau = \frac{1}{f_o}$. Proposition 1 is verified since $\chi(1,\tau)$ vanishes at $\tau = T_p = \frac{2}{f_o}$.

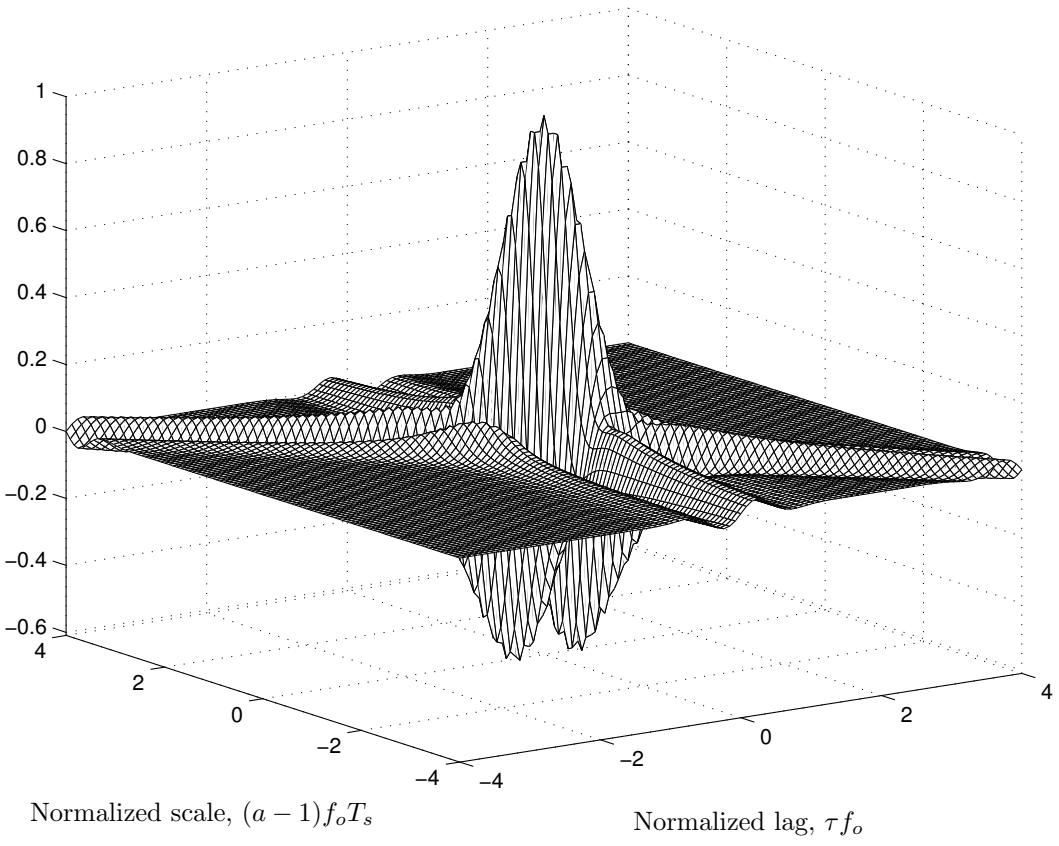

Figure 3.3: Approximate wideband ambiguity function $\bar{\chi}(a,\tau)$ with a second-derivative Gaussian chip pulse (3.3).

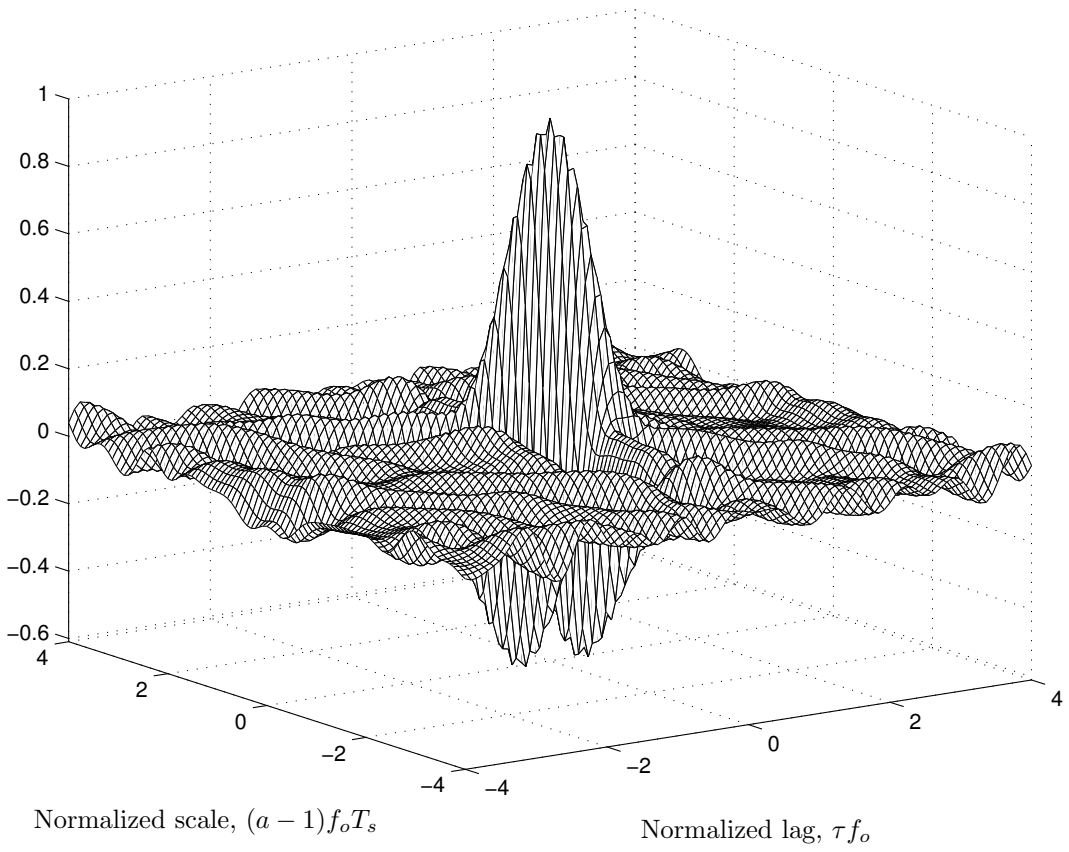

Figure 3.4: Deterministic wideband ambiguity function $\chi(a,\tau)$ of a DSSS waveform $x(t)$ composed of a length-128 i.i.d. random binary sequence modulating second-derivative Gaussian chip pulses. The chip-pulse spacing is chosen to be $T_o = \frac{2}{f_o}$.

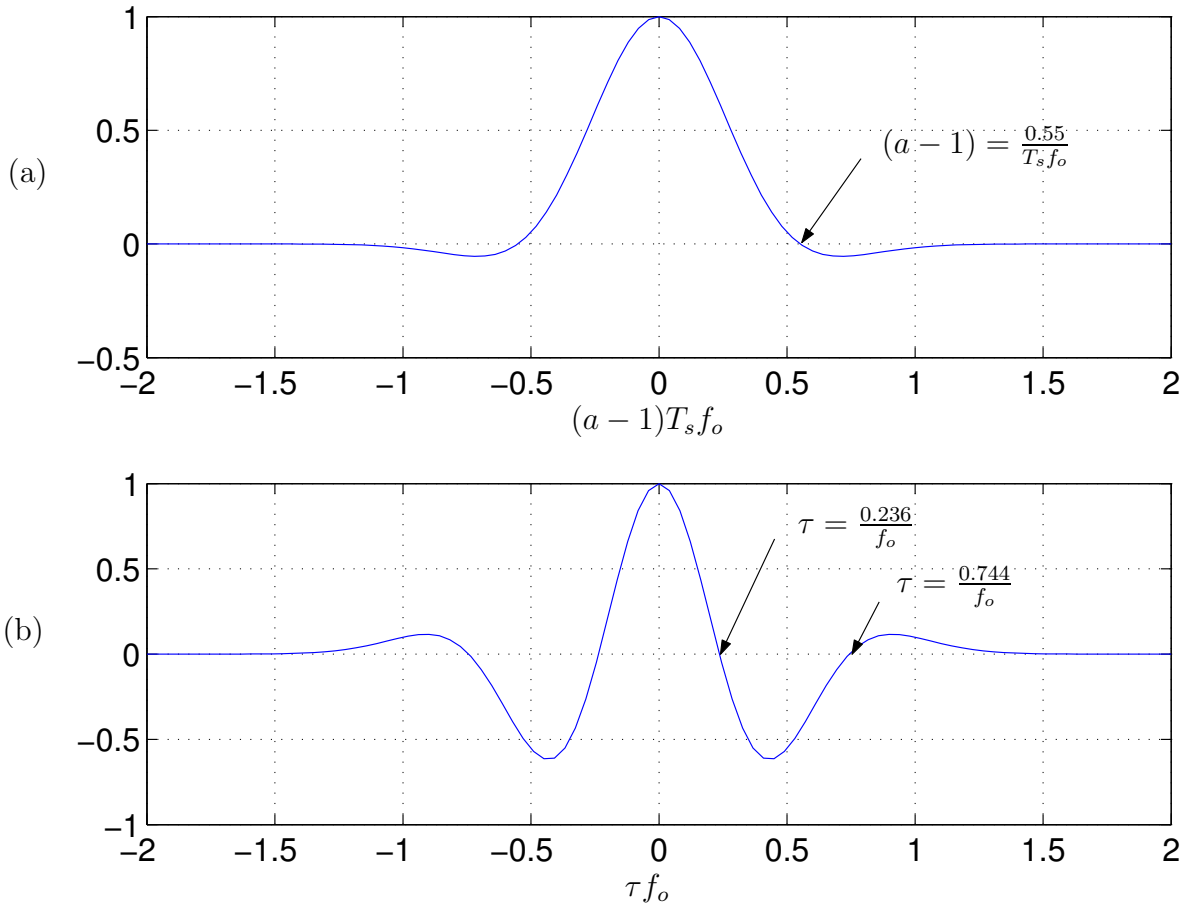

Figure 3.5: Plot of (a) $\bar{\chi}(a, 0)$ and (b) $\bar{\chi}(1, \tau)$ for DSSS waveform employing second-derivative Gaussian chip-pulses.

Quantity	Description
τ_o	Minimum resolvable lag.
α_o	Minimum resolvable dilation.
β_o	Minimum scale resolution, $\beta_o := \alpha_o - 1$.
t_o	Translation-spacing parameter of scale-lag Rake.
a_o	Dilation-spacing parameter of scale-lag Rake.
γ_o	Scale-spacing parameter of scale-lag Rake, $\gamma_o := a_o - 1$
k_t	Relation parameter between t_o and f_o, $k_t := t_o f_o$
k_γ	Relation parameter between γ_o and $T_s f_o$, $k_\gamma := \gamma_o T_s f_o$

Table 3.1: Outline of scale-lag resolution quantities.

3.1.1 Discussion

We define the *normalized scale spread* to be the ratio $\frac{\gamma_{\max}}{1/T_s f_o} = \gamma_{\max} T_s f_o$. The normalized scale spread can be written in terms of the mobile velocity, speed of signal propagation, and the time-bandwidth product (cf. (2.30)):

$$\gamma_{max} T_s f_o \;=\; \frac{v_{max}}{c} T_s f_o. \tag{3.8}$$

Note the similarity to the normalized Doppler-frequency spread [75, p. 809]:

$$f_{\max} T_s \;=\; \frac{v_{max}}{c} T_s f_c, \tag{3.9}$$

where f_c is the carrier frequency and $f_{\max} = \frac{v_{max}}{c} f_c$ is the single-sided Doppler frequency spread. In Chapter 6 we show that the normalized scale spread captures, in a single parameter, the wideband channel's effective rate of variation, just as the normalized Doppler spread captures that for the narrowband baseband-equivalent channel.

3.2 Choice of Basis Functions

From the scale-lag resolution properties of Section 3.1, and to match the scale-lag spreading of the wideband channel as outlined in Section 2.4.2, it is natural to choose as basis functions for demodulating the k^{th} bit the set of dilated-delayed versions of the DSSS waveform $x(t)$ [c.f., (2.2)]:

$$x_{m,n}^{(k)}(t) = \frac{1}{\sqrt{a_o^m}} x\left(\frac{t - nt_o a_o^m - kT_s}{a_o^m}\right), \tag{3.10}$$

where a_o is the *dilation-spacing* parameter. Define $\gamma_o := a_o - 1$ as the *scale-spacing* parameter. Recall from Section 2.3 that t_o is the *translation-spacing* parameter.

With an eye toward the minimum resolution quantities α_o and τ_o, the scale- and translation-spacing parameters are chosen relative to the spectral peak f_o and symbol duration T_s, i.e., $\gamma_o = \frac{k_\gamma}{T_s f_o}$ and $t_o = \frac{k_t}{f_o}$, where k_γ and k_t are relation parameters chosen by the designer. For the case of second-derivative Gaussian chip pulses, the choices $k_\gamma = 0.55$ and $k_t = 0.236$ imply that the dilation-spacing and translation-spacing are equal to the minimum resolvable dilation and lag, respectively.

In Chapter 4, we examine the choice of relation parameters k_γ and k_t through a frame-theoretic analysis. For second-derivative Gaussian chip pulses, $k_t = 0.236$ is a good choice, in the sense that for a wide range of k_γ the set of scale-lag Rake functions (3.10) is, on average, a tight frame; hence, the scale-lag Rake projection coefficients are a set of sufficient statistics for the detector. This is verified in Chapter 5, where we examine numerically the effects of different choices of k_t and k_γ on the scale-lag Rake performance.

The projection of the received signal onto the scale-lag basis functions (3.10) and subsequent whitened matched-filter combining of the projection coefficients[8] constitutes the *scale-lag Rake* receiver. The scale-lag Rake can be thought of as a union of the conventional lag-only Rake with the set of functions $\{x_{m,n}^{(k)},\ m \neq 0\}$. These "extra" functions resolve time-dilated multipath, which arise when there is a dynamic physical channel geometry between the transmitter and receiver.

Let us now calculate the scale-lag Rake projection coefficients $\{r_{m,n}^{(k)}\}$. Here we use the wideband channel model in the analysis.

$$\begin{aligned}
r_{m,n}^{(k)} &= \langle x_{m,n}^{(k)}(t), r(t)\rangle, \\
&= \sum_{l=0}^{N_b-1} b_l \underbrace{\left\langle x_{m,n}^{(k)}(t), \int_0^{\tau_{\max}} \int_{a_{\min}}^{a_{\max}} \mathcal{L}(a,\tau) \frac{1}{\sqrt{a}} x\left(\frac{t-\tau-lT_s}{a}\right) da\, d\tau \right\rangle}_{\approx 0,\ \text{for } l\neq k \text{ since } \tau_{\max} \ll T_s} \\
&\quad + \underbrace{\langle x_{m,n}^{(k)}(t), w(t)\rangle}_{w_{m,n}^{(k)}}, \\
&\approx b_k \underbrace{\left\langle x_{m,n}^{(k)}(t), \int_0^{\tau_{\max}} \int_{a_{\min}}^{a_{\max}} \mathcal{L}(a,\tau) \frac{1}{\sqrt{a}} x\left(\frac{t-\tau-kT_s}{a}\right) da\, d\tau \right\rangle}_{h_{m,n}^{(k)}} + w_{m,n}^{(k)}, \\
&= b_k h_{m,n}^{(k)} + w_{m,n}^{(k)}. \qquad (3.11)
\end{aligned}$$

where $\{h_{m,n}^{(k)}\}$ are the channel coefficients and $\{w_{m,n}^{(k)}\}$ are the noise coefficients. As in (2.38), we vectorize the coefficients for ease of notation:

$$\boldsymbol{r}_k = b_k \boldsymbol{h}_k + \boldsymbol{w}_k \qquad (3.12)$$

where $\boldsymbol{r}_k := [r_{-M,0}^{(k)}, \ldots, r_{0,0}^{(k)}, \ldots, r_{M,N}^{(k)}]^T$; $\boldsymbol{h}_k$ and $\boldsymbol{w}_k$ are defined likewise. The number of coefficients is $(2M+1)(N+1)$ where we choose $M = \lceil \frac{\gamma_{max}}{\gamma_o} \rceil + 1$ and $N = \lceil \frac{\tau_{max}}{t_o} \rceil + 1$

[8] See Section 2.3 for a discussion of whitened matched filtering.

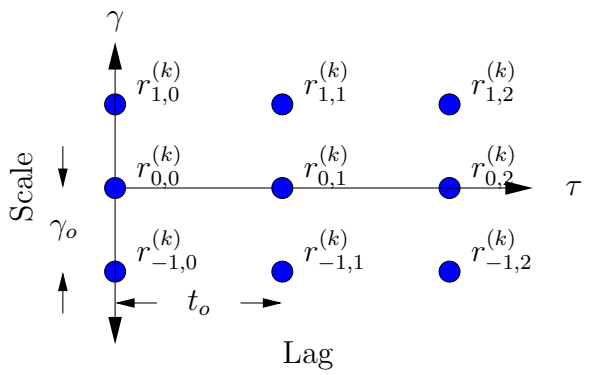

Figure 3.6: Sampling the scale-lag plane.

to capture a significant portion of the received energy in the channel coefficients. These choices are based on the wideband canonical model approximation analysis in Section 2.4.2.

The scale-lag Rake projection coefficients $\{r_{m,n}^{(k)}\}$ are effectively a sampling of the scale-lag plane, as shown in Fig. 3.6. A Taylor series approximation around $a_o = 1$ gives $a_o^m \approx 1 + m(a_o - 1) = 1 + m\gamma_o$; hence, a uniform spacing in the scale domain suffices for typical values of dilation (i.e., $a \approx 1$).

3.2.1 Low-Complexity Scale-Lag Rake Implementation

Anticipating the high expense of accurate wideband analog filtering, we propose a low-complexity means of scale-lag projection. Specifically, we feed the output of a single chip-matched filter into a bank of samplers with rates $(a_o^m t_o)^{-1}, m \in \{-M, \ldots, M\}$ according to the translation- and dilation-spacing parameters. Each sampler output is connected to a traditional (i.e., lag-only) Rake combiner where each finger is downsampled to the chip-pulse rate; we assume for simplicity that the translation spacing

parameter t_o divides evenly into the chip-pulse spacing parameter T_o, i.e., define $N_t := \frac{T_o}{t_o}$, $N_t \in \mathbb{N}$. We also drop the superscript (k) for notational convenience. This structure can be justified as follows:

$$\begin{aligned}
r_{m,n} &= \int x_{m,n}(t) r(t) dt, \\
&= \frac{1}{a_o^{m/2}} \sum_{i=0}^{N_p-1} \frac{c_i}{\sqrt{N_p}} \int p\left(\frac{t - nt_o a_o^m - iT_o a_o^m}{a_o^m}\right) r(t) dt, \\
&= \frac{1}{a_o^{m/2}} \sum_{i=0}^{N_p-1} \frac{c_i}{\sqrt{N_p}} \, p\left(-\frac{t}{a_o^m}\right) * r(t)\Big|_{t=(n+iN_t)a_o^m t_o}, \\
&\approx \frac{1}{a_o^{m/2}} \sum_{i=0}^{N_p-1} \frac{c_i}{\sqrt{N_p}} p\left(-t\right) * r(t)\Big|_{t=(n+iN_t)a_o^m t_o}, \\
&= \frac{1}{a_o^{m/2}} \sum_{i=0}^{N_p-1} \frac{c_i}{\sqrt{N_p}} z_{m,n}[i], \qquad (3.13)
\end{aligned}$$

where $*$ denotes linear convolution and where

$$z_{m,n}[i] = p\left(-t\right) * r(t)\Big|_{t=(n+iN_t)a_o^m t_o}. \qquad (3.14)$$

The approximation in the penultimate step of (3.13) is valid because dilating the chip pulse $p(t)$ by a_o^m is insignificant compared to dilating the entire DSSS waveform $x(t)$. A block diagram of the basis projection is shown in Fig. 3.7. Notice that the translation-spacing t_o is essentially the sampling period of the lag-only Rake receiver (e.g., $m = 0$ components); scale components ($m \neq 0$) are obtained by slightly lengthening or shortening the sampling period.

An interesting question to investigate in future work would be how sampling frequency offsets affect the performance of the scale-lag Rake. We conjecture that as long as the sampling of the scale-lag plane is "dense" enough to collect all the

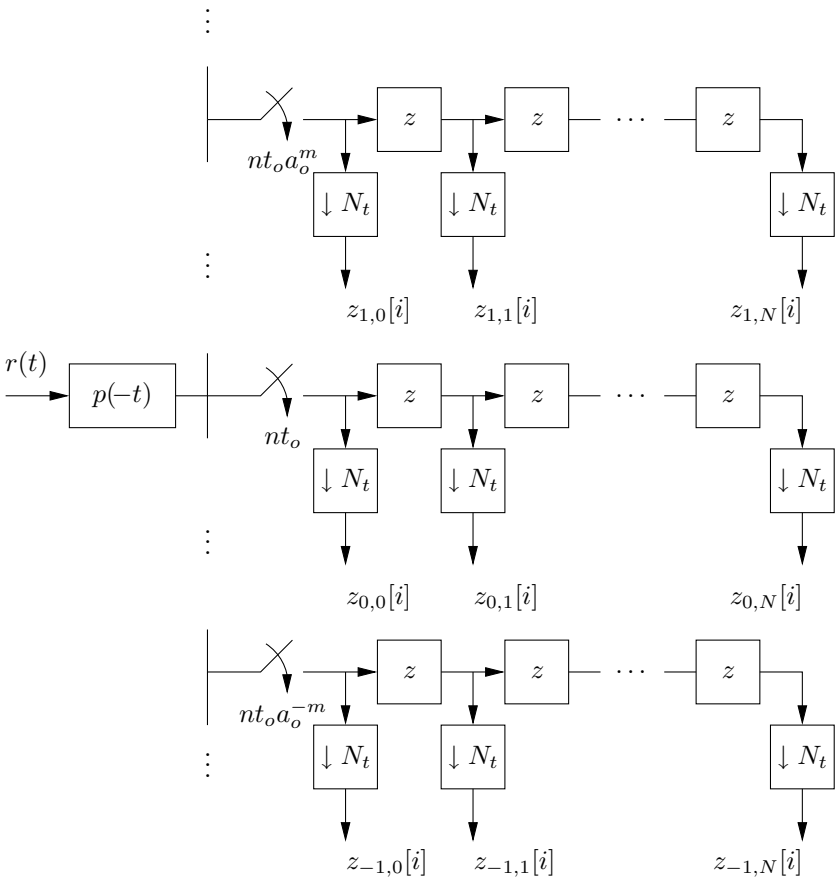

Figure 3.7: Block-diagram for the scale-lag Rake projection given by equation (3.13). The receiver can easily be made causal by introducing an appropriate bulk delay in the matched filter.

received energy, then frequency offsets shouldn't significantly adversely impact the performance.

3.3 Connection to Radar, Sonar, and Wavelets

The reader will notice that if $x(t)$ satisfies the wavelet admissibility condition [62, p. 125], then $\chi(a, \tau)$ is the continuous wavelet transform (CWT) with respect to $x(t)$. It is easily verified in Appendix 3.6 that if the chip pulse $p(t)$ is admissible, then the waveform $x(t)$ is also admissible. A necessary condition of admissibility is for the waveform to have a zero at DC; hence, an arbitrarily chosen wavelet will satisfy Proposition 2. The connection between wavelet analysis and wideband processing for Radar and Sonar is studied in [98], and experimental results are reported in [55].

The affect of time dilation on spread-spectrum signals is sometimes called code Doppler. A study of the effect of code Doppler on timing acquisition was performed in [33]. There were no papers attempting to exploit the presence of code Doppler for diversity gain. Code Doppler will also occur if there is a sampling frequency mismatch between the transmitter digital to analog converter (DAC) and the receiver analog to digital converter (ADC), in which case every path is dilated by the same amount.

The scale and lag resolution analysis we have performed for DSSS signals could be applied to Radar/Sonar estimation of target velocity and range. Consider the following recent papers on the topic. An exploration on the connection of the wideband ambiguity function (3.1) for arbitrary motion (not just constant velocity) and its constant-velocity narrowband approximation is found in [44]. In [27], the authors investigate the dilation resolution properties of random wideband signals, which are generated via a Gaussian noise source. In [88], a ternary-modulated sequence with chips chosen from $\{+1, -1, 0\}$ was used to estimate range and velocity. In [52], the

authors estimate range by determining when the pulse first arrives. In [72], a Cramer-Rao lower bound (CRLB) on the estimation error of velocity and range via wideband signals is calculated based on the Mellin transform [6]. One avenue of future work is to design optimal CRLB-minimizing chip-pulses by applying the Mellin transform analysis in [72] to our ambiguity-function approximations.

3.4 Appendix: Proof of Propositions 1 and 2

In this appendix, we state and prove a series of three lemmas and use them to prove Propositions 1 and 2.

Lemma 3 *The expectation of the wideband ambiguity function (3.1) can be approximated as* $\mathrm{E}[\chi(a,\tau)] \approx \bar{\chi}(a,\tau)$*, where* $\bar{\chi}(a,\tau)$ *is defined as (3.5) and the expectation is taken over the random chip sequence.*

Proof: Assuming that the ternary pseudonoise (PN) sequence is i.i.d., we can write

$$\begin{aligned}
\mathrm{E}\left[\chi(a,\tau)\right] &= \mathrm{E}\left[\int_{-\infty}^{\infty} x(t)\frac{1}{\sqrt{a}}x\left(\frac{t-\tau}{a}\right)dt\right], \\
&= \sum_{i=0}^{N_p-1}\frac{\mathrm{E}[c_i^2]}{N_p\sqrt{a}}\int_{-\infty}^{\infty} p(t)p\left(\frac{t-\tau-(a-1)iT_o}{a}\right)dt. \\
&= \sum_{i=0}^{N_p-1}\frac{\mathrm{E}[c_i^2]}{N_p}\chi_p\left(a,\tau+(a-1)iT_o\right) \qquad (3.15)
\end{aligned}$$

where $\chi_p(a,\tau)$, the ambiguity function of the chip pulse, is defined in (3.6).

The chip-pulse spacing parameter is $T_o = \frac{T_s}{N_p}$; hence, we make the following integral approximation of (3.15):

$$\sum_{i=0}^{N_p-1}\frac{1}{N_p}\chi_p\left(a,\tau+(a-1)\frac{i}{N_p}T_s\right) \approx \int_0^1 \chi_p(a,\tau+(a-1)zT_s)dz, \qquad (3.16)$$

which is very tight for large N_p. We have also used the fact that $\mathrm{E}[c_i^2] = 1$.

Since we are considering dilations a very close to unity, (3.16) can be further approximated by

$$\begin{aligned}\int_0^1 \chi_p(a,(a-1)zT_s)dz &\approx \int_0^1 \chi_p(1,(a-1)zT_s)dz,\\ &= \bar{\chi}(a,\tau). \quad \square\end{aligned}$$

Lemma 4 *The expectation of the product of wideband ambiguity functions can be approximated as* $\mathrm{E}[\chi(a,\tau)\chi(a',\tau')] \approx \bar{\chi}(a,\tau)\bar{\chi}(a',\tau')$*, where the expectation is taken over the random chip sequence.*

Proof: The use of a random spreading code simplifies the computation

$$\begin{aligned}\mathrm{E}[\chi(a,\tau)\chi(a',\tau')] &= \frac{1}{N_p^2}\sum_{i,j,k,l}\mathrm{E}[c_ic_jc_kc_l]\\ &\quad \chi_p(a,\tau+(ai-j)T_o)\chi_p(a',\tau'+(a'k-l)T_o), \qquad (3.17)\end{aligned}$$

where $\chi_p(a,\tau)$ is defined in (**??**). The number of terms in (3.17) can be reduced by noting that

$$\mathrm{E}[c_ic_jc_kc_l] = \begin{cases}\mathrm{E}[c_i^4] & i=j=k=l,\\ \mathrm{E}[c_i^2]^2 & i=j,\ k=l,\ i\neq k,\\ \mathrm{E}[c_i^2]^2 & i=k,\ j=l,\ i\neq j,\\ \mathrm{E}[c_i^2]^2 & i=l,\ j=k,\ i\neq j,\\ 0 & \text{else.}\end{cases} \qquad (3.18)$$

Hence, we need only compute the non-zero terms outlined in (3.18). We will find that only the second case will produce a non-negligible contribution. Note that the chip-pulse spacing parameter is $T_o = \frac{T_s}{N_p}$.

The absolute value of (3.17) for the case $i=j=k=l$ is upper bounded by

$$\sum_{i=0}^{N_p-1}\frac{\mathrm{E}[c_i^4]}{N_p^2}\left|\chi_p\left(a,\tau+(a-1)\tfrac{i}{N_p}T_s\right)\chi_p\left(a',\tau'+(a'-1)\tfrac{i}{N_p}T_s\right)\right| \le \frac{\mathrm{E}[c_i^4]}{N_p}, \qquad (3.19)$$

where the inequality in (3.19) follows from the chip pulse having bounded energy, i.e., $\chi_p(a,\tau) \leq 1, \forall\, a, \tau$. Hence, for a large number N_p of chips, the sum of the terms in the first case of (3.18) is negligible.

For the second case, $i = j$, $k = l$, $i \neq k$, we have

$$\begin{aligned}
&\sum_{i,k\neq i} \frac{\mathrm{E}[c_i^2]^2}{N_p^2} \chi_p\left(a, \tau+(a-1)\tfrac{i}{N_p}T_s\right) \chi_p\left(a, \tau'+(a'-1)\tfrac{k}{N_p}T_s\right) \\
&\quad \approx \mathrm{E}[c_i^2] \int_0^1 \chi_p(1, \tau+(a-1)zT_s)dz\, \mathrm{E}[c_i^2] \int_0^1 \chi_p(1, \tau'+(a'-1)z'T_s)dz' \\
&\quad = \bar{\chi}(a,\tau)\bar{\chi}(a',\tau') \qquad (3.20)
\end{aligned}$$

For the third case, $i = k$, $j = l$, $i \neq j$, we have

$$\begin{aligned}
&\sum_{i,j\neq i} \frac{\mathrm{E}[c_i^2]^2}{N_p^2} \left| \chi_p\left(a, \tau+(ai-j)T_o\right) \chi_p\left(a', \tau'+(a'i-j)T_o\right) \right| \\
&\quad \approx \sum_{i,j} \frac{\mathrm{E}[c_i^2]^2}{N_p^2} \left| \chi_p\left(1, \tau+(ai-j)T_o\right) \chi_p\left(1, \tau'+(a'i-j)T_o\right) \right| \qquad (3.21) \\
&\quad \leq \sum_{i=0}^{N_p-1} \frac{2\,\mathrm{E}[c_i^2]^2}{N_p^2} \;=\; \frac{2\,\mathrm{E}[c_i^2]^2}{N_p} \qquad (3.22)
\end{aligned}$$

The approximation in (3.21) is tight when a and a' are close to unity. Since the chip pulse is time-limited to T_p seconds, the function $\chi_p(1,z)$ is non-zero only when $|z| < T_p$. Therefore, given a and τ, for each $i \in 1, 2, \ldots, N_p - 1$, there are at most two values of j such that $|\frac{\tau}{T_o}+ai-j| < \frac{T_p}{T_o}$. This observation, combined with the fact that $|\chi_p(a,\tau)| < 1,\ \forall\, a, \tau$, leads to the inequality in (3.22). Thus, for a large number N_p of chips, the sum of the terms in the third case is negligible. Similarly, the sum of the terms in the fourth case $i = l$, $j = k$, $i \neq j$ can be shown to be negligible.

In summary, we have that only the second case gives non-negligible results, hence

$$\mathrm{E}[\chi(a,\tau)\chi(a',\tau')] \;\approx\; \bar{\chi}(a,\tau)\bar{\chi}(a',\tau').$$

where $\bar{\chi}(\cdot,\cdot)$ is defined in (3.5). $\square$

Lemma 5 *For N_p large and a near unity, the wideband ambiguity function $\chi(a,\tau)$ is approximately equal to $\bar{\chi}(a,\tau)$ in the mean-squared sense, where the expectation is taken over the random chip sequence.*

Proof: We use Lemmas 3 and 4 to write the following

$$\begin{aligned} \mathrm{E}[|\chi(a,\tau)-\bar{\chi}(a,\tau)|^2] &= \mathrm{E}[(\chi(a,\tau))^2] - 2\,\mathrm{E}[\chi(a,\tau)]\bar{\chi}(a,\tau) + (\bar{\chi}(a,\tau))^2 \quad (3.23) \\ &\approx 0. \quad \square \quad (3.24) \end{aligned}$$

Proof of Proposition 1

From Lemma 5, we see that $\bar{\chi}(1,\tau)$ is a mean-square approximation of $\chi(1,\tau)$; hence, from (3.5)

$$\begin{aligned} \chi(1,\tau) &\approx \int_0^1 \chi_p(1,\tau)dz \quad (3.25) \\ &= \chi_p(1,\tau). \quad (3.26) \end{aligned}$$

The function $\chi_p(1,\tau) = 0$ when $\tau > T_p$. $\square$

Proof of Proposition 2

From Lemma 5, we see that $\bar{\chi}(a,0)$ is a mean-square approximation of $\chi(a,0)$; hence, from (3.5)

$$\begin{aligned} \chi(a,0) &\approx \int_0^1 \chi_p(1,(a-1)zT_s)dz \quad (3.27) \\ &= \int_0^1 R_p((a-1)zT_s)dz \quad (3.28) \\ &= \frac{1}{2(a-1)T_s}\int_{-(a-1)T_s}^{(a-1)T_s} R_p(z)dz. \quad (3.29) \end{aligned}$$

where $R_p(\tau) := \chi_p(1,\tau)$ is the deterministic autocorrelation function of the chip pulse $p(t)$. Suppose $S_p(0) = 0$ where $S_p(f)$ is the energy spectral density of the chip pulse. Since the chip pulse has time support of T_p seconds, then for $(a-1)T_s \geq T_p \Leftrightarrow a \geq 1 + \frac{T_p}{T_s}$ we have

$$\begin{aligned} \chi(a,\tau) &\approx S_p(0), \\ &= 0, \end{aligned} \tag{3.30}$$

for N_p large and a near unity. $\square$

3.5 Appendix: Wideband Ambiguity Function for Second-Derivative Chip Pulse

The closed-form ambiguity function expression for the unit energy second-derivative Gaussian chip pulse is quickly derived by using Parseval's theorem to perform the inner product calculation in the frequency domain:

$$\chi_p(a,\tau) = \int_{-\infty}^{\infty} \frac{1}{\sqrt{a}} p\left(\frac{t-\tau}{a}\right) p(t)dt, \tag{3.31}$$

$$= \int_{-\infty}^{\infty} \sqrt{a}\exp(-j2\pi\tau)P(af)P^*(f)df, \tag{3.32}$$

where the Fourier transform $P(f)$ of the chip pulse $p(t)$ is

$$P(f) = \frac{\sqrt{f_o}\sqrt[4]{32\pi}}{\sqrt{3}} \frac{2}{\sqrt{\pi f_o^2}} \left(\frac{f}{f_o}\right)^2 e^{-\frac{f^2}{f_o^2}}. \tag{3.33}$$

We complete the square of the argument of the exponential in (3.32) and make use of the expression of the fourth Gaussian moment to write the solution as

$$\begin{aligned} \chi_p(a,\tau) &= f(a)\left(4\pi^4 f_o^4\tau^4 - 12\pi^2 f_o^2\tau^2(1+a^2) + 3(1+a^2)^2\right) \\ &\quad \exp\left(-\frac{\pi^2 f_o^2\tau^2}{1+a^2}\right), \end{aligned} \tag{3.34}$$

where $f(a) = \frac{4}{3}\sqrt{\frac{2a^5}{(1+a^2)^9}}$.

3.6 Appendix: Admissibility of DSSS Waveform

In this appendix, we show that a direct-sequence spread spectrum (DSSS) signal is admissible if the chip-pulse is admissible. A signal $g(t)$ is *admissible* if the following condition holds

$$\int_{-\infty}^{\infty} \frac{|G(f)|^2}{|f|} df < +\infty, \tag{3.35}$$

where $G(f)$ is the Fourier transform of $g(t)$. Recall that the DSSS signal $x(t)$ is

$$x(t) = \frac{1}{\sqrt{N_p}} \sum_{i=0}^{N_p-1} c_i p(t - iT_o), \tag{3.36}$$

and has Fourier transform

$$X(f) = \frac{P(f)}{\sqrt{N_p}} \sum_{i=0}^{N_p-1} c_i e^{j2\pi i T_o)}, \tag{3.37}$$

where $P(f)$ is the Fourier transform of the chip pulse. Now plug (3.37) into the admissibility condition (3.35) to get

$$\begin{aligned}
\int_{-\infty}^{\infty} \frac{|X(f)|^2}{|f|} df &= \int_{-\infty}^{\infty} \frac{|P(f)|^2}{|f|} \frac{\left|\sum_{i=0}^{N_p-1} c_i e^{-j2\pi f i T_o}\right|^2}{N_p} df && (3.38)\\
&\leq \int_{-\infty}^{\infty} \frac{|P(f)|^2}{|f|} \frac{\sum_{i=0}^{N_p-1} |c_i e^{-j2\pi f i T_o}|^2}{N_p} df && (3.39)\\
&= \underbrace{\frac{1}{N_p} \sum_{i=0}^{N_p-1} |c_i|^2}_{=1} \int_{-\infty}^{\infty} \frac{|P(f)|^2}{|f|} df && (3.40)\\
&< +\infty && (3.41)
\end{aligned}$$

Hence, an admissible chip pulse $p(t)$ implies that the DSSS signal $x(t)$ is also admissible.

CHAPTER 4

FRAME THEORY AND THE SCALE-LAG RAKE RECEIVER

In this chapter, we take a frame-theoretic view of the scale-lag Rake functions[9] $\{x_{m,n}(t)\}$ in the design of translation and dilation spacing parameters t_o and a_o. Our goal is to find the range of t_o and a_o values such that the scale-lag Rake functions constitute a frame. The designation of frame status means that the scale-lag Rake functions can represent any signal and hence can provide a set of sufficient statistics for bit detection. We compile and study numerical frame bounds for a DSSS waveform derived from second-derivative Gaussian chip pulses.

4.1 Introduction to Frame Theory

A "frame" is a set of not-necessarily independent vectors that can act as an expansion for any vector in the space. In other words, if we project any vector onto the frame, we should somehow be able to reconstruct the original vector from the projection coefficients. We would like the projection to be linear; thus, if our original vector has bounded energy, then the norm of the frame expansion should also be bounded.

[9]We drop the superscript (k) on the scale-lag Rake functions for notational convenience.

To state the first condition, reconstruction, more mathematically, let $\mathcal{H}$ be a Hilbert space and choose a set $\{\varphi_j\}_{j\in J} \subset \mathcal{H}$. Define $T : \mathcal{H} \to \mathbb{C}^{|J|}$ to be the linear transformation which projects vectors in $\mathcal{H}$ onto the set $\{\varphi_j\}_{j\in J}$, i.e.,

$$(Tf)_j := \langle \varphi_j, f \rangle = c_j, \tag{4.1}$$

for $f \in \mathcal{H}$. The transformation T maps $\mathcal{H}$ into the space of sequences with indices J. Recall that a linear transformation is invertible on its range if and only if its null space contains only the zero vector $\{0\}$; in other words, any vector with positive energy must be mapped away from zero. Thus, to be able to reconstruct $f \in \mathcal{H}$ from the projection coefficients $\{c_j\}_{j\in J}$, the transformation T must satisfy

$$0 < A\|f\|^2 \leq \|Tf\|^2 = \sum_{j\in J} |\langle \varphi_j, f \rangle|^2 \tag{4.2}$$

for some $A > 0$ and for every $f \in \mathcal{H}$, $f \neq 0$. An implication of (4.2) is that the span of the set $\{\varphi_j\}_{j\in J}$ must be at least dense in $\mathcal{H}$; otherwise, we could find a nonzero vector $f^\perp \in \mathcal{H}$ that is orthogonal to every φ_j.

The second condition, bounded energy, can be stated as follows. The transformation T has bounded energy if there is a $B < \infty$ such that for every $f \in \mathcal{H}$,

$$\|Tf\|^2 = \sum_{j\in J} |\langle \varphi_j, f \rangle|^2 \leq B\|f\|^2. \tag{4.3}$$

In other words, T maps vectors in $\mathcal{H}$ into $\ell^2(J)$, the space of square-summable sequences with indices J. Recalling that bounded linear transformations are continuous, we see that if T satisfies (4.3), then it is a continuous mapping from $\mathcal{H}$ into $\ell^2(J)$.

From (4.2) and (4.3), we are ready to state the definition of a frame. A set of vectors $\{\varphi_j\}_{j\in J}$ in a Hilbert space $\mathcal{H}$ is called a *frame* if there exist constants $A > 0$,

$B < \infty$ such that

$$A\|f\|^2 \leq \sum_{j \in J} |\langle \varphi_j, f \rangle|^2 \leq B\|f\|^2 \tag{4.4}$$

for all $f \in \mathcal{H}$.

4.1.1 Tight Frames

A *tight frame* has equal frame bounds, $A = B$. For a tight frame, reconstruction is straightforward [24, p. 56]

$$f = A^{-1} \sum_j \langle f, \varphi_j \rangle \varphi_j. \tag{4.5}$$

Furthermore, when the frame elements have unit energy, the tight frame bound A can be interpreted as a measure of the frame "redundancy," i.e., the ratio of the number of frame elements to the dimension of the space. If $\{\varphi_j\}_{j \in J}$ is a tight frame with frame bound $A = 1$, and each φ_j has unit norm $\|\varphi_j\| = 1$, then the frame $\{\varphi_j\}$ is an orthonormal basis for $\mathcal{H}$ [24, p.57].

4.1.2 Snug Frames

Given $\varepsilon > 0$, we say a frame is *snug* if the frame bounds satisfy $B/A - 1 < \varepsilon$ [23]. Given small epsilon ($\varepsilon \approx .01$), (4.5) can be used as an approximate reconstruction formula for snug frames.

4.2 Average Frame Bounds for DSSS Signal

Now let us return to the original question: does our scale-lag basis $\{x_{m,n}(t)\}_{m,n \in \mathbb{Z}}$ constitute a frame, and what are the implications? Recall that $x_{m,n}(t) = \frac{1}{\sqrt{a_o^m}} x\left(\frac{t - n t_o a_o^m}{a_o^m}\right)$, where $x(t) = \frac{1}{\sqrt{N_p}} \sum_{i=0}^{N_p - 1} c_i p(t - iT_o)$. Since the "mother"

basis function $x_{0,0}(t)$ is constructed from a pseudo-random sequence of wavelet chip pulses, we take a statistical approach, that is, we seek bounds on the expectation of the norm of the frame projection. We call these *average* frame bounds and proceed by taking the expectation of (4.4) when the frame is $\{x_{m,n}(t)\}_{m,n\in\mathbb{Z}}$. We follow closely the analysis in [24, p.67].

$$\begin{aligned}
\mathrm{E}\left[\sum_{m,n\in\mathbb{Z}} |\langle f, x_{m,n}\rangle|^2\right] &= \sum_{m,n} \mathrm{E}\left|\int_{-\infty}^{\infty} F(\omega) a_o^{m/2} X^*(a_o^m\omega) e^{jt_o a_o^m n\omega} d\omega\right|^2 \\
&= \sum_{m,n} a_o^m \,\mathrm{E}\left|\int_0^{2\pi t_o^{-1} a_o^{-m}} e^{jt_o a_o^m n\omega} \sum_{\ell\in\mathbb{Z}} F(\omega + 2\pi\ell a_o^{-m} t_o^{-1}) X^*(a_o^m\omega + 2\pi\ell t_o^{-1}) d\omega\right|^2 \\
&= \frac{2\pi}{t_o} \sum_m \int_0^{2\pi t_o^{-1} a_o^{-1}} \mathrm{E}\left|\sum_{\ell\in\mathbb{Z}} F(\omega + 2\pi\ell a_o^{-m} t_o^{-1}) X^*(a_o^m\omega + 2\pi\ell t_o^{-1})\right|^2 d\omega \\
&= \frac{2\pi}{t_o} \sum_{m,k\in\mathbb{Z}} \int_{-\infty}^{\infty} F(\omega) F^*(\omega + 2\pi k a_o^{-m} t_o^{-1}) \,\mathrm{E}\left[X^*(a_o^m\omega) X(a_o^m\omega + 2\pi k t_o^{-1})\right] d\omega.
\end{aligned} \tag{4.6}$$

We now calculate the expectation in (4.6):

$$\begin{aligned}
\mathrm{E}\left[X^*(a_o^m\omega) X(a_o^m\omega + 2\pi k t_o^{-1})\right] &= \frac{1}{N_p} \sum_{l,l'=0}^{N_p-1} \mathrm{E}[c_l c_{l'}] \\
&\quad P^*(a_o^m\omega) P(a_o^m\omega + 2\pi k t_o^{-1}) e^{j[(l-l')T_o a_o^m\omega - 2\pi k l' \frac{T_o}{t_o}]} \\
&= P^*(a_o^m\omega) P(a_o^m\omega + 2\pi k t_o^{-1}) \sum_{l=0}^{N_p-1} \frac{1}{N_p} e^{-j2\pi k l \frac{T_o}{t_o}}
\end{aligned} \tag{4.7}$$

where we have used the fact that

$$\begin{aligned}
X(\omega) &= \frac{1}{\sqrt{2\pi}} \int_{-\infty}^{\infty} x(t) e^{j\omega t} dt \\
&= \frac{1}{\sqrt{N_p}} P(\omega) \sum_{l=0}^{N_p-1} e^{-jlT_o\omega}
\end{aligned}$$

and

$$\mathrm{E}[c_l c_{l'}] = \begin{cases} \mathrm{E}[c_l^2] = 1, & l = l' \\ 0, & \text{otherwise.} \end{cases}$$

Substituting (4.7) into (4.6), we have

$$\mathrm{E}\left[\sum_{m,n\in\mathbb{Z}} |\langle f, x_{m,n}\rangle|^2\right] = \frac{2\pi}{t_o}\int_{-\infty}^{\infty} |F(\omega)|^2 \sum_{m\in\mathbb{Z}} |P(a_o^m\omega)|^2 d\omega + \mathrm{Rest}(f). \quad (4.8)$$

$\mathrm{Rest}(f)$ is bounded by (see [24, p.67])

$$|\mathrm{Rest}(f)| \le \frac{2\pi}{t_o}\|f\|^2 \sum_{k\neq 0}\left[\beta\left(\frac{2\pi}{t_o}k\right)\beta\left(-\frac{2\pi}{t_o}k\right)\right]^{1/2}, \quad (4.9)$$

where

$$\beta(s) := \sup_{\omega}\sum_{m\in\mathbb{Z}} |P(a_o^m\omega)||P(a_o^m\omega + s)|. \quad (4.10)$$

We are now ready to restate Proposition 3.3.2 from [24, p.69] for the case of spread-spectrum waveforms.

Proposition 6 *Suppose* $x(t) = \frac{1}{\sqrt{N_p}}\sum_{l=0}^{N_p-1} c_l p(t - lT_o)$ *is a spread-spectrum waveform composed of unit-norm wavelet chip-pulses* $p(t)$*. Suppose also that the spreading sequence* $\{c_l\}_{l=0}^{N_p-1}$ *is modeled as i.i.d. If* $p(t)$*,* a_o *are such that*

$$\inf_{1\le|\omega|\le a_o}\sum_{m=-\infty}^{\infty} |P(a_o^m\omega)|^2 > 0, \quad (4.11)$$

$$\sup_{1\le|\omega|\le a_o}\sum_{m=-\infty}^{\infty} |P(a_o^m\omega)|^2 < \infty, \quad (4.12)$$

and if $\beta(s) = \sup_\omega \sum_m |P(a_o^m\omega)||P(a_o^m\omega + s)|$ *decays at least as fast as* $(1+|s|)^{-(1+\varepsilon)}$*, with* $\varepsilon > 0$*, then there exists* $(t_o)_{\mathrm{thr}} > 0$ *such that,* on average*, the* $x_{m,n}(t) =$

$\frac{1}{a_o^{m/2}} x\left(\frac{t-t_o a_o^m}{a_o^m}\right)$ *constitute a frame for all choices* $t_o < (t_o)_{\text{thr}}$. *For* $t_o < (t_o)_{\text{thr}}$, *the following expressions are frame bounds,* on average, *for the* $x_{m,n}(t)$*:*

$$A = \frac{2\pi}{t_o}\left\{\inf_{1\le|\omega|\le a_o}\sum_{m=-\infty}^{\infty}|P(a_o^m\omega)|^2 - \sum_{k\neq 0}\left[\beta\left(\frac{2\pi}{t_o}k\right)\beta\left(-\frac{2\pi}{t_o}k\right)\right]^{1/2}\right\}, \quad (4.13)$$

$$B = \frac{2\pi}{t_o}\left\{\sup_{1\le|\omega|\le a_o}\sum_{m=-\infty}^{\infty}|P(a_o^m\omega)|^2 + \sum_{k\neq 0}\left[\beta\left(\frac{2\pi}{t_o}k\right)\beta\left(-\frac{2\pi}{t_o}k\right)\right]^{1/2}\right\}, \quad (4.14)$$

The conditions on β *and (4.12) are satisfied if, e.g.,* $|P(\omega)| \le C|\omega|^{\alpha}(1+|\omega|)^{-\gamma}$ *with* $\alpha > 0$, $\gamma > \alpha + 1$.

Let us, for a moment, examine the frame bound expressions (4.13) and (4.14) when the chip pulse has (single-sided) bandwidth W Hertz. If the frame translation parameter t_o is set to $t_o = \frac{1}{2W}$ seconds, then $\beta\left(\pm\frac{2\pi k}{t_o}\right) = 0$ for $k \neq 0$. Suppose also that the dilation parameter a_o is set very close to unity. Then we will have $\inf_{1\le|\omega|\le a_o}\sum_{m=-\infty}^{\infty}|P(a_o^m\omega)|^2 \approx \sup_{1\le|\omega|\le a_o}\sum_{m=-\infty}^{\infty}|P(a_o^m\omega)|^2$ and hence $A \approx B$, i.e., we have a snug frame. In this case, we can calculate the frame bound from the following necessary condition [24, p.63]

$$A \approx \frac{2\pi}{t_o \ln a_o}\int_{-\infty}^{\infty}\frac{|P(\omega)|^2}{|\omega|}d\omega. \quad (4.15)$$

4.3 Average Frame Bounds for DSSS Signals Using Second-Derivative Gaussian Wavelets as Chip Pulses

Let us calculate the frame bounds for a signal $x(t)$ with second-derivative Gaussian wavelet chip pulses, which are used in our scale-lag Rake receiver analysis. The (unit energy) second-derivative Gaussian wavelet (a.k.a. Mexican-hat wavelet [24, p. 75])

is written

$$u(t) = \frac{2}{\sqrt{3}}\pi^{-1/4}(1-t^2)e^{-\frac{t^2}{2}}, \tag{4.16}$$

and has Fourier transform

$$U(\omega) = \frac{2}{\sqrt{3}}\pi^{-1/4}\omega^2 e^{-\frac{\omega^2}{2}}. \tag{4.17}$$

The second-derivative Gaussian wavelet can be dilated to any desired level to obtain the chip pulse: $p(t) = \sqrt{\alpha}u(\alpha t)$. In our case, we set the scaling constant α to be $\alpha := \pi f_o\sqrt{2}$ so that the peak of the frequency response $\sup_\omega |P(\omega)|$ occurs at $2\pi f_o$ radians (f_o Hertz). Thus, (4.16) is equivalent, up to a temporal scaling factor to the chip pulse (3.3). For the second-derivative Gaussian chip pulse, the frame bounds from Proposition 6 are dependent on the product $t_o f_o$ as seen below:

$$A = \frac{\sqrt{2}}{t_o f_o}\left\{\inf_{1\le|\omega|\le a_o}\sum_{m=-\infty}^{\infty}|U(a_o^m\omega)|^2 - \sum_{k\neq 0}\left[\beta_U\left(\frac{\sqrt{2}}{t_o f_o}k\right)\beta_U\left(-\frac{\sqrt{2}}{t_o f_o}k\right)\right]^{1/2}\right\},$$

$$B = \frac{\sqrt{2}}{t_o f_o}\left\{\sup_{1\le|\omega|\le a_o}\sum_{m=-\infty}^{\infty}|U(a_o^m\omega)|^2 + \sum_{k\neq 0}\left[\beta_U\left(\frac{\sqrt{2}}{t_o f_o}k\right)\beta_{\mathsf{mex}}\left(-\frac{\sqrt{2}}{t_o f_o}k\right)\right]^{1/2}\right\},$$

where

$$\beta_U(s) = \sup_\omega\sum_m |U(a_o^m\omega)||U(a_o^m\omega + s)| \tag{4.18}$$

Tables 4.1, 4.2, and 4.3 compile the frame bounds for dilation-spacing parameter settings of $a_o = 2$, $a_o = 1 + 1/64$, and $a_o = 1 + 1/128$, respectively. In each table, the last value of the normalized frame translation parameter $t_o f_o$ is the largest value (in increments of 0.05) such that $A > 0$. Recall that $k_t = t_o f_o$. Values of k_t greater

than 0.35 will "probably" result in shift-dilates of $x(t)$ not being a frame anymore, as stated by Daubechies in [24, p.76]. The choice $k_t = 0.236$, or equivalently $t_o = \tau_o$, implies that the scale-lag basis is a frame and can act as an expansion for any received signal; hence, the scale-lag basis can provide sufficient statistics for the bit detector.

In some instances the translation-spacing parameter may need to be on the order of the chip-pulse duration, i.e., $t_o f_o = 2$. Note that this setting is much greater than the maximum allowable for the shift-dilates of $x(t)$ to be a frame on average! Hence, the scale-lag expansion will not collect all the energy offered by wideband channel output.

Figure 4.1 plots the ratio B/A versus $t_o f_o$. Note the abrupt loosening of the frame as the normalized translation spacing parameter $t_o f_o$ approaches 0.35 regardless of the value of the dilation spacing parameter a_o. Hence, the frame status is not sensitive to the choice of a_o (or equivalently of k_γ). However, tables 4.1, 4.2, and 4.3 indicate that the frame redundancy—the magnitude of A—is greatly impacted by the choice of a_o. We examine this connection next.

Plugging $P(f) = \frac{1}{\sqrt{\alpha}} U(\frac{\omega}{\alpha})$, $\alpha = \pi f_o \sqrt{2}$, into (4.15), we have

$$A \approx \frac{\sqrt{2}}{t_o f_o \ln a_o} \int_{-\infty}^{\infty} \frac{|U(\omega)|^2}{|\omega|} d\omega. \tag{4.19}$$

Recall that $t_o := \frac{k_t}{f_o}$ and $a_o := 1 + \frac{k_\gamma}{T_s f_o}$; hence, plugging these with the Taylor series approximation $\ln a_o \approx a_o - 1$ into (4.19) gives

$$A \approx \frac{\sqrt{2} T_s f_o}{k_t k_\gamma} \int_{-\infty}^{\infty} \frac{|U(\omega)|^2}{|\omega|} d\omega. \tag{4.20}$$

The expression (4.20) shows that the redundancy is directly proportional to the time-bandwidth product. Frame redundancy indicates the granularity of the expansion; if

a frame is highly redundant, then it can finely resolve signal features while using few basis functions. In our case, we want a highly redundant frame in order to resolve, with few basis functions, between slight dilation differences in the received multipath. A closer look at the connection between frame redundancy and scale resolution is an interesting line of future research.

$k_\tau := t_o f_o$	A	B	B/A
.1	7.3662	7.9814	1.0835
.2	3.6768	3.9970	1.0871
.3	1.4726	3.6432	2.4739
.34	0.0250	4.2600	16.7684

Table 4.1: Frame bounds for $a_o = 2$.

$k_\tau := t_o f_o$	A	B	B/A
.1	343.0828	343.0828	1.0000
.2	171.3491	171.7337	1.0022
.3	77.0038	151.7181	1.9703
.35	13.0300	183.0153	14.0435

Table 4.2: Frame bounds for $a_o = 1 + 1/64$.

$k_\tau := t_o f_o$	A	B	B/A
.1	682.8513	682.8714	1.0000
.2	341.0425	341.8188	1.0023
.3	153.1917	302.0492	1.9717
.35	25.7773	364.4292	14.1376

Table 4.3: Frame bounds for $a_o = 1 + 1/128$.

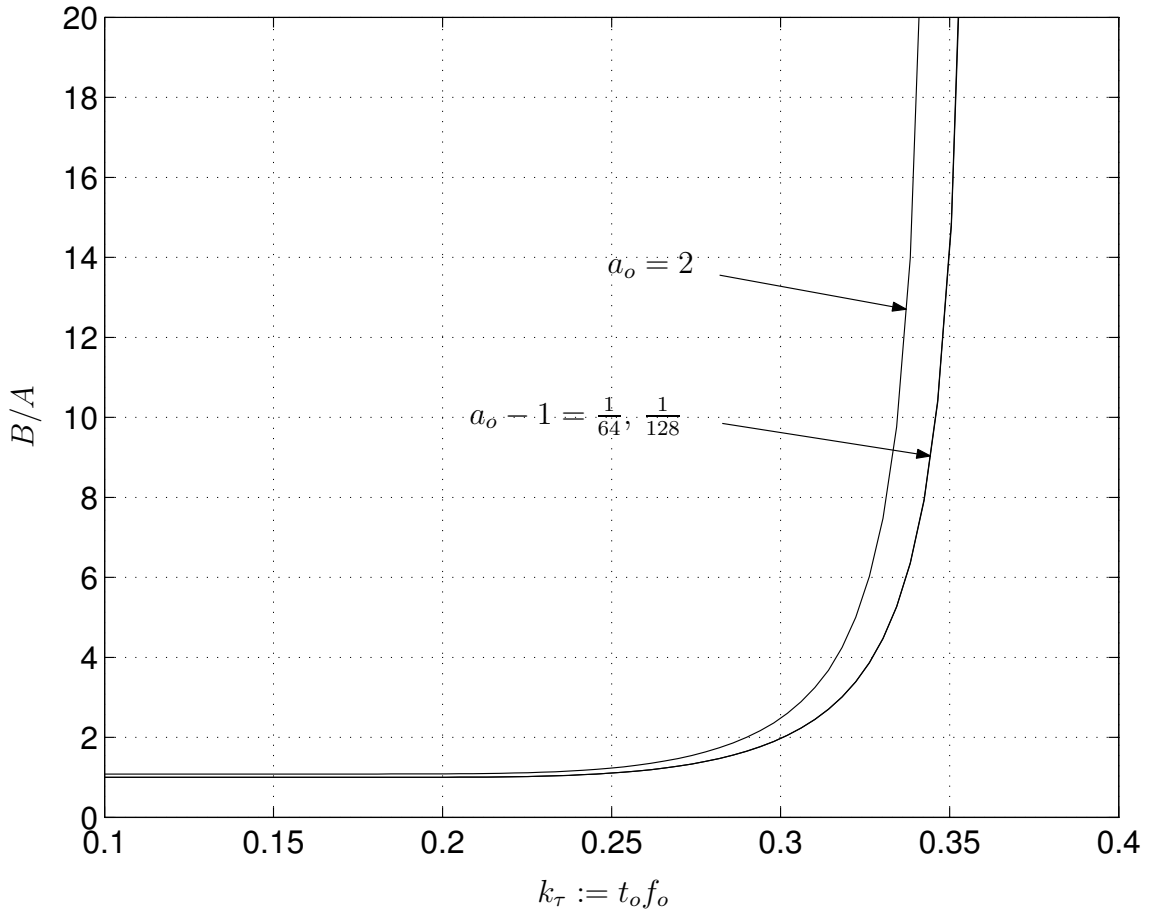

Figure 4.1: Ratio of average frame bounds B/A for a DSSS signal employing second-derivative Gaussian wavelet chip pulses.

CHAPTER 5

SCALE-LAG DIVERSITY

To determine the diversity[10] extracted by the coherent scale-lag Rake receiver, we derive the second-order statistics of the wideband channel kernel $\mathcal{L}(a,\tau)$ and use this information to compute correlation between the channel coefficients. The count of large eigenvalues of the combining coefficient autocorrelation matrix will be used to define the effective diversity level extracted by the receiver, as outlined in Section 2.3.1. The effective diversity level is the slope of the BER curve at a nominal value of SNR. We plot and compare the performances of the scale-lag Rake, Doppler-lag Rake, and conventional lag-only Rake receivers.

5.1 Wideband Scattering Function

In this section, we compute the second-order wideband channel statistics $\mathrm{E}[\mathcal{L}(a,\tau)\mathcal{L}(a',\tau')]$ assuming that the wideband channel kernel can be modeled as a sum of discrete paths. If we assume uncorrelated scattering, then we find that the second-order statistics are $\mathrm{E}[\mathcal{L}(a,\tau)\mathcal{L}(a',\tau')] = \Psi(a,\tau)\delta(a-a')\delta(\tau-\tau')$, where

[10]See Section 2.3.1 for a discussion on channel diversity.

$\Psi(a,\tau)$ is the *wideband scattering function*. The wideband scattering function quantifies the scale-lag energy spread of the wideband channel and is used in the sequel to examine the performance of the scale-lag Rake receiver.

Assume the wideband channel kernel can be modeled as a sum of N discrete paths:

$$\mathcal{L}(a,\tau) \;=\; \sum_{n=0}^{N-1} l_n \delta(a-a_n)\delta(\tau-\tau_n), \tag{5.1}$$

where $\delta(\cdot)$ is the Dirac delta function and where the n^{th} path has real-valued gain l_n, dilation a_n, and lag τ_n. A similar assumption is used to derive the channel autocorrelation function in the narrowband setting [90].

In order to proceed with the derivation, we make the following assumptions on the statistics of the wideband kernel:

(A1) The path parameters $\{l_n\}$, $\{a_n\}$, and $\{\tau_n\}$ are i.i.d. across paths with joint density $p_{A,L,\mathcal{T}}(\cdot,\cdot,\cdot)$.

(A2) The path amplitudes are zero mean, i.e., $\mathrm{E}[l_n] = 0$.

(A3) The dilation a_n is independent of the amplitude l_n and lag τ_n, i.e., $p_{A,L,\mathcal{T}}(\cdot,\cdot,\cdot) = p_A(\cdot)p_{L,\mathcal{T}}(\cdot,\cdot)$.

The amplitude and lag are often correlated in wireless communications channels where propagation losses manifest as an exponentially decaying function of increasing lag [93], [75].

From assumptions (A1) and (A2) we write

$$\mathrm{E}[\mathcal{L}(a',\tau')\mathcal{L}(a'',\tau'')] \;=\; \mathrm{E}[\delta(a'-a_0)\delta(a''-a_0)N|l_0|^2\delta(\tau'-\tau_0)\delta(\tau''-\tau_0)]. \tag{5.2}$$

Assumption (A1) allows us to consider the first path without loss of generality. From assumption (A3),

$$\begin{aligned} &\mathrm{E}[\delta(a'-a_0)\delta(a''-a_0)] \\ &= \int \delta(a'-a)\delta(a''-a)p_A(a)da, \\ &= p_A(a')\delta(a'-a''), \end{aligned} \tag{5.3}$$

and

$$\begin{aligned} &\mathrm{E}[N|l_0|^2\delta(\tau'-\tau_0)\delta(\tau''-\tau_0)] \\ &= N\iint |l|^2\delta(\tau'-\tau)\delta(\tau''-\tau)p_{L,\mathcal{T}}(l,\tau)d\tau dl, \\ &= f_{\mathcal{T}}(\tau')\delta(\tau'-\tau''), \end{aligned} \tag{5.4}$$

where we define

$$f_{\mathcal{T}}(\tau) := Np_{\mathcal{T}}(\tau)\int |l|^2 p_{L|\mathcal{T}}(l|\tau)dl. \tag{5.5}$$

The function $f_{\mathcal{T}}(\tau)$ is the *delay profile* as a function of lag τ. Thus, a decaying energy profile can be modeled.

We substitute (5.3) and (5.4) into (5.2) to obtain

$$\mathrm{E}[\mathcal{L}(a,\tau)\mathcal{L}(a',\tau')] = \underbrace{p_A(a)f_{\mathcal{T}}(\tau)}_{:=\Psi(a,\tau)}\delta(a-a')\delta(\tau-\tau'), \tag{5.6}$$

where $\Psi(a,\tau)$ is the wideband scattering function, which quantifies the distribution of received power as a function of dilation and delay.

Ring of Scatterers

Now that the form of the wideband scattering function has been determined, we investigate the dilation density $p_A(\cdot)$. An often studied channel geometry is a fixed

transmitter and dense ring of scatterers surrounding the mobile receiver. In this case, the relation between the angle-of-arrival relative to the direction of travel ξ and dilation a is

$$a \;=\; 1 - \gamma_{max}\cos(\xi). \tag{5.7}$$

where $\gamma_{max} = \frac{v_{max}}{c}$ is the scale-spread. Given the angle of arrival distribution $p_{\Xi}(\cdot)$, it is a simple matter to compute the dilation distribution $p_A(\cdot)$,

$$p_A(a) = \frac{1}{\gamma_{max}} p_Y\left(-\frac{a-1}{\gamma_{max}}\right), \tag{5.8}$$

where $Y = \cos(\Xi)$ and

$$p_Y(y) = \frac{p_{\Xi}(\cos^{-1}(y)) + p_{\Xi}(-\cos^{-1}(y))}{\sqrt{1-y^2}}. \tag{5.9}$$

If the angle of arrival ξ is distributed uniformly on $(-\pi, \pi]$, then we have

$$p_Y(y) = \frac{1}{\pi\sqrt{1-y^2}}, \quad |y| < 1, \tag{5.10}$$

which is a familiar "bathtub shape" [40] (see Fig. B.1). We call the function $p_A(a)$ the *scale profile*, analogous to the Doppler spectrum in narrowband baseband-equivalent systems.

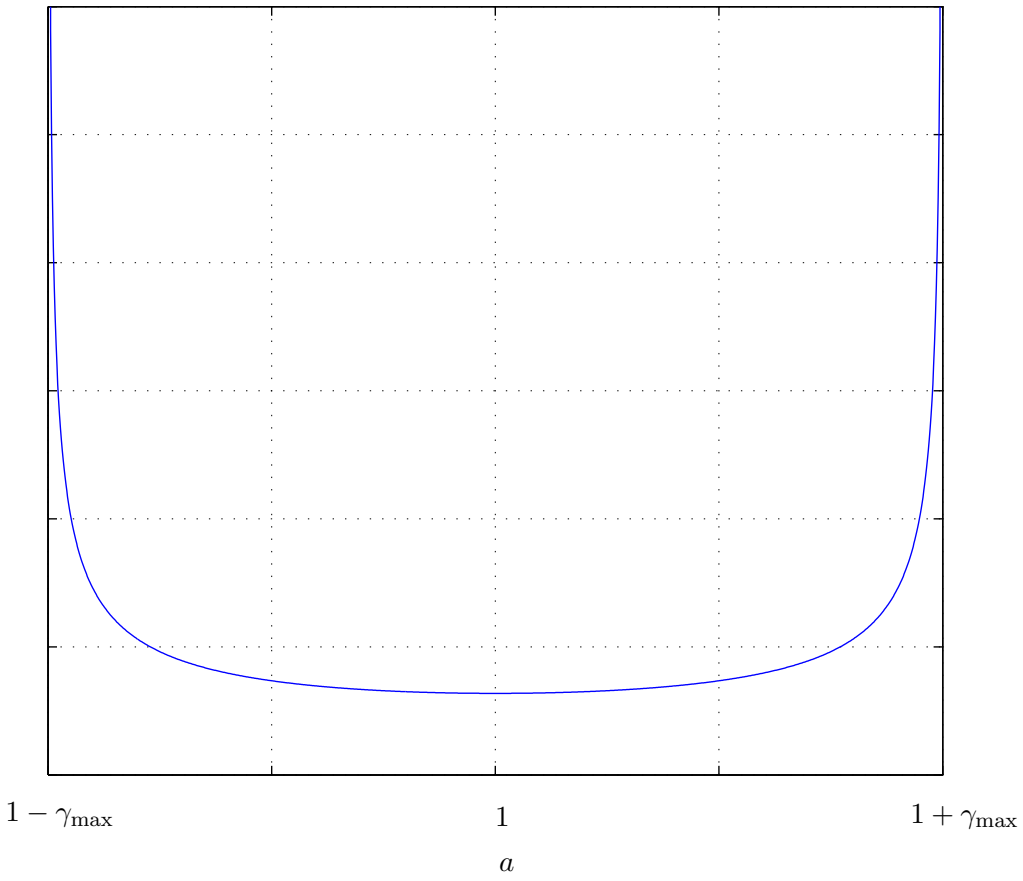

Figure 5.1: Plot of "bathtub-shaped" scale profile $p_A(a)$. The angle of arrival ξ is uniformly distributed.

5.2 Wideband Channel Coefficient Correlation

Recall from Section 2.3.1 that the BER performance of the scale-lag Rake receiver is dependent on the statistics of the channel coefficients $\{h_{m,n}^{(k)}\}$ (c.f. (3.11)). In the following, we compute $\mathrm{E}[h_{m,n}^{(k)} h_{m',n'}^{(k')}]$, which is the general correlation between the channel coefficients, and use this result to determine the diversity exploited by the scale-lag Rake.

$$\begin{aligned}
&\mathrm{E}[h_{m,n}^{(k)} h_{m',n'}^{(k')}] = \\
&\quad \int_0^{\tau_{\max}} \int_{1-\gamma_{\max}}^{1+\gamma_{\max}} \Psi(a,\tau) \\
&\quad \mathrm{E}\left[\chi\left(\frac{a_o^m}{a}, \frac{nT_o a_o^m - \tau - k(a-1)T_s}{a}\right)\chi\left(\frac{a_o^{m'}}{a}, \frac{n'T_o a_o^{m'} - \tau - k'(a-1)T_s}{a}\right)\right] da d\tau, \\
\approx &\quad \int_0^{\tau_{\max}} \int_{1-\gamma_{\max}}^{1+\gamma_{\max}} \Psi(a,\tau) \\
&\quad \bar{\chi}\left(\frac{a_o^m}{a}, \frac{nT_o a_o^m - \tau - k(a-1)T_s}{a}\right)\bar{\chi}\left(\frac{a_o^{m'}}{a}, \frac{n'T_o a_o^{m'} - \tau - k'(a-1)T_s}{a}\right) da d\tau,
\end{aligned} \tag{5.11}$$

where $\Psi(a,\tau)$ is the wideband scattering function defined in the previous section, $\chi(a,\tau)$ is the wideband ambiguity function defined in (3.1), and $\bar{\chi}(a,\tau)$ is defined in (3.5) as the mean-square approximation of $\chi(a,\tau)$. We have also used Lemma 4 of Appendix 3.4, which states $\mathrm{E}[\chi(a,\tau)\chi(a',\tau')] \approx \bar{\chi}(a,\tau)\bar{\chi}(a',\tau')$. The approximation (5.11) is tight since we assume that a and a' are near unity and the number of chips N_p is large. After making the approximations[11] $\frac{a_o^m}{a} \approx 1 + m\gamma_o - (a-1)$ and $\frac{nT_o a_o^m - \tau - i(a-1)T_s}{a} \approx nT_o - \tau - i(a-1)T_s$, we have that the correlation (5.11) can be

[11] Note that $a_o^m \approx 1 + m\gamma_o$, and $1/a \approx 1 - (a-1)$.

approximated[12] by

$$\begin{aligned}
&\mathrm{E}[h^{(k)}_{m,n}h^{(k')}_{m',n'}] \approx \\
&\quad \int_0^{\tau_{\max}} \int_{1-\gamma_{\max}}^{1+\gamma_{\max}} \Psi(a,\tau)\bar{\chi}\left(1+m\gamma_o-(a-1), nt_o-\tau-k(a-1)T_s\right) \\
&\quad \bar{\chi}\left(1+m'\gamma_o-(a-1), n't_o-\tau-k'(a-1)T_s\right) da d\tau. \qquad (5.12)
\end{aligned}$$

Finally, we insert the relations $t_o = \frac{k_\tau}{f_o}$ and $\gamma_o = \frac{k_\gamma}{T_s f_o}$ from Section 3.1 and make the variable substitutions $\bar{\gamma} := (a-1)T_s f_o$ and $\bar{\tau} := \tau f_o$ to obtain

$$\begin{aligned}
\mathrm{E}[h^{(k)}_{m,n}h^{(k')}_{m',n'}] \;&\approx\; \frac{1}{T_s f_o^2}\int_0^{\tau_{\max}f_o}\int_{-\gamma_{\max}T_s f_o}^{\gamma_{\max}T_s f_o} \Psi(1+\tfrac{\bar{\gamma}}{T_s f_o}, \tfrac{\bar{\tau}}{f_o}) \\
&\qquad \bar{\chi}\left(1+\frac{mk_\gamma-\bar{\gamma}}{T_s f_o}, \frac{nk_t-\bar{\tau}-k\bar{\gamma}}{f_o}\right) \\
&\qquad \bar{\chi}\left(1+\frac{m'k_\gamma-\bar{\gamma}}{T_s f_o}, \frac{n'k_t-\bar{\tau}-k'\bar{\gamma}}{f_o}\right) d\bar{\gamma}d\bar{\tau}. \\
&= \frac{1}{T_s f_o^2}\int_0^{\tau_{\max}f_o}\int_{-\gamma_{\max}T_s f_o}^{\gamma_{\max}T_s f_o} \Psi(1+\tfrac{\bar{\gamma}}{T_s f_o}, \tfrac{\bar{\tau}}{f_o}) \\
&\qquad \int_0^1 \chi_p\left(1, \frac{nk_t-\bar{\tau}+(mk_\gamma-\bar{\gamma})z-k\bar{\gamma}}{f_o}\right) dz \\
&\qquad \int_0^1 \chi_p\left(1, \frac{n'k_t-\bar{\tau}+(m'k_\gamma-\bar{\gamma})z'-k'\bar{\gamma}}{f_o}\right) dz' d\bar{\gamma}d\bar{\tau}. \qquad (5.13)
\end{aligned}$$

where we have used the definition $\bar{\chi}(a,\tau) := \int_0^1 \chi_p(1, \tau+(a-1)zT_s)dz$ (c.f. (3.5)). The variable $\bar{\gamma}$ is the scale deviation normalized by the time-bandwidth product, and $\bar{\tau}$ is lag normalized to bandwidth.

5.3 Numerical Results

In this section, we examine the performance a DSSS system employing a unit-energy second-derivative Gaussian chip pulse (c.f. (3.3)). As in Section 2.3.1, we

[12]This approximation is not valid for systems where mobility is large relative to the speed of wave propagation, e.g., high-speed underwater applications.

assume that the receiver is demodulating the 0^{th} bit and hence drop the bit index k, i.e., set $k = k' = 0$; the results pertain to any other bit in a bit-by-bit detector. We plug the expression for the ambiguity function of the second-derivative Gaussian chip pulse (3.34) into the correlation (5.13) to compute the channel correlation matrix $\mathrm{E}[\boldsymbol{h}\boldsymbol{h}^T] = \boldsymbol{R}_h$, where $\boldsymbol{h}$ is defined in Section 3.2. It is then straightforward to compute $\boldsymbol{\Sigma} = \boldsymbol{R}_{\boldsymbol{x}}^{-T/2}\boldsymbol{R}_{\boldsymbol{h}}\boldsymbol{R}_{\boldsymbol{x}}^{-1/2}$, the autocorrelation matrix of the whitened matched-filter combining coefficients $\boldsymbol{f}$, where $\boldsymbol{f}$ and $\boldsymbol{R}_{\boldsymbol{x}}$ are defined in Section 2.3 (using the scale-lag basis). The numerical analysis is performed by evaluating (5.13) on a grid of size 41×41 over the variables $(\bar{\gamma}, \bar{\tau})$ and using the MATLAB command trapz for numerical integration.

From (5.13), we see how the results are dependent on the relation parameters k_τ and k_γ. Recall from Section 3.1 that k_τ and k_γ relate the translation-spacing t_o and scale-spacing γ_o to the time and bandwidth in the following manner: $t_o = \frac{k_\tau}{f_o}$ and $\gamma_o = \frac{k_\gamma}{T_s f_o}$. If $k_\tau = 0.236$ then the translation spacing is set to the *minimum resolvable lag* and if $k_\gamma = 0.55$ then the scale spacing is set to the *minimum scale resolution*. See Section 3.1 for a discussion of scale and lag resolution.

The final assumption is that the wideband channel kernel $\mathcal{L}(a, \tau)$ is a real-valued, zero-mean, uncorrelated, Gaussian process with unit energy, i.e.,

$$\int\int \Psi(a, \tau) da d\tau = 1. \tag{5.14}$$

Hence, the BER analysis and effective diversity level definition of Section 2.3.1 apply.

Figures 5.2 - 5.5 study the scale-lag Rake for various choices of k_γ and k_τ, and figures 5.6 - 5.9 compare performances of the scale-lag Rake, Doppler-lag Rake and

conventional lag-only rake. See Appendix A for details regarding the setup of the Doppler-lag Rake, which is a real-valued extension of the Doppler-lag Rake in [85]. The conventional lag-only Rake (2.38) collects energy from only the $m = 0$ fingers, i.e., it collects only lag diversity. The bit error rate (BER) is computed with (2.50), where the SNR is $\frac{E_b}{\sigma_w^2}$, i.e., the *transmitted* SNR. For all the plots, the system assumes a delay spread of $\tau_{max} = 0.5/f_o$ seconds and a uniform delay profile $f_{\mathcal{T}}(\tau)$. Furthermore, the scale profile $p_A(a)$ is assumed to have a "bathtub" shape as specified in Section 5.1. We choose $M = \lceil \gamma_{max} T_s f_o \rceil + 1$ and $N = \lceil \tau_{max} f_o \rceil + 1$ to capture a significant portion of the received energy in the channel coefficients.

As discussed in Section 4.3, the frame status of the scale-lag Rake is not sensitive to the choice of scale-spacing parameter γ_o, or equivalently of the relation $k_\gamma = \gamma_o T_s f_o$; however, it was seen that γ_o affects significantly the frame redundancy, that is, the granularity of the frame. In Fig. 5.2(a), the translation spacing relation is set to the minimum resolvable lag ($k_\tau = 0.236$), such that the scale-lag Rake is a snug frame. In this case, the projection coefficients are sufficient statistics since they capture all the information in the signal space. Notice that the performance is affected very little by the choice of k_γ (scale-spacing). In Fig. 5.2(b)-(c), the translation spacing relation k_τ is set to 0.744 and 2, respectively, such that the scale-lag Rake is not a frame. The overall performance is worse than (a) because the statistics are insufficient, but a tighter scale spacing (e.g., $k_\gamma = 0.55$, set to the minimum scale resolution) mitigates the loss of performance by capturing energy in the dilated multipath components. In Fig. 5.2, the normalized scale spread is $\gamma_{max} T_s f_o = 0.05$; Figure 5.3 repeats the preceding observations for the scale spread of $\gamma_{max} T_s f_o = 0.0005$.

Figure 5.4 and Figure 5.5 illustrate the performance loss when the translation-spacing relation k_τ is chosen too large. The subplots are indexed by scale-spacing relation k_γ and the curves are indexed by translation-spacing relation k_τ. Once again, we see that the performance loss due to choosing a wider translation-spacing is minimized when the scale-spacing relation is set to the minimum scale resolution ($k_\gamma = 0.55$). In Fig. 5.4 and Fig. 5.5, the normalized scale spread is $\gamma_{max} T_s f_o = 0.05$ and 0.0005, respectively.

In Figures 5.6 - 5.7 we compare the performances of the scale-lag Rake, Doppler-lag Rake and conventional lag-only Rake. For a fair comparison, the scale-lag Rake and Doppler-lag Rake have the same number of Rake fingers: $(2M + 1)(N + 1)$. See Section 2.4.2 for a discussion on the choice of M and N. The lag-only rake has $N + 1$ fingers. When the the translation-spacing parameter of the Rakes is set to the minimum resolvable lag, then the Rakes have nearly the same performance, as shown in Fig. 5.6. We offer the following explanation for this similarity. The reduced complexity Rake analysis of Section 3.2.1 shows that the translation-spacing parameter can be thought of as the sampling period of the Rake receiver. The sampling period is slightly lengthened or shortened to obtain the scale components of the scale-lag Rake receiver. If the sampling period is short enough such that the sampling frequency satisfies the Nyquist sampling criterion, then the lag components are sufficient statistics and additional components do not provide additional information. The single-sided bandwidth of the second-derivative Gaussian chip pulse is roughly $W = 2f_o$ (see Fig. 3.2); hence, the Nyquist sampling criterion is approximately satisfied for a translation-spacing parameter t_o of $12W = 0.25 f_o$. If the translation

spacing parameter t_o is set to the minimum resolvable lag $\tau_o = \frac{0.236}{f_o}$, then Nyquist is approximately satisfied and additional scale or Doppler components provide little additional information at the operational SNR's.

On the other hand, if the translation-spacing is such that Nyquist sampling is not satisfied, as in Fig. 5.7 where $k_\tau = 2$, i.e., $t_o = \frac{2}{f_o}$, then the scale-lag Rake outperforms both the Doppler-lag Rake and lag-only Rake. We reason that scale-lag Rake is more closely matched to the scale-lag spreading of the wideband channel.

Figures 5.8 - 5.9 are similar to the previous two figures, however, the performances of the Rake receivers are now separated into subplots for self comparison: (a) scale-lag Rake, (b) Doppler-lag Rake, and (c) lag-only Rake. The Eigenvalue curves are indexed from right to left over normalized scale spreads of $\gamma_{\max} T_s f_o = 0.05,\ 0.005,$ and 0.0005. Figure 5.8 has translation spacing relation set to $k_\tau = 0.236$ (minimum resolvable lag) and Fig. 5.9 has translation spacing relation set to $k_\tau = 2$.

For reference, a normalized scale spread of 0.005 would be found in an RF system with mobile velocity of 10 km/hr, data rate of 1 Mbps, and bandwidth of 10 GHz, or in an RF system with velocity of 100 km/hr, data rate of 1 Mbps, and bandwidth of 1 GHz. A normalized scale spread of 0.05 would be found in an underwater acoustic telemetry system with mobile velocity of 1 km/hr, data rate of 1 kbps, and bandwidth of 50 kHz.

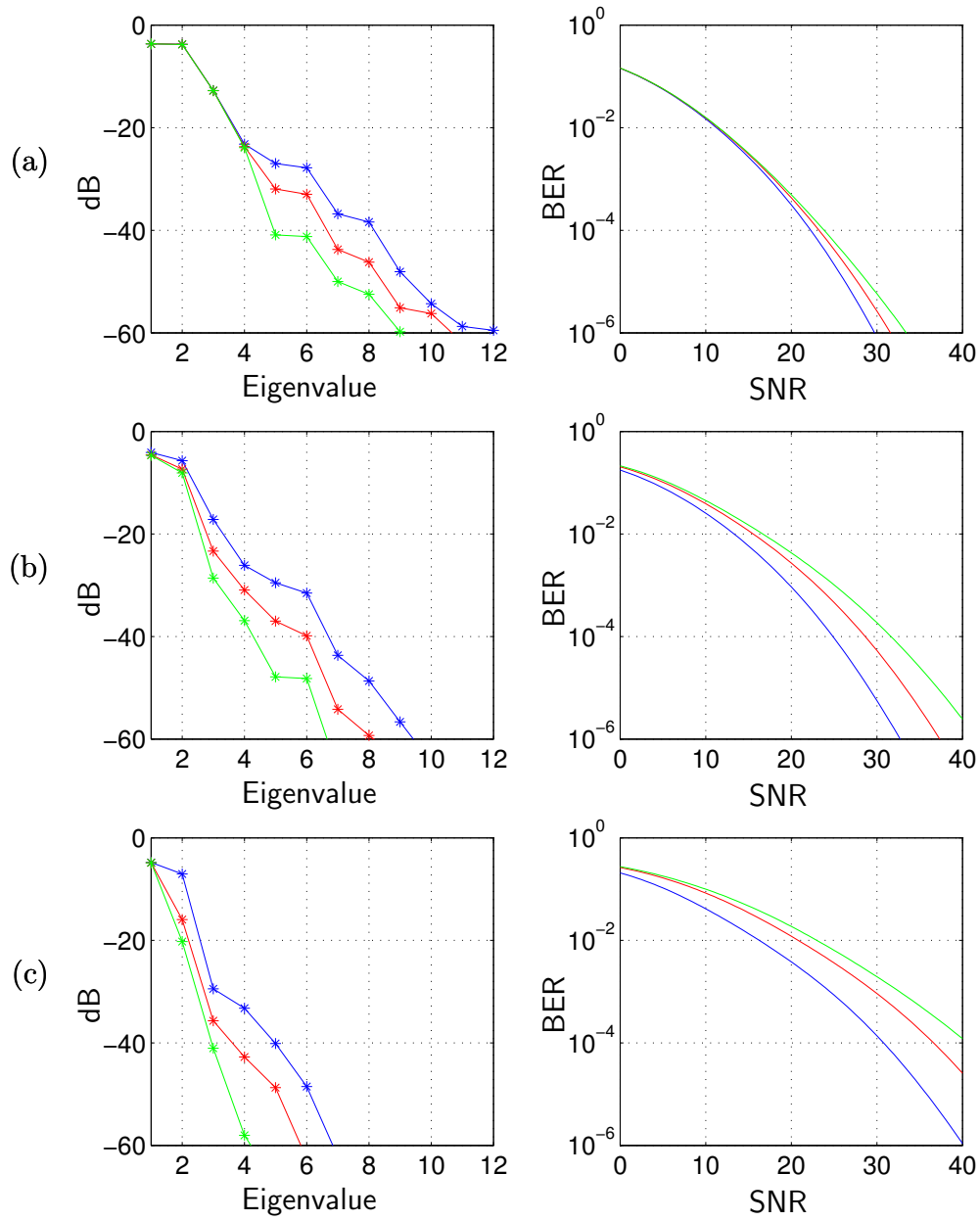

Figure 5.2: For the scale-spread of $\gamma_{max} T_s f_o = 0.05$, we compare the eigenvalues and BER of the scale-lag Rake receiver for translation-spacing relation k_τ settings of (a) $k_\tau = 0.236$ (minimum resolvable lag), (b) $k_\tau = 0.744$, (c) $k_\tau = 2$. The Eigenvalue curves are indexed from right to left over scale-spacings of $k_\gamma = 0.55$ (minimum scale resolution), $k_\gamma = 1$, and $k_\gamma = 2$. The BER curves are indexed in the opposite ordering. The normalized delay spread is $\tau_{max} f_o = 0.5$. A "bathtub-shaped" scale profile (5.10) is used.

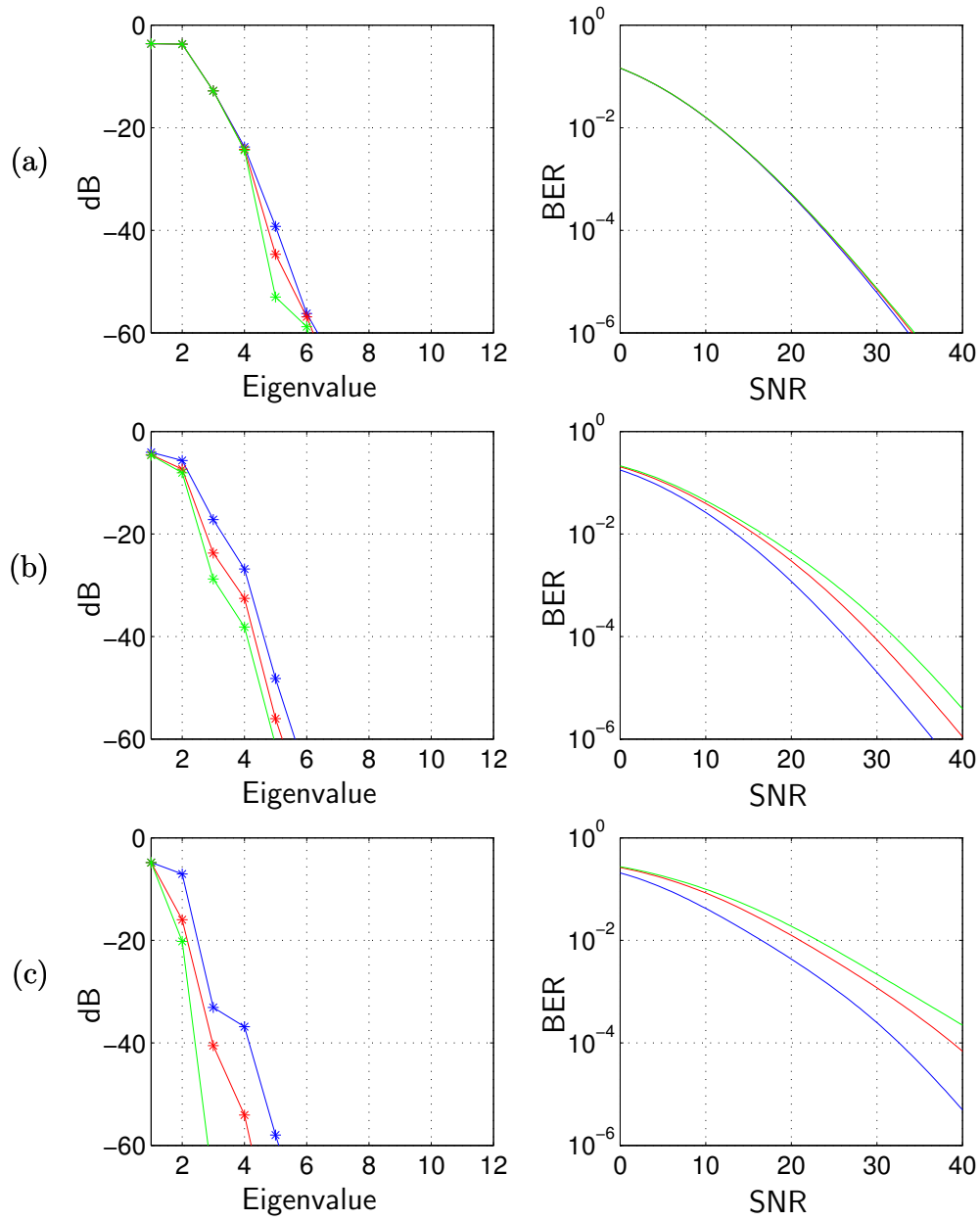

Figure 5.3: For the scale-spread of $\gamma_{max} T_s f_o = 0.0005$, we compare the eigenvalues and BER of the scale-lag Rake receiver for translation-spacing relation k_τ settings of (a) $k_\tau = 0.236$ (minimum resolvable lag), (b) $k_\tau = 0.744$, (c) $k_\tau = 2$. The Eigenvalue curves are indexed from right to left over scale-spacings of $k_\gamma = 0.55$ (minimum scale resolution), $k_\gamma = 1$, and $k_\gamma = 2$. The BER curves are indexed in the opposite ordering. The normalized delay spread is $\tau_{max} f_o = 0.5$. A "bathtub-shaped" scale profile (5.10) is used.

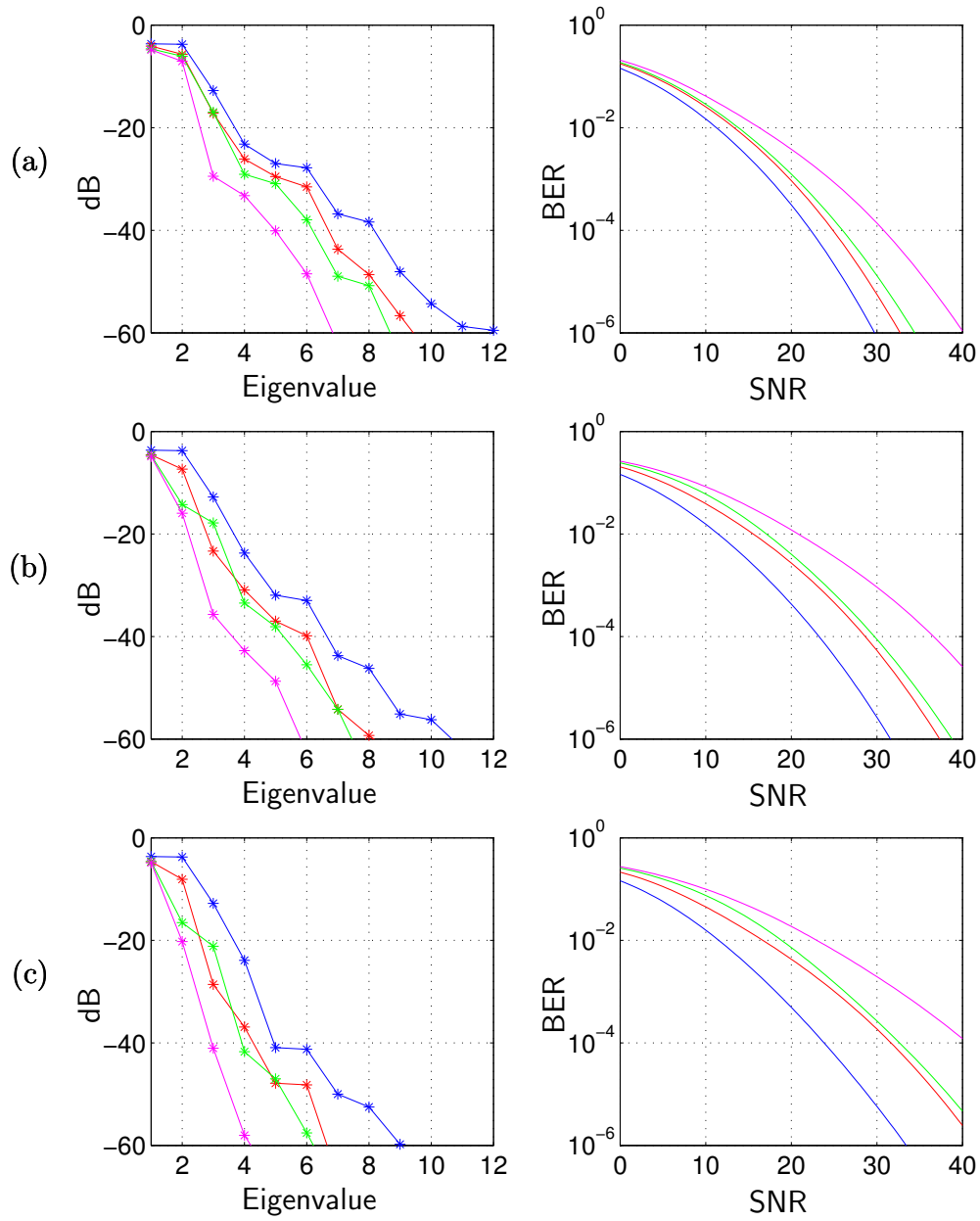

Figure 5.4: For the scale-spread of $\gamma_{max} T_s f_o = 0.05$, we compare the eigenvalues and BER of the scale-lag Rake receiver for scale-spacing relation k_γ settings of (a) $k_\gamma = 0.55$ (minimum scale resolution), (b) $k_\gamma = 1$, (c) $k_\gamma = 2$. The Eigenvalue curves are indexed from right to left over translation-spacings of $k_\tau = 0.236$ (minimum resolvable lag), $k_\tau = 0.744$, $k_\tau = 1$ and $k_\tau = 2$. The BER curves are indexed in the opposite ordering. The normalized delay spread is $\tau_{max} f_o = 0.5$. A "bathtub-shaped" scale profile (5.10) is used.

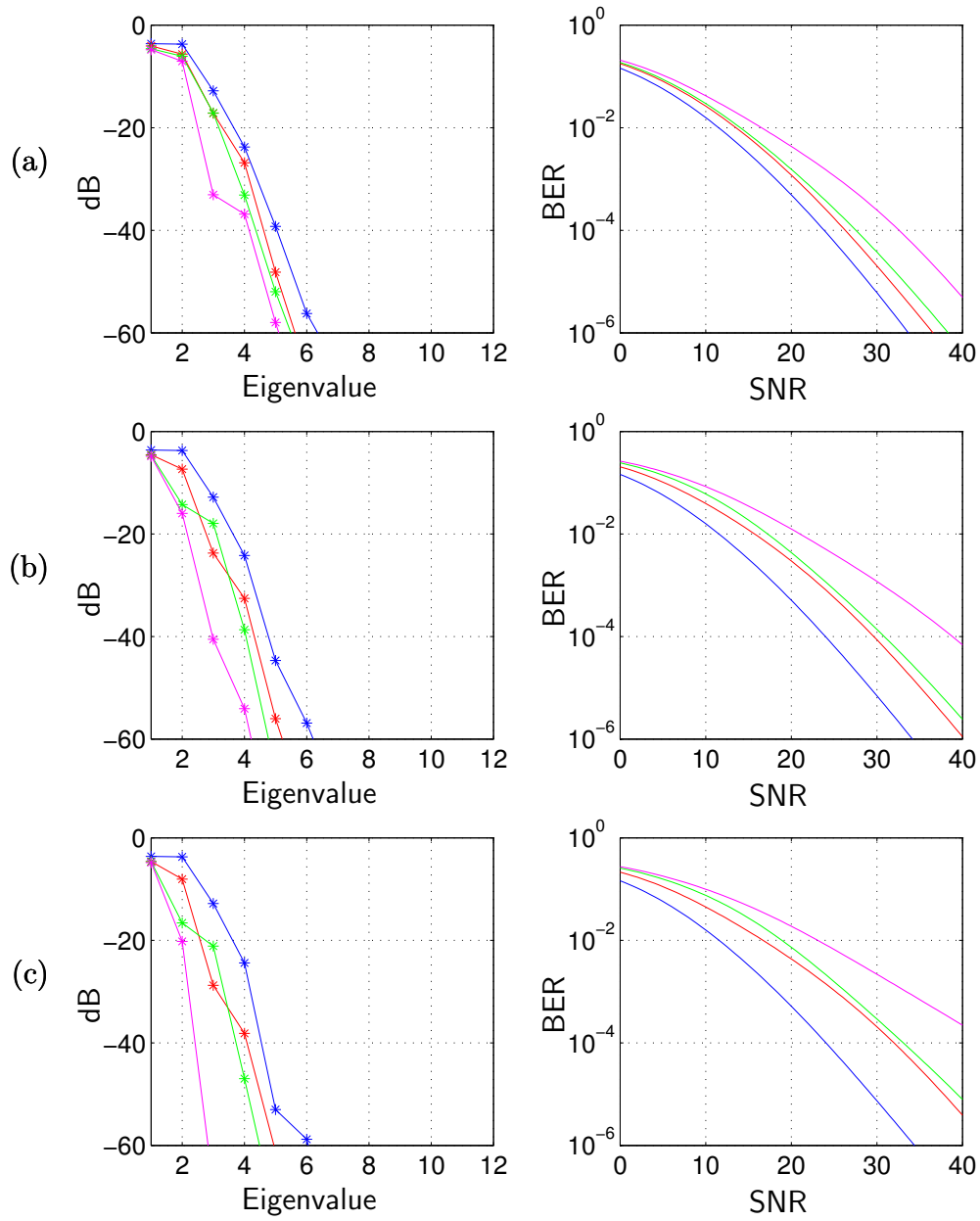

Figure 5.5: For the scale-spread of $\gamma_{max} T_s f_o = 0.0005$, we compare the eigenvalues and BER of the scale-lag Rake receiver for scale-spacing relation k_γ settings of (a) $k_\gamma = 0.55$ (minimum scale resolution), (b) $k_\gamma = 1$, (c) $k_\gamma = 2$. The Eigenvalue curves are indexed from right to left over translation-spacings of $k_\tau = 0.236$ (minimum resolvable lag), $k_\tau = 0.744$, $k_\tau = 1$ and $k_\tau = 2$. The BER curves are indexed in the opposite ordering. The normalized delay spread is $\tau_{max} f_o = 0.5$. A "bathtub-shaped" scale profile (5.10) is used.

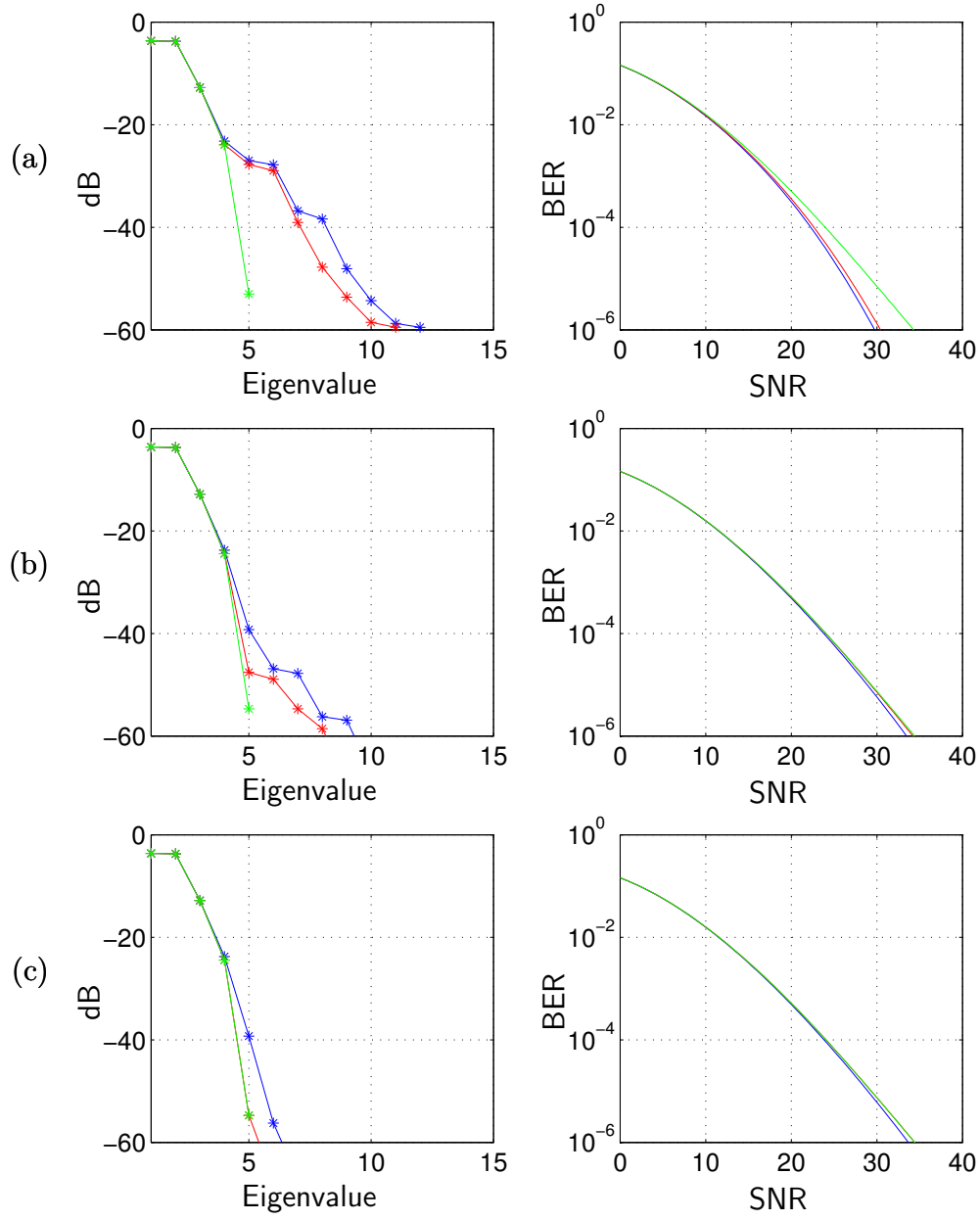

Figure 5.6: For the scale-spacing relation $k_\gamma = 0.55$ (set to minimum scale resolution) and translation-spacing relation $k_\tau = 0.236$ (set to minimum resolvable lag), we compare the eigenvalues and BER performances of the three receivers for scale-spreads of (a) $\gamma_{max} T_s f_o = 0.05$, (b) $\gamma_{max} T_s f_o = 0.005$, (c) $\gamma_{max} T_s f_o = 0.0005$. The Eigenvalue curves are indexed from right to left as the scale-lag Rake, Doppler-lag Rake, and lag-only Rake. The BER curves are indexed in the opposite ordering. The normalized delay spread is $\tau_{max} f_o = 0.5$. A "bathtub-shaped" scale profile (5.10) is used.

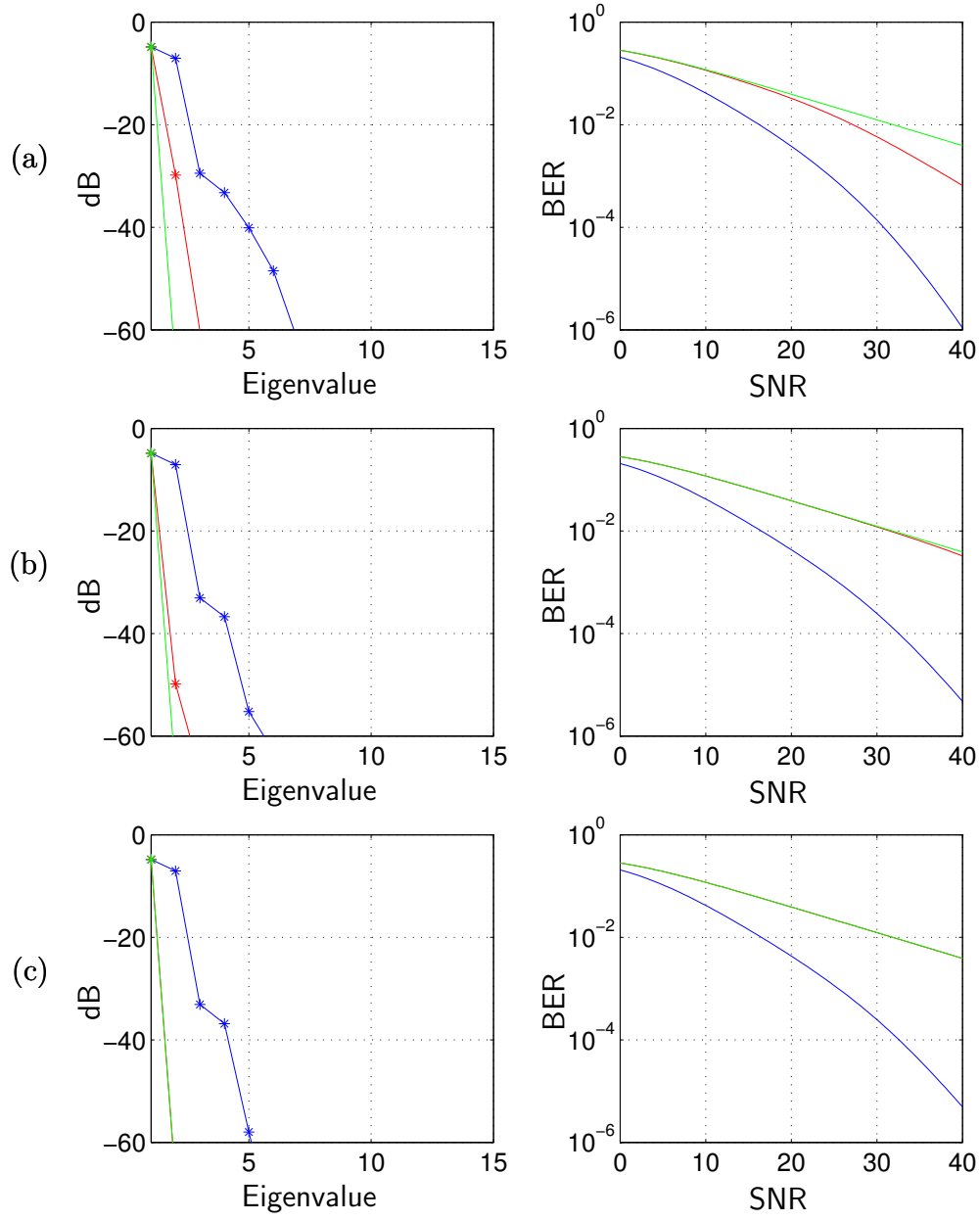

Figure 5.7: For the scale-spacing relation $k_\gamma = 0.55$ (set to minimum scale resolution) and translation-spacing relation $k_\tau = 2$, we compare the eigenvalues and BER performances of the three receivers for scale-spreads of (a) $\gamma_{max} T_s f_o = 0.05$, (b) $\gamma_{max} T_s f_o = 0.005$, (c) $\gamma_{max} T_s f_o = 0.0005$. The Eigenvalue curves are indexed from right to left as the scale-lag Rake, Doppler-lag Rake, and lag-only Rake. The BER curves are indexed in the opposite ordering. The normalized delay spread is $\tau_{max} f_o = 0.5$. A "bathtub-shaped" scale profile (5.10) is used.

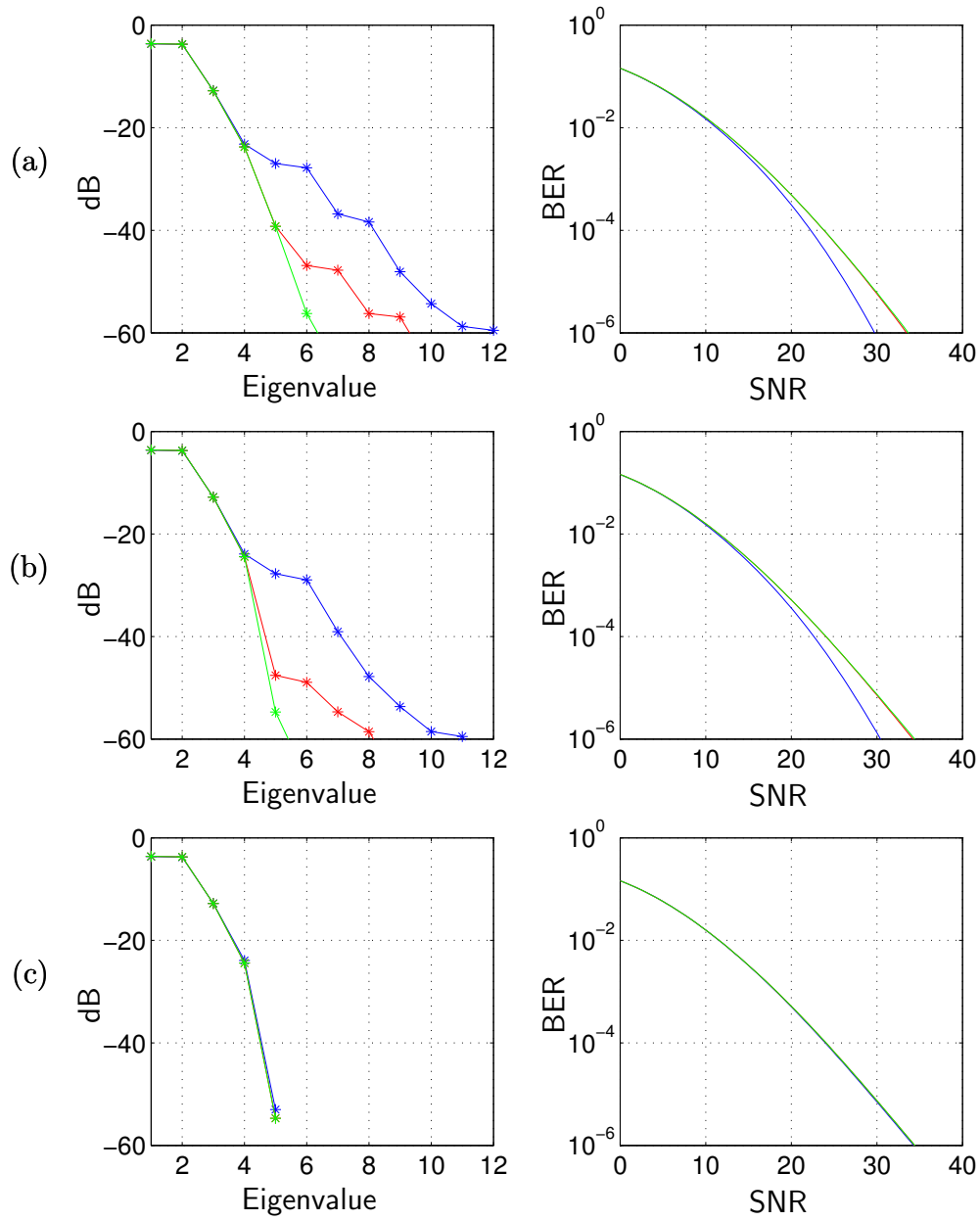

Figure 5.8: For the scale-spacing relation $k_\gamma = 0.55$ (set to minimum scale resolution) and translation-spacing relation $k_\tau = 0.236$ (set to minimum resolvable lag), we show the eigenvalues and BER for (a) scale-lag Rake, (b) Doppler-lag Rake, and (c) lag-only Rake. The Eigenvalue curves are indexed from right to left via the normalized scale spread $\gamma_{max} T_s f_o = 0.05, 0.005, 0.0005$, respectively. The BER curves are indexed in the opposite ordering. The normalized delay spread is $\tau_{max} f_o = 0.5$. A "bathtub-shaped" scale profile (5.10) is used.

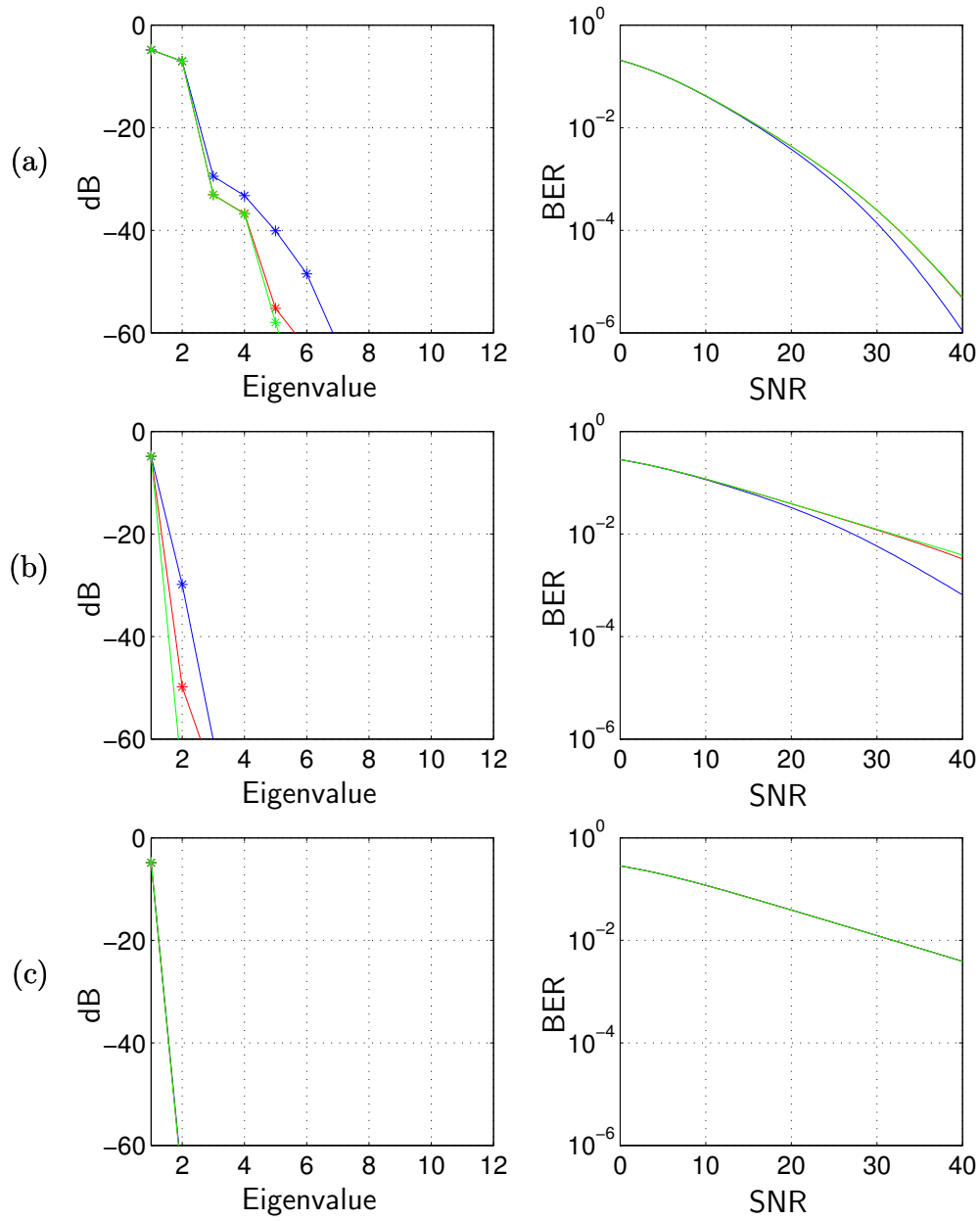

Figure 5.9: For the scale-spacing relation $k_\gamma = 0.55$ (set to minimum scale resolution) and translation-spacing relation $k_\tau = 2.0$, we show the eigenvalues and BER for (a) scale-lag Rake, (b) Doppler-lag Rake, and (c) lag-only Rake. The Eigenvalue curves are indexed from right to left via the normalized scale spread $\gamma_{max} T_s f_o = 0.05,\ 0.005,\ 0.0005$, respectively. The BER curves are indexed in the opposite ordering. The normalized delay spread is $\tau_{max} f_o = 0.5$. A "bathtub-shaped" scale profile (5.10) is used.

CHAPTER 6

RAKE RECEIVER FINGER CORRELATION STRUCTURE

Up to this point, we have considered each bit in isolation and assumed that the receiver has perfect knowledge of the wideband channel coefficients $\{h_{m,n}^{(k)}\}$. In a real system, these receiver parameters must be estimated and tracked for coherent reception. In this chapter, we make a preliminary study the time variations of the channel coefficients and find that the time-variability is proportional to the scale spread in wideband channels, just as the time-variability is proportional to the Doppler spread for narrowband baseband-equivalent channels.

We begin by studying the autocorrelation between channel coefficients of a Doppler-lag receiver [85] operating in a narrowband baseband-equivalent system. The channel coefficients are found to evolve according to Jakes model [40] for a ring of scatterers model. We then investigate the wideband system and determine that the channel coefficients are approximately stationary over short periods of time. Since the number of significant eigenmodes is small compared to the full system dimension, we study the effect of using principal components combining (PCC) [2] to generate bit decisions. Finally, we perform physical experiments in the acoustic domain to validate

the theoretical wideband correlation sequence and show the validity of the wideband channel model for modelling real-world channels.

6.1 Narrowband Baseband-Equivalent Model

Let us for a moment return to the narrowband baseband-equivalent model and examine the time-series autocorrelation of the Doppler-lag Rake finger channel coefficients. We take an approach similar to the approach we will take for the wideband case, in that we project the baseband received signal onto the (complex-valued) Doppler-lag basis [85] and compute the correlation of the channel coefficients across time.

Recall that the narrowband baseband-equivalent received signal (2.25) is

$$\tilde{r}(t) \;=\; \int\int \tilde{H}(\theta,\tau)e^{j2\pi\theta t}\tilde{s}(t-\tau)d\theta d\tau + \tilde{w}(t).$$

If we assume uncorrelated scattering, the narrowband baseband-equivalent spreading function $\tilde{H}(\theta,\tau)$ is uncorrelated across time and frequency, i.e., the second order statistics can be written (see Appendix B)

$$\mathrm{E}[\tilde{H}(\theta,\tau)\tilde{H}(\theta',\tau')] = \tilde{S}(\theta,\tau)\delta(\theta-\theta')\delta(\tau-\tau'), \tag{6.1}$$

where $\tilde{S}(\theta,\tau)$ is the *narrowband scattering function*, which characterizes the channel power distribution across Doppler-frequency θ and lag τ. From the narrowband assumption,[13] the scattering function has finite θ-support: $\tilde{H}(\theta,\tau) = 0$ for $|\theta| > f_{\max}$, where $f_{\max}$ is the (single-sided) maximum Doppler-frequency spread (see

[13] see assumption (A0) in Section 2.2.1.

Section 2.2.1). We also have that $\tilde{H}(\theta,\tau) = 0$ for $\tau < 0$ or $\tau > \tau_{\max}$, where $\tau_{\max}$ is the delay spread.

6.1.1 Doppler-Lag Rake Receiver

The Doppler-lag Rake receiver generates sufficient statistics for the k^{th} bit by projecting the received signal $\tilde{r}(t)$ onto the Doppler-lag basis functions

$$\tilde{x}_{m,n}^{(k)}(t) \;:=\; \tilde{x}(t - n\tilde{t}_o - kT_s)e^{j\frac{2\pi mt}{T_s}}, \quad k,n,m \in \mathbb{Z}, \tag{6.2}$$

where $\tilde{x}(t)$ is the narrowband baseband-equivalent DSSS signal given by (2.1) and $\tilde{t}_o$ is the lag spacing of the Doppler-lag Rake. It is shown in [85] that this basis is approximately orthonormal for $\tilde{t}_o = \tilde{T}_o$, where $\tilde{T}_o$ is the chip spacing (see (2.1)).

6.1.2 Narrowband Channel Coefficients

The resulting narrowband baseband-equivalent projection coefficients are

$$\begin{aligned}
\tilde{r}_{m,n}^{(k)} &= \langle \tilde{x}_{m,n}^{(k)}(t), \tilde{r}(t) \rangle && (6.3)\\
&= \int \tilde{x}_{m,n}^{(k)*}(t)\tilde{r}(t)dt && (6.4)\\
&= \sum_{p=0}^{\tilde{N}_p-1} b_p \int\int \tilde{H}(\theta,\tau) \underbrace{\int \tilde{x}_{m,n}^{(k)*}(t)\tilde{x}(t-\tau-pT_s)e^{j2\pi\theta t}dt}_{\approx 0,\ \text{for } p\neq k \ \text{since } T_s \gg \tau_{\max}} d\theta d\tau + \tilde{w}_{m,n}^{(k)} && (6.5)\\
&\approx b_k \int\int \tilde{H}(\theta,\tau) \int \tilde{x}_{m,n}^{(k)*}(t)\tilde{x}(t-\tau-kT_s)e^{j2\pi\theta t}dt d\theta d\tau + \tilde{w}_{m,n}^{(k)} && (6.6)\\
&= \underbrace{b_k \int\int \tilde{H}(\theta,\tau)\tilde{\chi}\left(\theta - \frac{m}{T_s}, n\tilde{t}_o - \tau\right) e^{j2\pi(\theta\tau + fkT_s - \frac{m}{T_s}\tau)} d\theta d\tau}_{\tilde{h}_{m,n}^{(k)}} + \tilde{w}_{m,n}^{(k)} && (6.7)\\
&= b_k \tilde{h}_{m,n}^{(k)} + \tilde{w}_{m,n}^{(k)}, && (6.8)
\end{aligned}$$

where $\tilde{\chi}(\theta,\tau) := \int x(t)x(t-\tau)e^{j2\pi\theta t}dt$ is the *narrowband ambiguity function* and $\tilde{h}_{m,n}^{(k)}$ is the channel coefficient for Doppler-lag Rake finger (m,n) at bit k.

6.1.3 Narrowband Channel Correlation

We are interested in how the narrowband baseband-equivalent channel taps $\{\tilde{h}^{(k)}_{m,n}\}$ change with time, which is statistically quantified by the channel correlation $\mathrm{E}[\tilde{h}^{(k)}_{m,n}\tilde{h}^{(k+k')*}_{m',n'}]$. Using the uncorrelated scattering assumption (6.1), we write the channel correlation as

$$\mathrm{E}[\tilde{h}^{(k)}_{m,n}\tilde{h}^{(k+k')*}_{m',n'}] = \int_0^{\tau_{\max}} \int_{-f_{\max}}^{f_{\max}} \tilde{S}(\theta,\tau)\,\mathrm{E}\Big[\tilde{\chi}\left(\theta-\tfrac{m}{T_s}, n\tilde{t}_o-\tau\right) \tilde{\chi}\left(\theta-\tfrac{m'}{T_s}, n'\tilde{t}_o-\tau\right)\Big] e^{j2\pi(\theta k' T_s+\frac{m-m'}{T_s}\tau)} d\theta d\tau. \tag{6.9}$$

Note that channel coefficients form a wide-sense stationary process, that is, with fixed m, n, m', n'; the correlation (6.9) depends only on the bit-interval difference k' between channel coefficients. From the assumptions and analysis of Appendix B (specifically equation (B.6)), we observe that the narrowband scattering function can be separated into Doppler and lag profiles $S(\theta,\tau) = p_\Theta(\theta) f_\mathcal{T}(\tau)$. Furthermore, for a sufficiently smooth ambiguity function $\tilde{\chi}(\theta,\tau)$, we can assume $\tilde{\chi}\left(\theta-\frac{m}{T_s}, n\tilde{t}_o-\tau\right) \approx \chi\left(-\frac{m}{T_s}, n\tilde{t}_o-\tau\right)$, when $\theta \in [-f_{\max}, f_{\max}]$. It follows that (6.9) can be written

$$\mathrm{E}[\tilde{h}^{(k)}_{m,n}\tilde{h}^{(k+k')*}_{m',n'}] \approx \int_{-f_{\max}}^{f_{\max}} p_\Theta(\theta) e^{j2\pi\theta k' T_s} df \underbrace{\int_0^{\tau_{\max}} f_\mathcal{T}(\tau)\,\mathrm{E}\Big[\tilde{\chi}\left(-\tfrac{m}{T_s}, n\tilde{t}_o-\tau\right)\tilde{\chi}\left(-\tfrac{m'}{T_s}, n'\tilde{t}_o-\tau\right)\Big] e^{j2\pi(\frac{m-m'}{T_s}\tau)} d\tau}_{\text{not a function of Doppler variable } \theta}. \tag{6.10}$$

We have, finally, that the narrowband baseband-equivalent channel coefficients are stationary and the autocorrelation between different time samples of channel coefficients depends only on the Doppler-frequency profile $p_\Theta(\theta)$. Specifically, the autocorrelation is the (inverse) Fourier transform of the Doppler profile sampled at times $k'T_s$.

In Appendix B, it is shown that if the multipath angle-of-arrival is uniformly distributed, then the Doppler-frequency profile is bathtub-shaped, i.e., the Doppler-lag channel coefficients evolve according to Jake's model [40], i.e., (6.10) is proportional to $J_0(2\pi f_{\max} T_s k')$, where $J_0(\cdot)$ is the zeroth-order Bessel function of the first kind. The first zero crossing of $J_0(x)$ occurs at approximately $x = 3\pi/4$; it follows that the *coherence interval* of the narrowband baseband-equivalent channel is approximately $\frac{3}{8}\frac{1}{f_{\max}T_s}$ bit intervals. Note that the coherence interval is inversely proportional to the normalized Doppler frequency spread $f_{\max}T_s$.

Consider the time interval a mobile receiver takes to travel one wavelength: $T_{\lambda_c} := \frac{\lambda_c}{v_{\max}}$, where $\lambda_c := \frac{c}{f_c}$ is wavelength of the carrier frequency. The channel coefficients could vary significantly over this interval since the phase of the multipath components could change by up to 2π radians. We can connect the time interval T_{λ_c} to the coherence interval through the following ratio: $\frac{T_{\lambda_c}}{T_s}$—the number of bit intervals that occur in the time it takes the mobile to travel one wavelength. Recall that the (single-sided) Doppler-frequency spread is defined as $f_{\max} = \frac{v_{\max} f_c}{c}$; thus, through substitution, we have

$$\frac{T_{\lambda_c}}{T_s} = \frac{1}{f_{\max}T_s}. \tag{6.11}$$

The connection is now clear: the coherence interval is proportional to the number of bits transmitted while the mobile travels the distance of one wavelength.

6.2 Wideband Model

In this section, we examine the correlation of the wideband channel coefficients $\{h_{m,n}^{(k)}\}$ across scale m, lag n, *and* symbol index k and show that the time-variability of the channel is directly proportional to the normalized scale spread $\gamma_{\max} T_s f_o$ (discussed in Section 3.1.1). We propose an AR-model to approximate the time-variations and discuss the applicability of principal components combining (PCC) [2] to reduce the complexity of the scale-lag Rake combiner.

6.2.1 Wideband Channel Autocorrelation

To begin, we make the following observation. Assume there is a line-of-sight path between the transmitter and the receiver. We assign time zero to be when the output of the chip-pulse matched-filter peaks as a result of receiving the first chip of the first transmitted bit. If the channel geometry is fixed (no motion), then the first chip pulse of the *second* transmitted bit causes the chip-pulse matched-filter to peak at T_s seconds. However, if the receiver is travelling directly away from the transmitter with velocity $v_{\max}$, then the first chip pulse of the second transmitted bit causes the output of the chip-pulse matched-filter to peak at $T_s + \frac{v_{\max}}{c} T_s$ seconds—a time-offset of $\frac{v_{\max}}{c} T_s$ seconds relative to the fixed case. The excess time is caused by the transmitted signal travelling an excess distance of $v_{\max} T_s$ meters. In the case of open-loop timing synchronization, the mobile receiver expects the second bit to

arrive T_s seconds after the first, and a sampling phase mismatch of $\frac{v_{\max}}{c}T_s$ seconds occurs. As more bits are received, the sampling-phase mismatch accumulates to t_o seconds[14] and the bulk delay causes the channel energy to shift from the zeroth Rake finger to the first Rake finger. Eventually, the energy will shift beyond the last Rake finger and no information will be received. In the case of closed-loop (pilot-aided or decision-directed) timing synchronization, this bulk delay does not accumulate because it is absorbed by the synchronized sampling clock. In the presence of a "good" synchronization algorithm, the scale-spreading is defined relative to the mean scale shift. Under these assumptions, we assume that the channel coefficients are stationary.

To gain insight into the time-variation of the wideband channel coefficients, we numerically evaluate the autocorrelation sequence[15] $\mathrm{E}[h^{(0)}_{m,n}h^{(k')}_{m',n'}]$ with fixed scale-lag Rake finger indices. For example, fix $m = m' = 0$, and $n = n' = 0$; the autocorrelation over bit-index lag k' with different values of normalized scale spread $\gamma_{\max}f_oT_s$ are indicated as solid lines in Fig. 6.1. We assume a ring-of-scatterers model such that the scattering function $\Psi(a, \tau)$ is flat across lag τ and has a "bathtub" shape in scale a (see Section 5.1). The dashed lines in Fig. 6.1 correspond to a damped zeroth-order Bessel function of the first kind $J_0(2\pi\gamma_{\max}f_oT_sk')e^{-\gamma_{\max}f_oT_s|k'|}$, which closely approximates the autocorrelation sequence of a wideband channel with normalized scale spread of $\gamma_{\max}f_oT_s$. Recall that the first zero crossing of a zeroth-order Bessel function of the first kind $J_0(x)$ occurs at approximately $x = 3\pi/4$; it follows that the

[14]Recall that t_o is the lag spacing between the fingers of the Rake receiver.

[15]See Section 5.2 for the derivation.

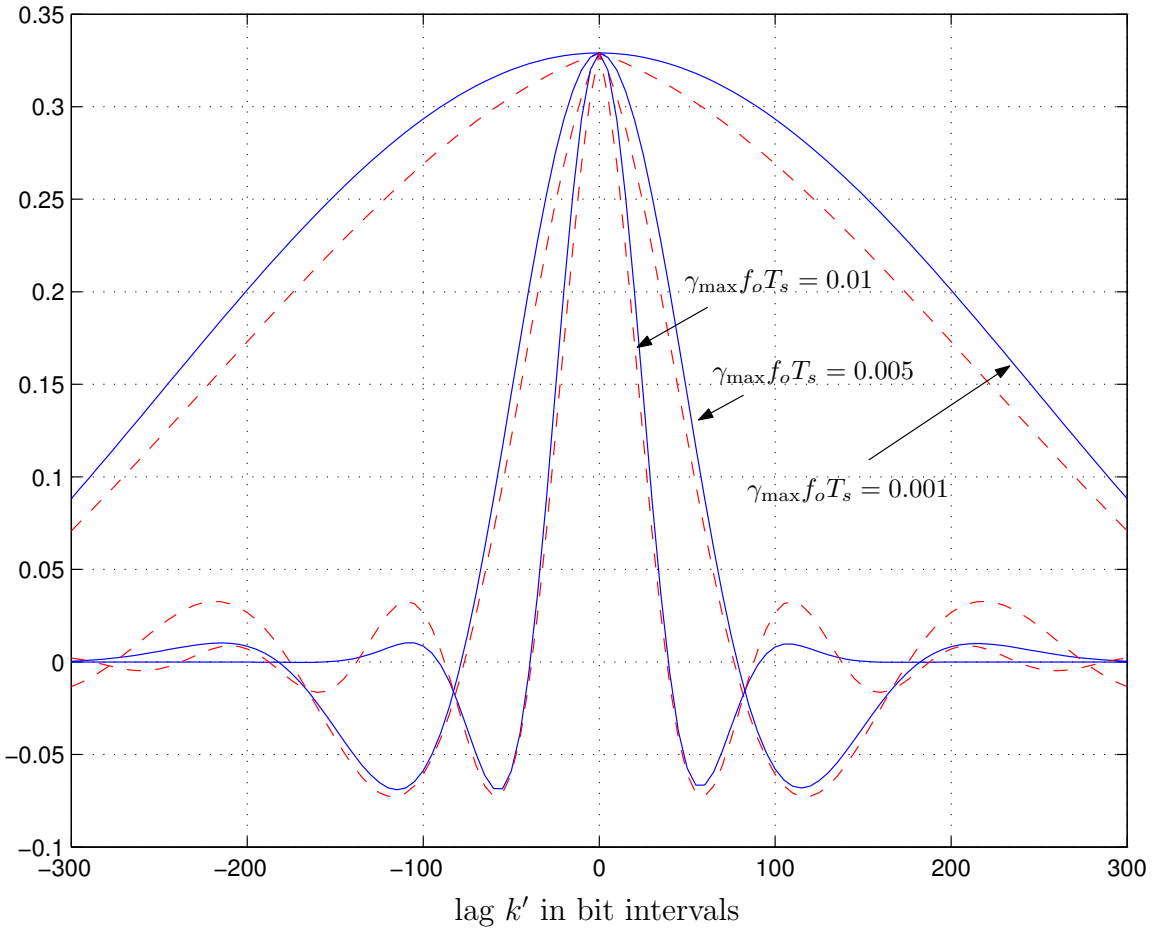

Figure 6.1: (Solid lines) Channel coefficient autocorrelation sequence $\mathrm{E}[h^{(0)}_{m,n} h^{(k')}_{m',n'}]$ for $m = m' = 0$, and $n = n' = 0$. (Dashed lines) Damped Bessel function approximation: $J_0\left(2\pi\gamma_{\max} f_o T_s k'\right) e^{-\gamma_{\max} f_o T_s |k'|}$. The normalized delay spread is $\tau_{\max} f_o = 0.5$.

wideband coherence interval of the wideband channel is approximately $\frac{3}{8}\frac{1}{\gamma_{\max} f_o T_s}$ bit intervals. Recalling the definition $\gamma_{\max} := \frac{v_{\max}}{c}$, we see that the wideband coherence interval is inversely proportional to the velocity of the mobile receiver. As velocity increases, scale spreading causes greater channel variation. This is reminiscent of the role the normalized Doppler spread plays for narrowband baseband-equivalent systems.

For reference, a normalized scale spread of 0.005 would be found in an RF system with mobile velocity of 10 km/hr, data rate of 1 Mbps, and bandwidth of 10 GHz, or in an RF system with velocity of 100 km/hr, data rate of 1 Mbps, and bandwidth of 1 GHz. A normalized scale spread of 0.05 would be found in an underwater acoustic telemetry system with mobile velocity of 1 km/hr, data rate of 1 kbps, and bandwidth of 50 kHz.

6.2.2 Autoregressive Model for Scale-Lag Channel Coefficients

After applying the whitening matrix $\boldsymbol{R}_{\boldsymbol{x}}^{-T/2}$ to the received signal vector $\boldsymbol{r}_k$, the system becomes

$$\begin{aligned} \boldsymbol{y}_k &:= R_{\boldsymbol{x}}^{-T/2}\boldsymbol{r}_k & (6.12) \\ &= b_k\boldsymbol{f}_k + \boldsymbol{n}_k & (6.13) \end{aligned}$$

where $\boldsymbol{n}_k := R_{\boldsymbol{x}}^{-T/2}\boldsymbol{w}_k$ is a AWGN vector with autocorrelation $\sigma_w^2\boldsymbol{I}$ and $\boldsymbol{f}_k$ is the whitened matched-filter combining coeffienent vector. Note that the time variations of $\boldsymbol{f}_k$ are a direct result of the underlying variations in $\boldsymbol{h}_k$, since $\boldsymbol{f}_k = R_{\boldsymbol{x}}^{-T/2}\boldsymbol{h}_k$.

We define the correlation $\boldsymbol{R}_{\boldsymbol{f}}(k') := \mathrm{E}[\boldsymbol{f}_o\boldsymbol{f}_{k'}^T]$ for generating time series realizations. We have observed that $\{\boldsymbol{R}_{\boldsymbol{f}}(k')\}$ can be approximately jointly diagonalized by a common set of eigenvectors: $\boldsymbol{R}_{\boldsymbol{f}}(k') \approx \boldsymbol{U}\boldsymbol{\Lambda}(k')\boldsymbol{U}^T$. Suppose that none of the correlation matrices in $\{\boldsymbol{R}_{\boldsymbol{f}}(k')\}_{k'=0}^{\infty}$ has more than $K_{\max}$ non-zero eigenvalues: $\{\lambda_l(k')\}_{l=1}^{K_{\max}}$. If we assume that the channel coefficients are zero-mean jointly-Gaussian processes, then combining-coefficient realizations can be generated by filtering a set of $K_{\max}$

uncorrelated white noise processes. The l^{th} noise process is filtered by an autoregressive (AR) model that is fit to the l^{th} eigenvalue sequence $\{\lambda_l(k')\}_{k'=0}^{\infty}$. For example, let $\{a_l(i)\}_{i=1}^{N_k}$ be the N_k model parameters computed from the Yule-Walker equation. Define $z_l(k) = q_l(k) - \sum_{i=1}^{N_k} a_l(k) z_l(k-i)$, where $q_l(k)$ is white-Gaussian noise of suitable variance. Now define the vector $\boldsymbol{z}_k := [z_1(k), z_2(k), \ldots, z_{K_{\max}}(k)]^T$ such that the coefficient vector realization is

$$\boldsymbol{f}_k = \boldsymbol{U}_{K_{\max}} \boldsymbol{z}_k, \tag{6.14}$$

where $\boldsymbol{U}_{K_{\max}}$ collects the $K_{\max}$ principal eigenvectors from $\boldsymbol{U}$.

6.2.3 Principal Components Combining

In Chapter 5, it is seen that the correlation matrix $\boldsymbol{R}_{\boldsymbol{f}}(0)$ produces a relatively small number of non-negligible eigenvalues compared to the number of scale-lag channel coefficients. For example, Fig. 5.6(b) shows that out of 15 eigenvalues, only four are greater than -25 dB. From (6.14), the channel dynamics are focused in a low-dimensional subspace spanned by the principal eigenvectors, which motivates the use of principal components combining (PCC) [2] to reduce receiver complexity. The PCC vector $\boldsymbol{f}_k$ is the SNR maximizing (BER minimizing) vector constrained to lie in the subspace spanned by the K_{pcc} principal eigenvectors of $\boldsymbol{R}_{\boldsymbol{f}}(0)$: [2]

$$\boldsymbol{f}_k = \underbrace{\boldsymbol{U}_{K_{\mathsf{pcc}}} \boldsymbol{\Theta}}_{\tilde{\boldsymbol{U}}_{K_{\mathsf{pcc}}}} \underbrace{\boldsymbol{\Theta}^T \boldsymbol{U}_{K_{\mathsf{pcc}}}^T \boldsymbol{f}_k}_{\tilde{\boldsymbol{z}}_k}, \tag{6.15}$$

where $\boldsymbol{U}_{K_{\mathsf{pcc}}}$ collects the K_{pcc} principal eigenvectors of $\boldsymbol{R}_{\boldsymbol{f}}(0)$, and $\boldsymbol{\Theta}$ is any $K_{\mathsf{pcc}} \times K_{\mathsf{pcc}}$ orthogonal matrix. The value K_{pcc} is a design choice that trades-off complexity and performance.

For operational convenience, the PCC vector can be applied in two stages: first, the whitened scale-lag Rake received vector $\boldsymbol{y}_k$ is projected onto the principal eigenvector subspace: $\tilde{\boldsymbol{y}}_k = \tilde{\boldsymbol{U}}^T_{K_{\mathsf{pcc}}} \boldsymbol{y}_k$; second, the projection is maximal ratio combined: $\hat{b}_k = \tilde{\boldsymbol{z}}_k^T \tilde{\boldsymbol{y}}_k$. The projection matrix $\tilde{\boldsymbol{U}}_{K_{\mathsf{pcc}}}$ describes the channel statistics (scale spread, delay spread), which change slowly and thus can be easily learned by the receiver (e.g., [103]). The parameters $\tilde{\boldsymbol{z}}_k$ represent the channel realization, which changes quickly, and hence must be tracked using, e.g., decision-directed LMS or RLS. We will perform a study of adaptive solutions in future work.

In Fig. 6.2, we show the bit error rate (BER) performance of the scale-lag PCC with perfect channel knowledge for increasing values of K_{pcc}—the number of principal components used in the receiver. The system has the same setup as in Fig. 5.6(b). Recall from Fig. 5.6(b) that $\boldsymbol{R_f}(0)$ gives four non-negligible eigenvalues; hence, the scale-lag Rake exploits full scale-lag diversity for $\bar{K} \geq 4$, as evidenced in Fig. 6.2.

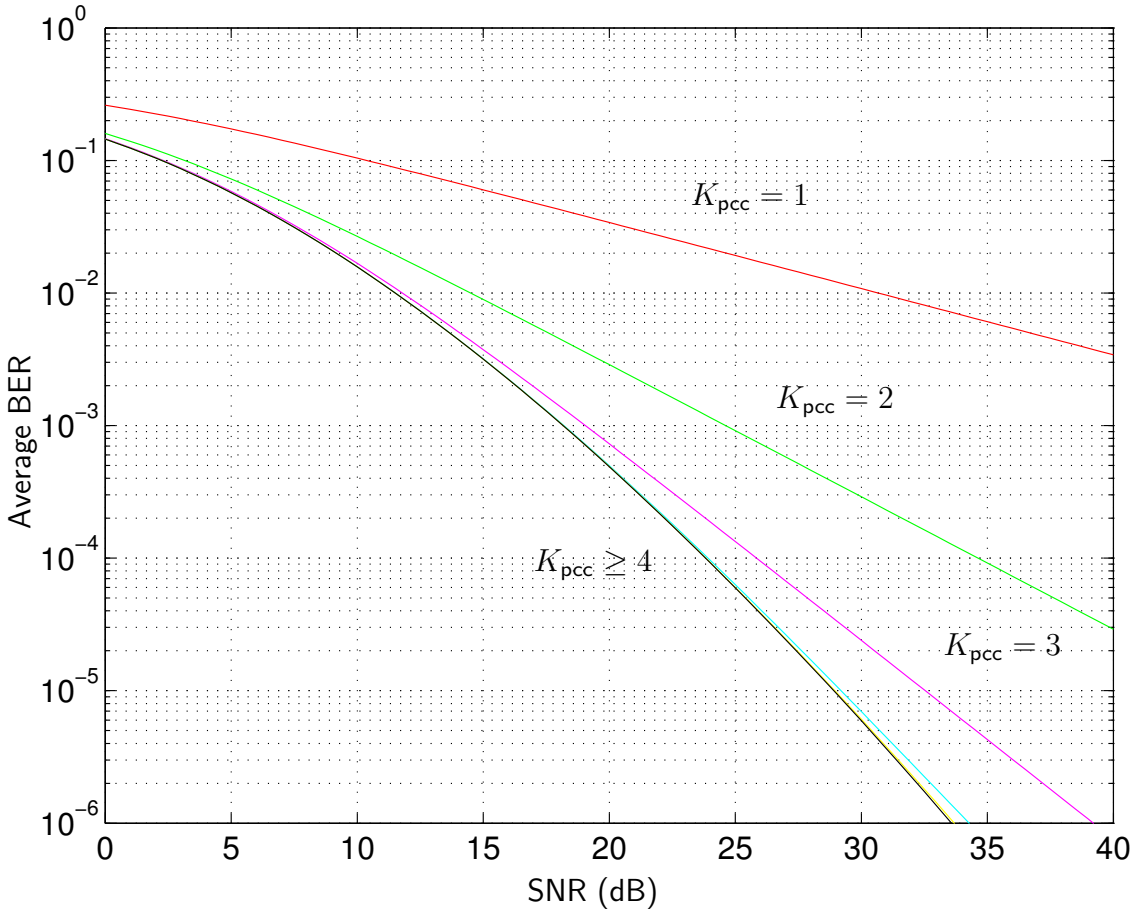

Figure 6.2: BER performance of scale-lag Rake receiver using PCC with various values of K_{pcc}. Same setup as in Fig. 5.6(b).

6.2.4 Acoustic Experiments

In order to investigate a "real-world" wideband channel, we present the results of experiments performed with an acoustic channel. We chose the acoustic channel for the reason that the equipment for transmitting and sampling the received signal was readily available. The wideband acoustic channel parallels the wideband electromagnetic channel since none of our analysis relies on electromagnetic polarization. The speed of wave propagation in air is approximately 340 m/s, or 1 foot per millisecond; light travels approximately one million times faster, i.e., 1 foot per nanosecond.

The parameters of the experiment were as follows:

- Omni-directional microphone was pointed straight up during the experiments.
- Sampling rate: 44100 samples/second.
- Peak frequency was $f_o = 4900$ Hz (single-sided bandwidth: $W \approx 2f_o = 9800$ Hz).
- Chip-pulse spacing was $T_o = 18/44100 = 4.0816 \times 10^{-4}$ seconds.
- Spreading gain: $N_p = 255$ chips/symbol.
- Bit duration $T_s = N_p T_o = 0.1041$ seconds.
- Velocity: about 1 inch/second.
- Normalized scale spread: $\gamma_{\max} f_o T_s = 0.0381$.
- Number of randomly chosen bits sent: 200.

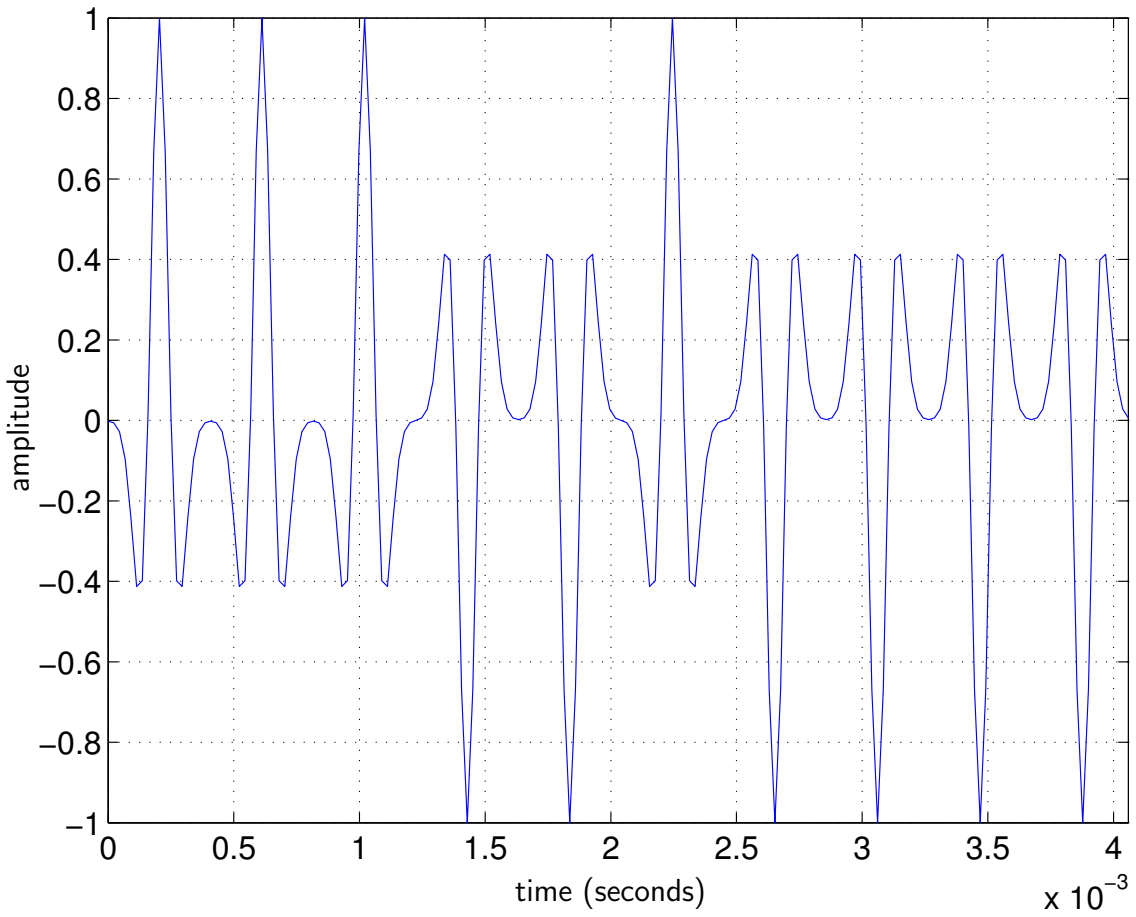

Figure 6.3: Zoomed view of a typical wideband DSSS transmit waveform.

- Chip-pulse shape: second-derivative Gaussian.
- Spreading sequence type: m-sequence [75]. See Fig. 6.3 for a plot of the DSSS waveform, Fig. 6.4 for a plot of the deterministic lag autocorrelation, and Fig. 6.5 for a plot of the deterministic dilation autocorrelation.

The experiments were performed in room 608 of Dreese Laboratory, which is a graduate student office. A cubicle-style divider separates one half of the room from

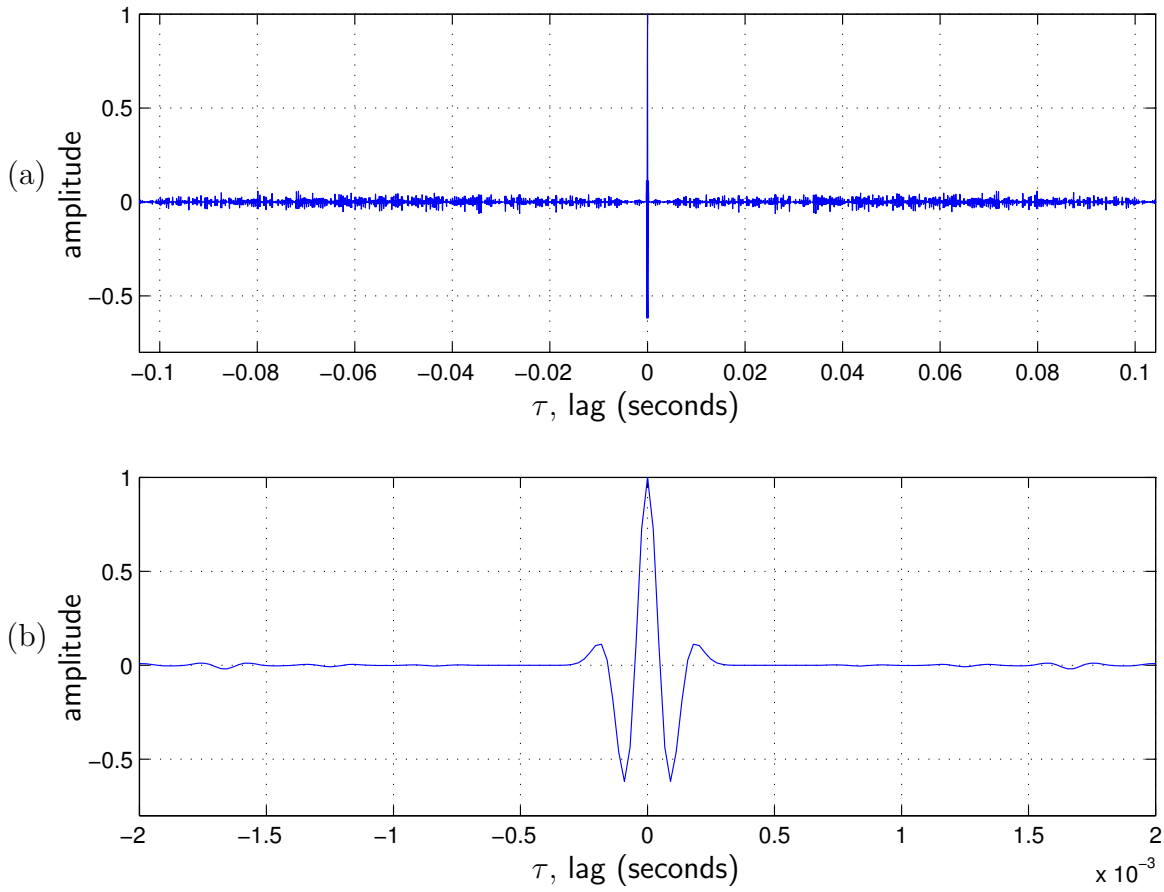

Figure 6.4: (a) Deterministic lag autocorrelation of a typical wideband DSSS transmit waveform realization: $\chi(1,\tau) = \langle x(t), x(t-\tau)\rangle$. (b) Zoomed view.

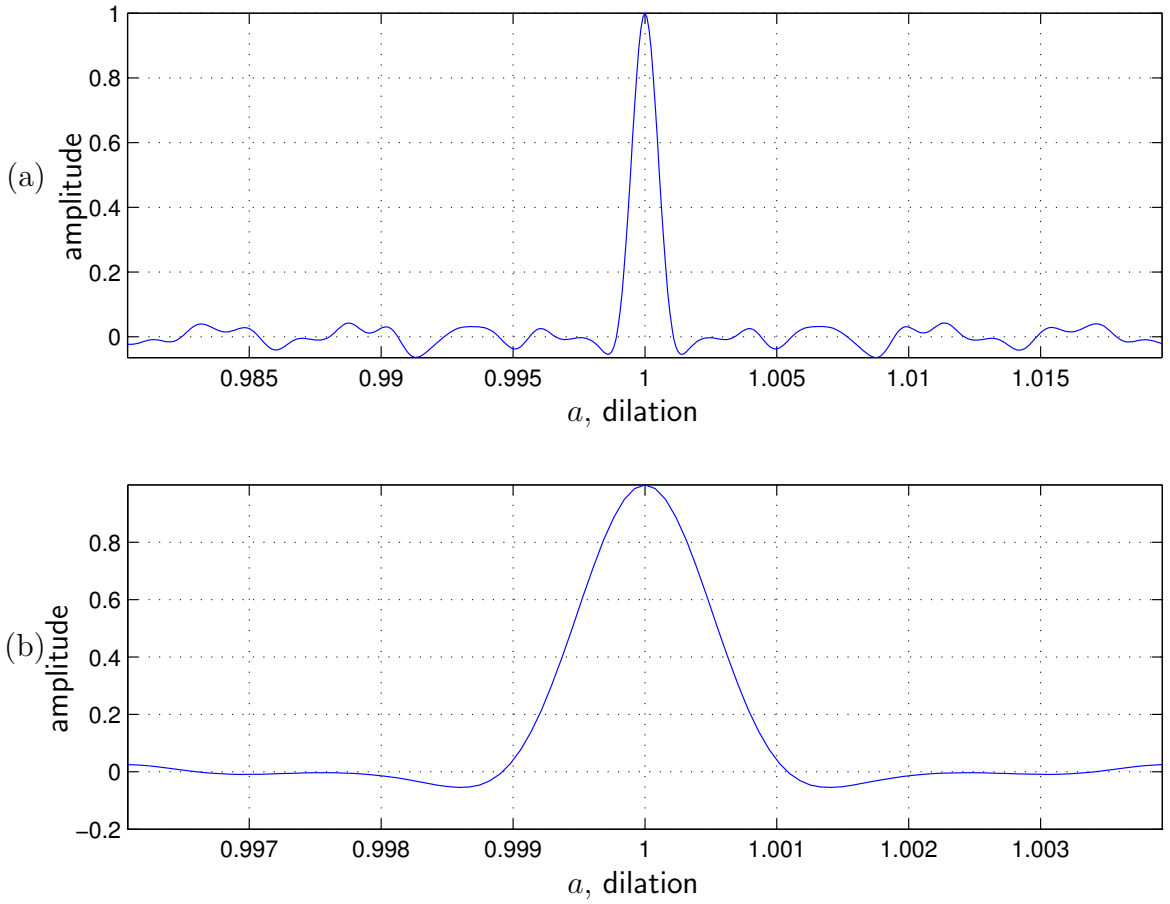

Figure 6.5: (a) Deterministic dilation autocorrelation of a typical wideband DSSS transmit waveform realization: $\chi(a,0) = \langle x(t), \frac{1}{\sqrt{a}} x(\frac{t}{a}) \rangle$. (b) Zoomed view.

the other and creates a non-line-of-sight channel between the transmitter and the receiver. The audio speaker and microphone are placed at opposite sides of the room; the speaker is set on a desk and the microphone placed on a book shelf approximately 5 inches from the wall. The doors and windows are closed during the experiments.

The acoustic experiment was performed under two conditions: first, a fixed microphone placement; and second, sliding the microphone at a constant velocity across the bookshelf toward the speaker, which is hidden behind the partition. Figure 6.6 and Fig. 6.7 show the results for a fixed microphone. Figure 6.6 shows the output of the PN-waveform matched filter across time and lag. We see that the channel is static over time. This is verified in Fig. 6.7(b), which shows a plot of the lag-zero channel coefficient $r_{0,0}^{(k)}$ as a function of bit index. Also shown in Fig. 6.7(b) is a plot of the first scale-finger $r_{1,0}^{(k)}$ of the scale-lag Rake receiver. Notice that there is no energy in this component. Figure 6.7(a) displays the output of the PN-waveform matched filter at time zero.

Figure 6.8 and Fig. 6.9 show the results for a sliding microphone. Figure 6.8 shows the output of the PN-sequence matched filter across time and lag. A V-shape can be seen, which indicates a time-varying channel. The left-hand side of the V results from the shortest reflective path from the acoustic speaker to the microphone, which grows shorter as the microphone travels ever closer to the speaker. The right-hand side of the V results from the strong echo from the wall directly behind the microphone; since the microphone is traveling away from the wall, the path lengthens. Figure 6.9(a) displays the output of the PN-waveform matched filter at time zero. In Fig. 6.9(b), we see that the first scale-finger $r_{1,0}^{(k)}$ is now extracting energy due to the dilation

effects of the wideband channel. Also shown as a dashed line is the wideband channel correlation sequence $\mathrm{E}[h_{0,0}^{(0)} h_{0,0}^{(k)}]$ for a normalized scale spread of $\gamma_{\max} f_o T_s = 0.0381$, corresponding to a mobile speed of 1 in./second. Note how closely the theoretical correlation sequence matches the dynamics of the experimental channel.

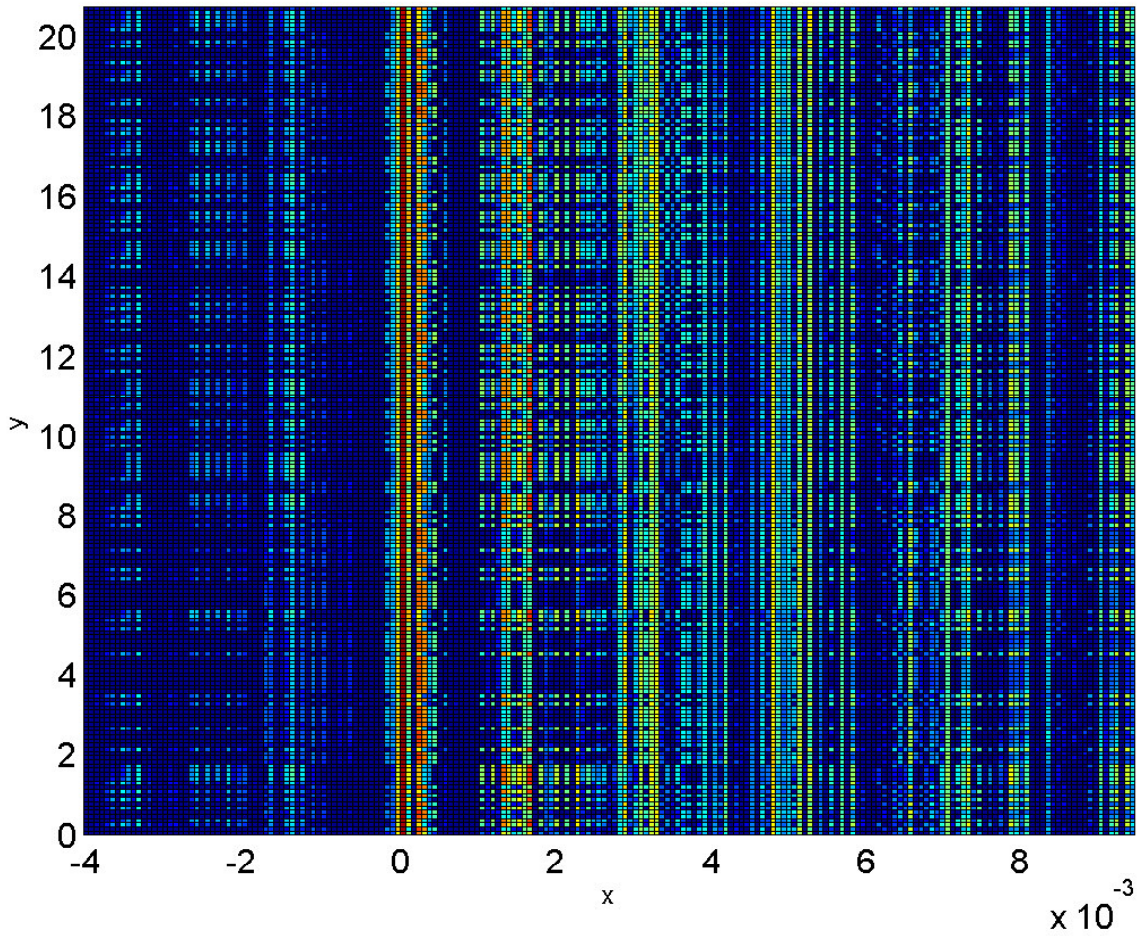

Figure 6.6: Time-invariant transfer function of an acoustic channel. The x-axis is lag (in seconds) and the y-axis is time (in seconds).

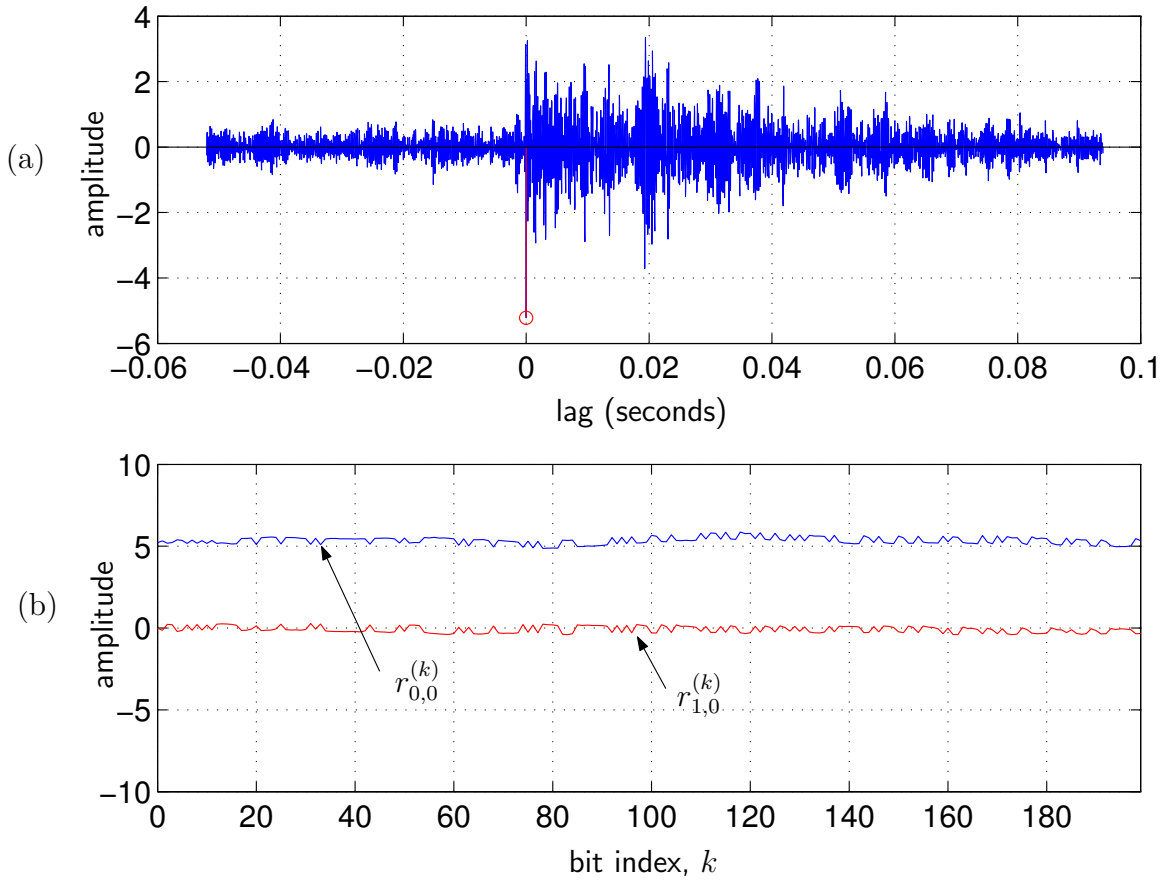

Figure 6.7: (a) Delay spread at time zero. (b) Channel coefficients $r_{0,0}^{(k)}$ and $r_{1,0}^{(k)}$ for a fixed receiver.

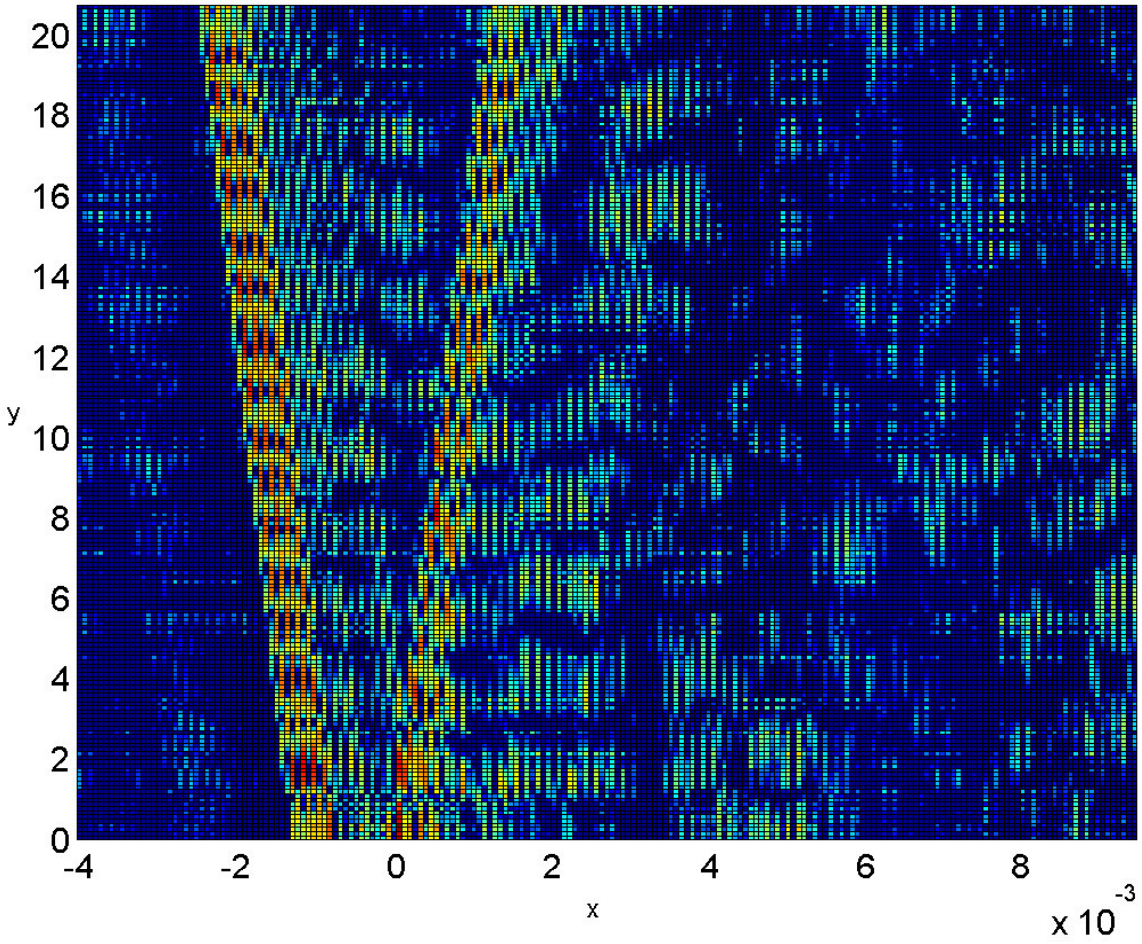

Figure 6.8: Time-varying transfer function of acoustic channel. The x-axis is lag (in seconds) and the y-axis is time (in seconds).

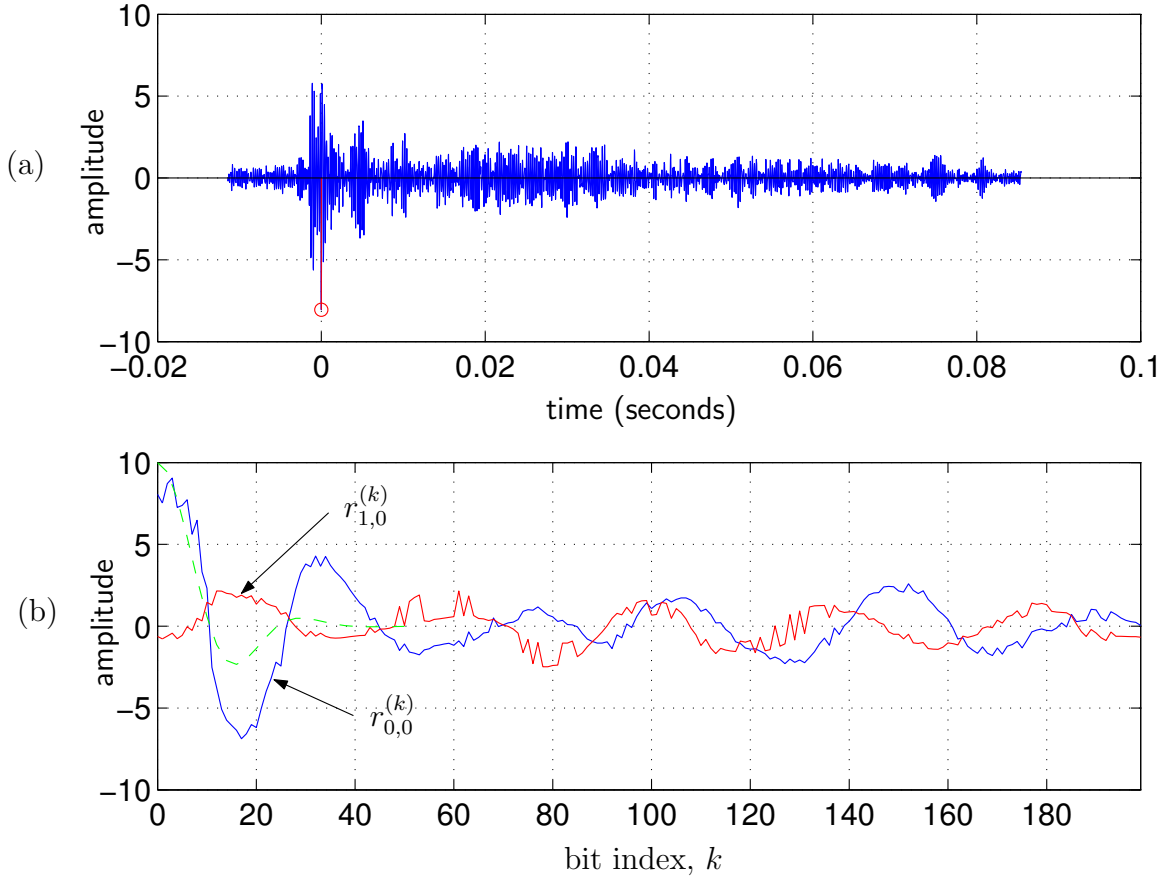

Figure 6.9: (a) Delay spread at time zero. (b) Channel coefficients $r_{0,0}^{(k)}$ and $r_{1,0}^{(k)}$ for a mobile receiver. The dashed line is $\mathrm{E}[h_{0,0}^{(0)}h_{0,0}^{(k)}]$ for a normalized scale spread of $\gamma_{\max}f_oT_s = 0.0381$, corresponding to a mobile speed of 1 in./second.

CHAPTER 7

CONCLUSIONS AND FUTURE RESEARCH

In this dissertation, we studied a *scale-lag* Rake receiver capable of leveraging the diversity that results from scale-lag spreading in mobile wideband direct-sequence spread-spectrum (DSSS) systems. The analysis applies to channels where narrowband assumptions are invalid, such as radio-frequency ultra-wideband (UWB) systems and underwater wideband acoustic systems. After defining the *minimum scale resolution* of a DSSS signal, we put the scale-lag Rake in the context of frame theory and produced guidelines for choosing the scale-spacing and lag-spacing parameters. We examined numerically the diversity-level exploited by the scale-lag Rake and made comparisons with the Doppler-lag Rake and conventional lag-only Rake. When the sampling rate of the chip-pulse matched filter was below the approximate Nyquist frequency, the proposed scale-lag Rake receiver outperformed the conventional lag-only Rake and the Doppler-lag Rake, since the scale-lag Rake was better matched to the scale-lag spreading of the wideband channel. When the sampling rate was above the approximate Nyquist frequency, the statistics produced by the conventional Rake receiver were approximately sufficient; thus, additional scale or Doppler components

provided little additional information or performance gain. We then made a time-series correlation analysis of the scale-lag Rake channel coefficients and examined using principal components combining (PCC) to reduce the complexity of the scale-lag Rake. Finally, we validated the wideband correlation-sequence analysis through an acoustic experiment.

Throughout this dissertation, suggestions have been given for future research. We conclude by collecting these and other suggestions into the following list.

- The wideband signals considered in this dissertation were transmitted directly at baseband. It would be interesting consider the case of modulated wideband signals, where Doppler-frequency offsets and time dilations both come into play.

- An interesting question is how sampling-frequency offsets affect the performance of the scale-lag Rake receiver. We conjecture that as long as the sampling of the scale-lag plane is "dense" enough, then frequency offsets shouldn't adversely impact the performance.

- Our proposed scale-lag Rake receiver performs a "rectangular" sampling of the scale-lag plane. It would be interesting to consider other non-rectangular scale-lag sampling schemes to reduce receiver complexity while preserving the ability to exploit channel diversity.

- We could provide a lower bound on receiver performance by deriving the matched-filter bound via a Karhuenan-Loeve expansion of the received signal. See [7] for details regarding the narrowband baseband-equivalent case.

- More realistic channel effects could be incorporated into the wideband model such as antenna effects and frequency-dependent attenuation.

- For higher data-rate systems such that inter-symbol interference (ISI) is no longer negligible, the design of ISI-mitigating receivers is critical.

- Considering the detection of target velocity in Radar systems, we could design optimal CRLB-minimizing chip-pulses by applying our ambiguity-function approximations in Appendix 3.4 to the Mellin transform analysis in [72]. The CRLB is minimized by maximizing the "Mellin spread" of the signal.

- We suggest examining adaptive subspace tracking algorithms in conjunction with the principal components combining (PCC) receiver. In addition, the optimal design and placement of pilots to aid in the learning of receiver parameters could be performed.

- As was pointed out in the previous chapter, the dilation effects of the wideband channel cause the received energy to shift across Rake fingers over time. It would be interesting to investigate the correlations between different Rake fingers over time for different channel geometries. This would aid in the design and implementation of channel tracking algorithms.

- We have assumed that the chip-pulse shape was a second-derivative Gaussian. It would be interesting to examine other pulse-shapes and consider designing chip-pulses to optimally extract scale-lag diversity from the mobile wideband channel.

- Throughout this thesis, we have considered the spreading sequences to be randomly chosen in order to make the analysis tractable. However, a careful design of the spreading sequence would enhance receiver performance.

APPENDIX A

REAL-VALUED DOPPLER-LAG BASIS

The real-valued Doppler-lag basis is a simple modification of the work in [85], which is included here to facilitate comparison to our baseband scale-lag Rake. The Doppler-lag basis functions are uniform frequency- and time-shifted versions of the DSSS waveform:

$$\tilde{x}_{m,n}(t) \;:=\; \tilde{y}_m(t/T_s)x(t-nt_o) \tag{A.1}$$

where

$$\tilde{y}_m(t) \;:=\; \begin{cases} \sqrt{2}\cos(2\pi mt) & m>0, \\ -\sqrt{2}\sin(2\pi mt) & m<0, \\ 1 & m=0. \end{cases} \tag{A.2}$$

In [85], it is shown that the complex-valued extension of the Doppler-lag basis (A.1) is approximately orthonormal, which motivated using the Doppler-lag Rake receiver to extract diversity in doubly-spread narrowband baseband-equivalent channels. The inner-product between Doppler-lag basis functions is derived in Section A.1.

A.1 Doppler-Lag Basis Function Inner Product

In the following we calculate the expectation of the inner product between basis functions of the Doppler-lag basis. This will be used to determine the noise statistics,

since the basis functions may not be orthogonal.

$$\begin{aligned}
\langle \tilde{x}_{m,n}(t), \tilde{x}_{m',n'}(t) \rangle &= \mathrm{E} \int \tilde{x}_{m,n}(t) \tilde{x}_{m',n'}(t) dt, && \text{(A.3)} \\
&= \frac{1}{N_p} \mathrm{E} \int \tilde{y}_m \left(\frac{t}{T_s} \right) \tilde{y}_{m'} \left(\frac{t}{T_s} \right) \\
&\quad \sum_{i=0}^{N_p-1} \sum_{l=0}^{N_p-1} c_i c_l p(t - nt_o - iT_o) p(t - n't_o - lT_o) dt, && \text{(A.4)} \\
&= \frac{\mathrm{E}\,|c_i|^2}{N_p} \int \tilde{y}_m \left(\frac{t}{T_s} \right) \tilde{y}_{m'} \left(\frac{t}{T_s} \right) \\
&\quad \sum_{i=0}^{N_p-1} p(t - nt_o - iT_o) p(t - n't_o - iT_o) dt. && \text{(A.5)}
\end{aligned}$$

Now make the variable substitution $s := t - nt_o + iT_o$ to obtain

$$\begin{aligned}
\langle \tilde{x}_{m,n}(t), \tilde{x}_{m',n'}(t) \rangle &= \frac{\mathrm{E}\,|c_i|^2}{N_p} \int \sum_{i=0}^{N_p-1} \tilde{y}_m \left(\frac{s + nt_o + iT_o}{T_s} \right) \tilde{y}_{m'} \left(\frac{s + nt_o + iT_o}{T_s} \right) \\
&\quad p(s) p(s - (n' - n)t_o) ds && \text{(A.6)} \\
&= \mathrm{E}\,|c_i|^2 \int \sum_{i=0}^{N_p-1} \frac{1}{N_p} \tilde{y}_m \left(\frac{s + nt_o}{T_s} + \frac{i}{N_p} \right) \tilde{y}_{m'} \left(\frac{s + nt_o}{T_s} + \frac{i}{N_p} \right) \\
&\quad p(s) p(s - (n' - n)t_o) ds. && \text{(A.7)}
\end{aligned}$$

Similar to the approximations in Appendix 3.4, we approximate the summation in (A.7) by an integral. The approximation is very tight when the number of chips N_p is large.

$$\begin{aligned}
\langle \tilde{x}_{m,n}(t), \tilde{x}_{m',n'}(t) \rangle &\approx \mathrm{E}\,|c_i|^2 \int \left[\int_0^1 \tilde{y}_m \left(\frac{s + nt_o}{T_s} + z \right) \tilde{y}_{m'} \left(\frac{s + nt_o}{T_s} + z \right) dz \right] \\
&\quad p(s) p(s - (n' - n)t_o) ds && \text{(A.8)}
\end{aligned}$$

For a moment, let us examine the integral over z in (A.8). For the case $m > 0$ and $m' > 0$, we have

$$\begin{aligned}
&\int_0^1 \tilde{y}_m\left(\frac{s+nt_o}{T_s}+z\right)\tilde{y}_{m'}\left(\frac{s+nt_o}{T_s}+z\right)dz \\
&= \int_0^1 2\cos\left(\frac{2\pi m(s+nt_o)}{T_s}+2\pi mz\right)\cos\left(\frac{2\pi m'(s+nt_o)}{T_s}+2\pi m'z\right)dz, \\
&= \int_0^1 \cos\left(2\pi m\frac{s+nt_o}{T_s}+2\pi m'\frac{s+nt_o}{T_s}+2\pi(m+m')z\right) \\
&\quad +\cos\left(2\pi m\frac{s+nt_o}{T_s}-2\pi m'\frac{s+nt_o}{T_s}+2\pi(m-m')z\right)dz, \\
&= \int_0^1 \cos\left(2\pi(m+m')z\right)+\cos\left(2\pi(m-m')z\right)dz, \qquad \text{(A.9)} \\
&= \delta_{m-m'}, \qquad \text{(A.10)}
\end{aligned}$$

where δ_m is the Kroneker delta function. The step from (A.9) to (A.10) is true because $m, m' > 0$. For the case $m > 0$ and $m' < 0$ we have

$$\begin{aligned}
&\int_0^1 \tilde{y}_m\left(\frac{s+nt_o}{T_s}+z\right)\tilde{y}_{m'}\left(\frac{s+nt_o}{T_s}+z\right)dz \\
&= -\int_0^1 2\cos\left(\frac{2\pi m(s+nt_o)}{T_s}+2\pi mz\right)\sin\left(\frac{2\pi m'(s+nt_o)}{T_s}+2\pi m'z\right)dz, \\
&= \int_0^1 -\sin\left(2\pi m\frac{s+nt_o}{T_s}+2\pi m'\frac{s+nt_o}{T_s}+2\pi(m+m')z\right) \\
&\quad -\sin\left(2\pi m\frac{s+nt_o}{T_s}-2\pi m'\frac{s+nt_o}{T_s}+2\pi(m-m')z\right)dz, \\
&= \int_0^1 -\sin\left(2\pi(m+m')z\right)-\sin\left(2\pi(m-m')z\right)dz, \qquad \text{(A.11)} \\
&= 0. \qquad \text{(A.12)}
\end{aligned}$$

By symmetry, the result in (A.12) is true for the case $m < 0$ and $m' > 0$. Finally, we examine the case $m < 0$ and $m' < 0$

$$\begin{aligned}
&\int_0^1 \tilde{y}_m\left(\frac{s+nt_o}{T_s}+z\right)\tilde{y}_{m'}\left(\frac{s+nt_o}{T_s}+z\right)dz \\
&= \int_0^1 2\sin\left(\frac{2\pi m(s+nt_o)}{T_s}+2\pi mz\right)\sin\left(\frac{2\pi m'(s+nt_o)}{T_s}+2\pi m'z\right)dz, \\
&= \int_0^1 \cos\left(2\pi m\frac{s+nt_o}{T_s}-2\pi m'\frac{s+nt_o}{T_s}+2\pi(m-m')z\right) \\
&\quad -\cos\left(2\pi m\frac{s+nt_o}{T_s}+2\pi m'\frac{s+nt_o}{T_s}+2\pi(m+m')z\right)dz, \\
&= \int_0^1 \cos\left(2\pi(m-m')z\right)-\cos\left(2\pi(m+m')z\right)dz, \qquad \text{(A.13)} \\
&= \delta_{m-m'}. \qquad \text{(A.14)}
\end{aligned}$$

After checking all other cases of m, m' in a similar manner, we have the following result:

$$\int_0^1 \tilde{y}_m\left(\frac{s+nt_o}{T_s}+z\right)\tilde{y}_{m'}\left(\frac{s+nt_o}{T_s}+z\right)dz = \delta_{m-m'}. \qquad \text{(A.15)}$$

We plug (A.15) into (A.8) to obtain the tight approximation of the inner-product between two Doppler-lag basis functions

$$\langle \tilde{x}_{m,n}(t), \tilde{x}_{m',n'}(t)\rangle \approx \mathrm{E}\,|c_i|^2\delta_{m-m'}\chi_p(1,(n'-n)t_o) \qquad \text{(A.16)}$$

where

$$\chi_p(a,\tau) := \int p(t)\frac{1}{\sqrt{a}}p\left(\frac{t-\tau}{a}\right)dt \qquad \text{(A.17)}$$

A.2 Second-Derivative Gaussian Chip Pulse

For the Doppler-lag basis (A.1) employing unit energy second-derivative Gaussian chip pulses (3.3), it can be shown using the same approach as Appendix **??** that for

large N_p, the autocorrelation between channel coefficients can be approximated by

$$\mathrm{E}[\tilde{h}_{m,n}\tilde{h}_{m',n'}] \approx \int_0^{\tau_{max}f_o} \int_{-\gamma_{max}T_s f_o}^{\gamma_{max}T_s f_o} \Psi(1+\frac{\bar{\gamma}}{T_s f_o}, \frac{\bar{\tau}}{f_o}) \bar{R}_{m,n}(\bar{\gamma},\bar{\tau}) \bar{R}_{m',n'}(\bar{\gamma},\bar{\tau}) d\bar{\gamma} d\bar{\tau},$$

where

$$\bar{R}_{m,n}(\bar{\gamma},\bar{\tau}) = \int_0^1 \tilde{y}_m(x) \chi_p(1, (\bar{\gamma}x - n + \bar{\tau})t_o) dx. \tag{A.18}$$

The expression $\chi_p(1,\tau)$ follows from (3.34).

APPENDIX B

NARROWBAND SCATTERING FUNCTION

In the following, we derive the narrowband baseband-equivalent scattering function $\tilde{\Psi}(\theta, \tau)$, which quantifies the statistics of the narrowband baseband-equivalent fading channel. We will proceed differently than the familiar Jakes derivation [40]. Instead of considering the transmission of a narrowband baseband-equivalent signal through a multipath channel and deriving the autocorrelation of the output, we directly compute the narrowband baseband-equivalent scattering function.

B.1 Derivation

Similar to the wideband case in Section 5.1, we assume that the narrowband baseband-equivalent spreading function $\tilde{H}(f, \tau)$ can be modeled as a sum of N discrete paths:

$$\tilde{H}(\theta, \tau) \;:=\; \sum_{n=0}^{N-1} \tilde{l}_n \delta(\theta - \theta_n)\delta(\tau - \tau_n), \tag{B.1}$$

where $\delta(\cdot)$ is the Dirac delta function and where the n^{th} path has complex-valued gain $\tilde{l}_n$, Doppler-frequency shift θ_n, and lag τ_n [90].

B.1.1 Assumptions

In order to proceed with the derivation, we make the following typical assumptions on the statistics of the narrowband baseband-equivalent spreading function:

(A1) The path parameters $\{\theta_n\}$, $\{\tilde{l}_n\}$, and $\{\tau_n\}$ are i.i.d. across paths with joint density $p_{\Theta,\tilde{L},\mathcal{T}}(\cdot,\cdot,\cdot)$.

(A2) The path amplitudes are zero mean, i.e., $\mathrm{E}[\tilde{l}_n] = 0$.

(A3) The Doppler-frequency shift θ_n is independent of the amplitude $\tilde{l}_n$ and lag τ_n, i.e., $p_{\Theta,\tilde{L},\mathcal{T}}(\cdot,\cdot,\cdot) = p_{\Theta}(\cdot)p_{\tilde{L},\mathcal{T}}(\cdot,\cdot)$.

These assumptions arise when there is no line-of-sight between the transmitter and receiver. Note that the amplitude and lag are often correlated in wireless communications channels where propagation losses manifest as an exponentially decaying function of increasing lag [93].

From assumptions (A1) and (A2) we write

$$\begin{aligned}
&\mathrm{E}[\tilde{H}(\theta',\tau')\tilde{H}(\theta'',\tau'')] \\
&\quad = \mathrm{E}[\delta(\theta'-\theta_0)\delta(\theta''-\theta_0)N|h_0|^2\delta(\tau'-\tau_0)\delta(\tau''-\tau_0)]. \qquad \text{(B.2)}
\end{aligned}$$

Assumption (A1) allows us to consider the first path without loss of generality. From assumption (A3),

$$\begin{aligned}
&\mathrm{E}[\delta(\theta'-\theta_0)\delta(\theta''-\theta_0)] \\
&\quad = \int \delta(\theta'-\theta)\delta(\theta''-\theta)p_{\Theta}(\theta)d\theta, \\
&\quad = p_{\Theta}(\theta')\delta(\theta'-\theta''), \qquad \text{(B.3)}
\end{aligned}$$

and

$$\begin{aligned}
&\mathrm{E}[N|\tilde{l}_0|^2\delta(\tau'-\tau_0)\delta(\tau''-\tau_0)] \\
&= N\iint |\tilde{l}|^2\delta(\tau'-\tau)\delta(\tau''-\tau)p_{\tilde{L},\mathcal{T}}(\tilde{l},\tau)d\tau d\tilde{l}, \\
&= f_{\mathcal{T}}(\tau')\delta(\tau'-\tau''),
\end{aligned} \tag{B.4}$$

where we define

$$f_{\mathcal{T}}(\tau) := Np_{\mathcal{T}}(\tau)\int |\tilde{l}|^2 p_{\tilde{L}|\mathcal{T}}(\tilde{l}|\tau)d\tilde{l}. \tag{B.5}$$

The function $f_{\mathcal{T}}(\tau)$ is the *delay profile* as a function of lag τ. Thus, a decaying energy profile can be modeled.

We substitute (B.3) and (B.4) into (B.2) to obtain

$$\mathrm{E}[\tilde{H}(\theta,\tau)\tilde{H}(\theta',\tau')] = \underbrace{p_{\Theta}(\theta)f_{\mathcal{T}}(\tau)}_{:=\tilde{S}(\theta,\tau)}\delta(\theta-\theta')\delta(\tau-\tau'), \tag{B.6}$$

where $\tilde{S}(\theta,\tau)$ is the *narrowband baseband-equivalent scattering function*, which quantifies the distribution of received power as a function of Doppler and delay.

B.1.2 Ring of Scatterers

Now that the form of the narrowband baseband-equivalent scattering function has been determined, we investigate the *Doppler-frequency profile* $p_{\Theta}(\cdot)$. An often studied channel geometry is a fixed transmitter and dense ring of scatterers surrounding the mobile receiver. In this case, the relation between the angle-of-arrival relative to the direction of travel ξ and Doppler frequency θ is

$$\theta = f_{max}\cos(\xi). \tag{B.7}$$

where $f_{max} = \frac{v_{max}}{c} f_c$ is the (one-sided) maximum Doppler-frequency spread. Given the angle of arrival distribution $p_\Xi(\cdot)$, it is a simple matter to compute the Doppler-frequency distribution $p_\Theta(\cdot)$,

$$p_\Theta(\theta) = \frac{1}{\gamma_{max}} p_Y\left(\frac{\theta}{\gamma_{max}}\right), \tag{B.8}$$

where $Y = \cos(\Xi)$ and

$$p_Y(y) = \frac{p_\Xi(\cos^{-1}(y)) + p_\Xi(-\cos^{-1}(y))}{\sqrt{1-y^2}}. \tag{B.9}$$

If the angle of arrival ξ is distributed uniformly on $(-\pi, \pi]$, then we have

$$p_Y(y) = \frac{1}{\pi\sqrt{1-y^2}}, \quad |y| < 1, \tag{B.10}$$

which is a familiar "bathtub shape" [40] (see Fig. B.1). We call the function $p_\Theta(\theta)$ the *Doppler profile*.[16]

[16]The Doppler profile is also known as the Doppler spectrum [90].

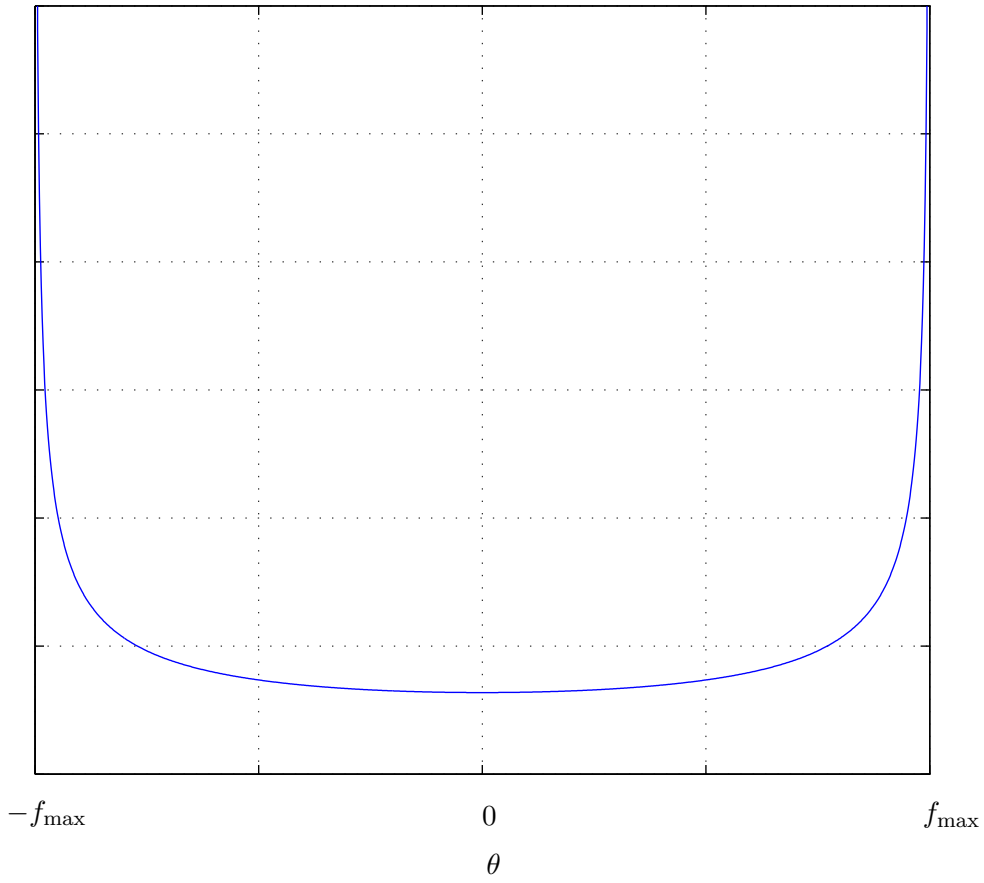

Figure B.1: Plot of "bathtub-shaped" Doppler-frequency profile $p_\Theta(\theta)$. The angle of arrival ξ is uniformly distributed.

BIBLIOGRAPHY

[1] S. M. Alamouti. A simple transmit diversity technique for wireless communications. *IEEE Journal on Selected Areas In Communications*, 16(8):1451–1458, Oct 1998.

[2] M.-S. Alouini, A. Scaglione, and G. B. Giannakis. PCC: Principal components combining for dense correlated multipah fading environments. *Proc. IEEE Vehicular Technology Conference*, 5:2510–2517, Sept. 2000.

[3] A. Alvarez, G. Valera, M. Lobeira, R. Torres, and J. Garcia. New channel impulse response model for UWB indoor system simulations. *Proc. IEEE Vehicular Technology Conference*, 1:1–5, Apr. 2003.

[4] M. Antweiler, L. Bomer, and H.-D. Luke. Perfect ternary arrays. *IEEE Trans. on Information Theory*, 36(3):696–705, May 1990.

[5] R. Balan, H. V. Poor, S. Rickard, and S. Verdú. Time-frequency and time-scale canonical representations of doubly spread channels. *Proc. European Signal Processing Conf.*, Sep. 2004.

[6] J. Bartrand, P. Bertrand, and J.-P. Ovarlez. *The Transforms and Applications Handbook*, chapter 11, pages 11–1. CRC Press LLC, 2 edition, 2000.

[7] N. Bass and D. Taylor. Matched filter bounds for wireless communicatino over rayleigh fading dispersive channels. *IEEE Trans. on Communications*, 49:1525–1528, Sept. 2001.

[8] A. Bayesteh and M. Nasiri-Kenari. Iterative interference cancellation and decoding for a coded UWB-TH-CDMA system in multipath channels using MMSE filters. *Proc. IEEE Internat. Symposium on Personal, Indoor and Mobile Radio Communications*, 2:1555–1559, Sep. 2003.

[9] S. Bhashyam, A. Sayeed, and B. Aazhang. Time-selective signaling and reception for communication over multipath fading channels. *IEEE Trans. on Communications*, 48(1):83–94, Jan. 2000.

[10] R. Blazquez, P. Newaskar, and A. Chandrakasan. Coarse acquisition for ultra wideband digital receivers. *Proc. IEEE Internat. Conf. on Acoustics, Speech, and Signal Processing*, 4:137–140, Apr. 2003.

[11] R. Boudreau, J.-Y. Chouinard, and A. Yongacoglu. Exploiting doppler-diversity in flat, fast fading channels. *Proc. Canadian Conf. on Electrical and Computer Engineering*, 1:270–274, Mar. 2000.

[12] I. R. Capoglu, Y. G. Li, and A. Swami. Effect of doppler spread in OFDM based UWB systems. *IEEE Trans. on Wireless Communications*, 2004. to appear.

[13] C. Carbonelli, U. Mengali, and U. Mitra. Synchronization and channel estimation for UWB signals. *Proc. IEEE Global Telecommunications Conf.*, 2:764–768, Dec. 2003.

[14] D. Cassioli, M. Win, and A. Molisch. The ultra-wide bandwidth indoor channel: from statistical model to simulations. *IEEE Journal on Selected Areas In Communications*, 20(6):1247–1257, Aug. 2002.

[15] D. Cassioli, M. Win, F. Vatalaro, and A. Molisch. Performance of low-complexity rake reception in a realistic UWB channel. *Proc. IEEE Intern. Conf. on Communication*, 2:763–767, 2002.

[16] J. Cha. Class of ternary spreading sequences with zero correlation duration. *PElectronics Letters*, 37(10):636–637, May 2001.

[17] J.-S. Cha and K. Tsubouchi. New ternary spreading codes with zero-correlation duration for approximately synchronized cdma. *Proc. of IEEE International Symposium on Industrial Electronics*, 1:312–317, Jun. 2001.

[18] J. Choi and W. Stark. Performance of ultra-wideband communications with suboptimal receivers in multipath channels. *IEEE Journal on Selected Areas In Communications*, 20:1754–1766, Dec. 2002.

[19] F. C. Commission. New public safety applications and broadband internet access among uses envisioned by FCC authorization of ultra-wideband technology. Press release announcing the ammended Part 15 rules allowing intentional UWB emissions, February 2002.

[20] F. C. Commission. Revision of part 15 of the commission's rules regarding ultra-wideband transmission systems, First Report and Order. *ET Docket 98-153, FCC 02-48*, pages 1–118, Feb. 14 2002.

[21] J. Conroy, J. LoCicero, and D. Ucci. Communication techniques using monopulse waveforms. *Military Communications Conference*, 2:1181–1185, Oct 1999.

[22] J. N. da Silva and M. de Campos. Performance comparison of binary and quaternary UWB modulation schemes. *Proc. IEEE Global Telecommunications Conf.*, 2:789–793, Dec. 2003.

[23] I. Daubechies. The wavelet transform, time-frequency localization and signal analysis. *IEEE Trans. on Information Theory*, 36(5):961–1005, Sept. 1990.

[24] I. Daubechies. *Ten Lectures on Wavelets*. Society for Industrial And Applied Mathematics, Philadelphia, 1992.

[25] J. Davies and S. Pointer. UW communication system design for severely dispersed channels. *OCEANS 1998 MTS/IEEE Conference and Exhibition*, 2:1022–1027, Sep. 1998.

[26] J. Davies, S. Pointer, and S. Dunn. Wideband acoustic communications dispelling narrowband myths. *OCEANS 2000 MTS/IEEE Conference and Exhibition*, 1:377–384, Sep. 2000.

[27] M. Dawood and R. Narayanan. Generalised wideband ambiguity function of a coherent ultrawideband random noise radar. *IEE proc.-Radar, Sonar Navig.*, 150(5):379–386, Oct. 2003.

[28] S. Dunn, J. Davies, and S. Pointer. A real-time high data rate acoustic communications receiver demonstration system. *OCEANS 2000 MTS/IEEE Conference and Exhibition*, 1:385–390, Sep. 2000.

[29] J. Foerster. The effects of multipath interference on the performance of UWB systems in an indoor wireless channel. *Proc. IEEE Vehicular Technology Conference*, 2:1176–1180, Spring 2001.

[30] J. Foerster. The performance of a direct-sequence spread ultra-wideband system in the presence of multipath, narrowband interference, and multiuser interference. *Conference on Ultra Wideband Systems and Technologies*, May 2002.

[31] J. Foerster, M. Pendergrass, and A. Molish. A channel model for ultra wideband indoor communication. *Internation Symposium on Wireless Personal Multimedia Communication*, Oct. 2003.

[32] A. Forouzan, M. Nasiri-Kenari, and J. Salehi. Performance analysis of time-hopping spread-spectrum multiple-access systems: uncoded and coded schemes. *IEEE Trans. on Communications*, 1:671–681, Oct. 2002.

[33] A. Fuxjaeger and R. Iltis. Acquisition of timing and doppler-shift in a direct-sequence spread-spectrum system. *IEEE Trans. on Communications*, 42(10):2870–2880, Oct. 1994.

[34] M. D. Gallagher. On the FCC's UWB proceeding: An examination of the government's spectrum management process. Jun. 2002.

[35] G. Giannakis and C. Tepedelenlioglu. Basis expansion models and diversity techniques for blind identification and equalization of time-varying channels. *Proceedings of the IEEE*, 86(10):1969–1986, Oct. 1998.

[36] R. Harjani, J. Harvey, and R. Sainati. Analog/RF physical layer issues for UWB systems. *Proceedings of International Conference on VLSI Design*, pages 941–948, Jan. 2004.

[37] N. He and C. Tepedelenlioglu. Adaptive synchronization for non-coherent UWB receivers. *Proc. IEEE Internat. Conf. on Acoustics, Speech, and Signal Processing*, 4:517–520, May 2004.

[38] M. Ho, V. Somayazulu, J. Foerster, and S. Roy. A differential detector for an ultra-wideband communications system. *Proc. IEEE Vehicular Technology Conference*, 4:1896–1900, Spring 2002.

[39] Y.-W. Hong and A. Scaglione. Bayesian detector and adaptive receivers for TH-SSMA ultra-wide bandwidth impulse radio. *Proc. Asilomar Conf. on Signals, Systems and Computers*, 2002.

[40] W. Jakes. *Microwave Mobile Communications*. IEEE press, Piscataway, NJ, 1993.

[41] Y. Jiang and A. Papandreou-Suppappola. Characterization of wideband time-varying channels with multipath-scale diversity. *Proc. IEEE Workshop on Statistical Signal and Array Processing*, (5):50–53, Sep. 2003.

[42] Y. Jiang and A. Papandreou-Suppappola. Time-scale cononical model for wideband system characterization. *Proc. IEEE Internat. Conf. on Acoustics, Speech, and Signal Processing*, Mar. 2005.

[43] Q. Jin, K. M. Wong, and Z.-Q. Luo. The estimation of time delay and Doppler stretch of wideband signals. *IEEE Trans. on Signal Processing*, 43(4):904–916, Apr. 1995.

[44] G. Kaiser. Physical wavelets and radar: A variational approach to remote sensing. *IEEE Antennas and Propagation Magazine*, 38(1):15–24, Feb. 1996.

[45] D. B. Kilfoyle and A. B. Baggeroer. The state of the art in underwater acoustic telemetry. 25(1), Jan. 2000.

[46] A. G. Klein, D. R. Brown, III, D. L. Goeckel, and C. R. Johnson, Jr. RAKE reception for UWB communication systems with intersymbol interference. *Proc. IEEE Workshop on Signal Processing Advances in Wireless Communication*, pages 244–248, Jun. 2003.

[47] J. Kunisch and J. Pamp. Radio channel model for indoor UWB WPAN environments, 02281r0p802-15_sg3a-imst-response-call-contributions-uwb-channel-models.pdf, Jun. 2002. [Online]. Available: http://grouper.ieee.org/groups/802/15/pub/2002/Jul02/.

[48] J. Kunisch and J. Pamp. An ultra-wideband space-variant multipath indoor radio channel model. *Conference on Ultra Wideband Systems and Technologies*, pages 290–294, Nov. 2003.

[49] D. Laney, G. Maggio, F. Lehmann, and L. Larson. Ber performance and spectral properties of interleaved convolutional time hopping for UWB impulse radio. *Proc. IEEE Global Telecommunications Conf.*, 4:1994–1998, Dec. 2003.

[50] H. Lee, B. Han, Y. Shin, and S. Im. Multipath characteristics of impulse radio channels. *Proc. IEEE Vehicular Technology Conference*, 3:2487–2491, May 2000.

[51] H. Lee and S. Im. New impulse radio receivers in multipath environments. *Proc. IEEE Vehicular Technology Conference*, 4:1891–1895, Spring 2002.

[52] J.-Y. Lee and R. A. Scholtz. Ranging in dense multipath environment using an UWB radio link. *IEEE Journal on Selected Areas In Communications*, 20(9):1677–1683, Dec. 2002.

[53] G. Leus, S. Zhou, and G. Giannakis. Orthogonal multiple access over time- and frequency-selective channels. *IEEE Trans. on Information Theory*, 49(8):1942–1950, Aug. 2003.

[54] Q. Li and L. Rusch. Hybrid rake / multiuser receivers for UWB. *Radio and Wireless Conference*, pages 203–206, Aug. 2003.

[55] F.-Y. Lin and J.-M. Liu. Ambiguity functions of laser-based chaotic radar. *IEEE Journ. of Quantum Electronics*, 40(12):1732–1738, Dec. 2004.

[56] V. Lottici, A. D'Andrea, and U. Mengali. Channel estimation for ultra-wideband communications. *IEEE Journal on Selected Areas In Communications*, 20:1638–1645, Dec. 2002.

[57] W. Lovelace and J. Townsend. The effects of timing jitter and tracking on the performance of impulse radio. *IEEE Journal on Selected Areas In Communications*, 20:1646–1651, Dec. 2002.

[58] X. Ma and G. Giannakis. Maximum-diversity transmissions over time-selective wireless channels. *Proc. IEEE Wireless Communication and Networking Conf.*, 1:497–501, Mar. 2002.

[59] X. Ma and G. Giannakis. Maximum-diversity transmissions over doubly selective wireless channels. *IEEE Trans. on Information Theory*, 49(7):1832–1840, Jul. 2003.

[60] X. Ma, G. Giannakis, and B. Lu. Block differential encoding for rapidly fading channels. *IEEE Trans. on Communications*, 52(3):416–425, Mar. 2004.

[61] Y. Ma, S. Pasupathy, F. Chin, and B. Kannan. Acquisition performance of an ultra wide-band communications system over a multiple-access fading channel. *Conference on Ultra Wideband Systems and Technologies*, May 2002.

[62] S. Mallat. *A Wavelet Tour of Signal Processing*. Academic Press, San Diego, second edition, 1999.

[63] A. R. Margetts and P. Schniter. Joint scale-lag diversity in mobile wideband communication systems. *IEEE Trans. on Wireless Communications*. submitted.

[64] A. R. Margetts and P. Schniter. Joint scale-lag diversity in mobile wideband communication systems. *Proc. Asilomar Conf. on Signals, Systems and Computers*, Nov. 2004.

[65] A. R. Margetts and P. Schniter. On the correlation structure of wideband scale-lag rake fingers. *Proc. IEEE Workshop on Signal Processing Advances in Wireless Communication*, Jun. 2005.

[66] A. R. Margetts, P. Schniter, and A. Swami. Scale-lag diversity reception in mobile wideband channels. *Proc. IEEE Internat. Conf. on Acoustics, Speech, and Signal Processing*, Mar. 2005.

[67] S. Mo, A. Gelman, and J. Gopal. Frame synchronization in UWB using multiple sync words to eliminate line frequencies. *Proc. IEEE Wireless Communication and Networking Conf.*, 2:773–778, Mar. 2003.

[68] O. Moreno, C. C. Bravo, and S. Maric. New sequence design constructions for ultra-wideband systems. *Proc. IEEE Internat. Symposium on Information Theory*, pages 435–435, Jun. 2003.

[69] W. Namgoong. A channelized DSSS ultra-wideband receiver. *Radio and Wireless Conference*, pages 105–108, 2001.

[70] W. Namgoong. A channelized digital ultrawideband receiver. *IEEE Trans. on Wireless Communications*, 2(3):502–510, May 2003.

[71] C. Nassar, F. Zhu, and Z. Wu. Direct sequence spreading UWB systems: frequency domain processing for enhanced performance and throughput. *Proc. IEEE Intern. Conf. on Communication*, 3:2180–2186, May 2003.

[72] J. Ovarlez. Cramer-rao bound computation for velocity estimation in the broad band case using the mellin transform. *Proc. IEEE Internat. Conf. on Acoustics, Speech, and Signal Processing*, 1993.

[73] M. Pausini and G. Janssen. Analysis and comparison of autocorrelation receivers for IR-UWB signals based on differential detection. *Proc. IEEE Internat. Conf. on Acoustics, Speech, and Signal Processing*, 4:513–516, May 2004.

[74] J. Proakis. *Digital Communications*. McGraw-Hill, New York, NY, 3rd edition, 1995.

[75] J. Proakis. *Digital Communications*. McGraw-Hill, New York, NY, 4th edition, 2001.

[76] A. Rajeswaran, V. Somayazulu, and J. Foerster. Rake performance for a pulse based UWB system in a realistic UWB indoor channel. *Proc. IEEE Intern. Conf. on Communication*, 4:2879–2883, 2003.

[77] F. Ramirez-Mireles. On the performance of ultra-wide-band signals in gaussian noise and dense multipath. *IEEE Trans. on Vehicular Technology*, 50:244–249, Jan. 2001.

[78] F. Ramirez-Mireles. Performance of ultra wideband SSMA using time hopping and M-ary PPM. *IEEE Journal on Selected Areas In Communications*, 19:1186–1196, Jun. 2001.

[79] F. Ramirez-Mireles, M. Win, and R. Scholtz. Performance of ultra-wideband time-shift-modulated signals in the indoor wireless impulse radio channel. *Proc. Asilomar Conf. on Signals, Systems and Computers*, 1:192–196, 1997.

[80] R. Raulefs, A. Dammann, S. Kaiser, and G. Auer. The doppler spread - gaining diversity for future mobile radio systems. *Proc. IEEE Global Telecommunications Conf.*, 3:1301–1305, Dec. 2003.

[81] S. Rickard. *Time-frequency and time-scale representations of doubly spread channels*. PhD thesis, Princeton University, November 2003.

[82] B. M. Sadler and A. Swami. On the performance of episodic UWB and direct-sequence communication systems. *IEEE Trans. on Wireless Communications*, 3(6):2246–2255, Nov. 2004.

[83] A.-B. Salberg and A. Swami. Doppler and frequency-offset synchronization in wideband OFDM. *IEEE Trans. on Wireless Communications*. accepted for publication.

[84] A. Saleh and R. Valenzuela. A statistical model for indoor multipath propagation. *IEEE Journal on Selected Areas In Communications*, 5(2):128–137, Feb. 1987.

[85] A. M. Sayeed and B. Aazhang. Joint multipath-doppler diversity in mobile wireless communications. *IEEE Trans. on Communications*, 47(1):123–132, Jan. 1999.

[86] G. Schiavone, P. Wahid, R. Palaniappan, J. Tracy, E. van Doorn, and B. Lonske. Outdoor propagation analysis of ultra wide band signals. *Antennas and Propagation Society International Symposium*, 2:999–1002, Jun. 2003.

[87] R. Scholtz. Multiple access with time-hopping impulse modulation. *Military Communications Conference*, 2:447–450, 1993.

[88] R. Scholtz and J.-Y. Lee. Problems in modeling UWB channels. *Proc. Asilomar Conf. on Signals, Systems and Computers*, 1:706–711, Nov. 2002.

[89] M. K. Simon and M.-S. Alouini. A unified approach to the performance analysis of digital communication over generalized fading channels. *Proceedings of the IEEE*, 86(9):1860–1877, Sept. 1998.

[90] G. L. Stuber. *Principles of Mobile Communications*. Kluwer Academic, 1996.

[91] A. Swami, B. Sadler, and J. Turner. On the coexistence of ultra-wideband and narrowband radio systems. *Military Communications Conference*, 1:16–19, Oct. 2001.

[92] J. Taylor. Ultrawideband radar. *IEEE MTT-S International Microwave Symposium Digest*, 1:367–370, Jun. 1991.

[93] M. Terri, A. Hong, G. Guibe, and F. Legrand. Major characteristics of UWB indoor transmission for simulation. *Proc. IEEE Vehicular Technology Conference*, 1:19–23, Apr. 2003.

[94] Z. Tian, L. Yang, and G. Giannakis. Symbol timing estimation in ultra wideband communications. *Proc. Asilomar Conf. on Signals, Systems and Computers*, 2002.

[95] D. Tse and P. Viswanath. *Fundamentals of Wireless Communication*. Cambridge University Press, 2005.

[96] J. Walko. Agree to disagree [standardisation over UWB]. *IEE Review*, 50(5):28–29, May 2004.

[97] M. Weisenhorn and W. Hirt. Performance of binary antipodal signaling over the indoor UWB MIMO channel. *Proc. IEEE Intern. Conf. on Communication*, 4:2872–2878, 2003.

[98] L. G. Weiss. Wavelets and wideband correlation processing. *IEEE Signal Processing Magazine*, pages 13–32, Jan. 1994.

[99] R. Wilson and R. Scholtz. Comparison of CDMA and modulation schemes for UWB radio in a multipath environment. *Proc. IEEE Global Telecommunications Conf.*, 2:754–758, Dec. 2003.

[100] M. Win and R. Scholtz. Energy capture vs. correlator resources in ultra-wide bandwidth indoor wireless communications channels. *Military Communications Conference*, 3:1277–1281, Nov. 1997.

[101] M. Win and R. Scholtz. Ultra-wide bandwidth time-hopping spread-spectrum impulse radio for wireless multiple-access communications. *IEEE Trans. on Communications*, 48:679–689, Apr. 2000.

[102] D. Wu, P. Spasojevic, and I. Seskar. Ternary zero correlation zone sequences for multiple code UWB. *Proc. Conf. on Information Science and Systems*, Mar. 2004.

[103] B. Yang. Projection approximation subspace tracking. *IEEE Trans. on Signal Processing*, 43(1):95–107, Jan. 1995.

[104] L. Yang and G. Giannakis. Low-complexity training for rapid timing acquisition in ultra wideband communications. *Proc. IEEE Global Telecommunications Conf.*, 2:769–773, Dec. 2003.

[105] L. Yang and G. B. Giannakis. Ultra-wideband communications: An idea whose time has come. *IEEE Signal Processing Magazine*, pages 26–55, Nov. 2004.

[106] Y. Zakharov and V. Kodanev. Multipath-doppler diversity of ofdm signals in an underwater acoustic channel. *Proc. IEEE Internat. Conf. on Acoustics, Speech, and Signal Processing*, 5:2941–2944, Jun. 2000.

[107] H. Zhang and T. Gulliver. Performance and capacity of pam and ppm UWB systems with multiple receive antennas. *IEEE Pacific Rim Conference on Communications, Computers and signal Processing*, 2:740–743, Aug. 2003.

[108] H. Zhang, T. Udagawa, T. Arita, and M. Nakagawa. A statistical model for the small-scale multipath fading characteristics of ultra wideband indoor channel. *Conference on Ultra Wideband Systems and Technologies*, pages 81–85, May 2002.

[109] H. Zhang, S. Wei, D. Goeckel, and M. Win. Rapid acquisition of ultra-wideband radio signals. *Proc. Asilomar Conf. on Signals, Systems and Computers*, 2002.

[110] Z. Zhang and L. Ge. Differential detection acquisition for time-hopping sequence in ultra-wideband radio. *Proc. IEEE Internat. Symposium on Personal, Indoor and Mobile Radio Communications*, 2:2442–2445, Sep. 2003.

[111] L. Zhao and A. Haimovich. Performance of ultra-wideband communications in the presence of interference. *IEEE Journal on Selected Areas In Communications*, 20:1684–1691, Dec. 2002.